

Multiple scattering and time-reversal in granular media

Múltiple scattering e inversión temporal en medios granulares

Yamil Abraham Fernández

PhD Program in Physics
Facultad de Ciencias, Institut Langevin - Ondes et Images
Universidad de la República - Université Paris Sciences et Lettres

Uruguay – France
January 2023



UNIVERSIDAD DE LA REPUBLICA
URUGUAY

ESPCI PARIS | PSL



FACULTAD DE CIENCIAS



PEDECIBA

ANII
AGENCIA NACIONAL DE INVESTIGACIÓN E INNOVACIÓN



Institut Langevin
ONDES ET IMAGES

cnrs

Multiple scattering and time-reversal in granular media

Múltiple scattering e inversión temporal en medios granulares

Yamil Abraham Fernández

Thesis submitted to the PhD Program in Physics of Universidad de la República and Université Paris Sciences et Lettres, as part of the necessary requirements for obtaining the title of Doctor in Physics.

Directors:
Dr. Carlos A. Negreira
Dr. Arnaud Tourin

Co-dvisors:
Dr. Nicolás Benech
Dr. Xiaoping Jia

Uruguay – France
January 2023

Abraham Fernández, Yamil

Multiple scattering and time-reversal in granular media / Yamil Abraham Fernández. - Uruguay: Universidad de la República, Université Paris Sciences et Lettres, Facultad de Ciencias, Institut Langevin - Ondes et Images, 2023.

xi, 124 p. 29, 7cm.

Directors:

Carlos A. Negreira

Arnaud Tourin

Co-dvisors:

Nicolás Benech

Xiaoping Jia

Thesis de Doctoral Degree – Universidad de la República, Program in Physics, 2023.

References: p. 117 – 117.

1. Ultrasound acoustics, 2. Multiple scattering, 3. Time reversal focusing, 4. Transport parameters, 5. Granular media. I. Negreira, Carlos A., Tourin, Arnaud, *et al.* II. Universidad de la República, PhD Program in Physics.III. Título.

MEMBERS OF THE THESIS DEFENSE JURY

Arturo MARTÍ
President

Nicolás PÉREZ
Reporter

Thomas BRUNET
Reporter

Agnès MAUREL
Examiner

Carlos NEGREIRA
Thesis Director

Uruguay – France
January 2023

Acknowledgements

First of all, I would like to thank my supervisors Arnaud, Xiaoping, Carlos and Nicolas for their patience and for all the work we did together during these years of my PhD. The experience of participating with them in an international cotutelage was very pleasant and fruitful. I hope to collaborate again and share future works with them.

I would like to thank the administrative staff who helped me during my PhD, both from the Institut Langevin (in particular Catherine Dupuy) and PSL University, as well as from PEDECIBA (in particular Jimena Rodríguez) and Facultad de Ciencias. I would also like to thank PEDECIBA, ANII, CAP, ESPCI, Campus France and LIA for their financial support throughout my PhD.

I would also like to thank my colleagues and friends from the Institute of Physics, who made the course during the writing of the manuscript more enjoyable with their daily company. The people from the Institut Langevin for welcoming me and making me part of it. Thanks to the group of PhD students, in particular Camilo, Loubnan, Guyu, Anwesh and Max, with whom we shared many good moments during my many stays in Paris. Thanks also to Daphneé and Ross, who were a great support and could be considered my godparents in France.

Many thanks to those friends who were present during my thesis. A special mention to the MVPs: Gonzalo, with whom I have the pleasure to share office, work and even bar, I would like to thank him for his daily company and constant support, being next to me or in a different country; and Miguel, who after offering me to reside with him in Paris became one of my closest friends, and whose company during my stays in France made the experience infinitely more pleasant.

Last but not least, thanks to Paula and to my family.

To my sister and brother.
To my mother and father.
To my grandma and grandpa.

ABSTRACT

In this thesis, we investigate new applications of time-reversal of acoustic waves in the multiple scattering regime, not only as a focusing method but also as a means for measuring the transport parameters of a multiple scattering medium. We first study experimentally the scattering of waves in a system composed of copper rods immersed in water as a 2D model, from the dilute state to the dense packing. We show the appearance of a low-frequency ballistic wave when rods are put in contact. These results are analyzed as a function of the scatterer's density on the basis of the multiple scattering theory developed for dilute media.

Then we consider a more complicated family of systems, namely 3D dense granular media immersed in water. In these media, we present a configuration that exhibits the sensitivity of time-reversal focusing to the transport parameters of the medium. It has already been shown that a link can be established between time reversal and the coherent backscattering effect. This latter phenomenon, which results from the combined effects of the reciprocity of a medium and its diffusive behavior, can be exploited to measure the transport parameters of wave propagation in the medium: the mean free path and the diffusion coefficient. Here, we show for the first time that time-reversal focusing can also be used to measure the diffusion coefficient. We present experimental results and compare them with a new theoretical model, where time-reversal focusing becomes a method to measure the diffusion coefficient.

In a second part, we focus on a 3D dry granular medium under stress. As shown in previous works, acoustic waves provide a non-intrusive probe of the heterogeneous contact network between grains. These waves can propagate as coherent ballistic waves or as multiple scattered waves through the network as a function of the ratio of wavelength to grain size. In dry granular media, acoustic waves can be used not only as a probe but also as a "pump" to induce rearrangements in the medium. Here, we seek to remotely create a controlled perturbation by time-reversal of the multiple scattered waves. We then monitor the rearrangements of the dry granular medium induced this way by a cross-correlation technique.

Keywords:
Ultrasound acoustics, Multiple scattering, Time reversal focusing, Transport parameters, Granular media.

RESUMEN

En esta tesis investigamos nuevas aplicaciones de la inversión temporal de ondas acústicas en régimen de múltiple scattering, no sólo como método de focalización sino también como método para medir los parámetros de transporte de un medio multidifusor. En primer lugar, estudiamos experimentalmente el scattering de ondas en un medio compuesto por cilindros de cobre sumergidos en agua como modelo 2D, desde el sistema diluido hasta el empaquetamiento denso. Se muestra la aparición de una onda balística de baja frecuencia cuando los cilindros se ponen en contacto. Estos resultados se analizan en función de la densidad de difusores, basándonos en la teoría de múltiple scattering desarrollada para medios diluidos.

A continuación, consideramos una familia de sistemas más compleja, a saber, los medios granulares densos 3D, inmersos en agua. En estos medios, presentamos una configuración que exhibe la sensibilidad de la focalización por inversión temporal a los parámetros de transporte del sistema. Ya se ha demostrado que se puede establecer un vínculo entre la inversión temporal y el cono de retrodifusión coherente. Este último fenómeno, que resulta de los efectos combinados de la reciprocidad de un medio y su carácter difusivo, puede ser explotado para medir los parámetros de transporte de la propagación de ondas en el medio: el recorrido libre medio y el coeficiente de difusión. Aquí mostramos por primera vez que la focalización por inversión temporal también puede utilizarse para medir el coeficiente de difusión. Presentamos resultados experimentales y los comparamos con un nuevo modelo teórico, en el que la focalización por inversión temporal se convierte en un método para medir el coeficiente de difusión.

En una segunda parte, nos centramos en un medio granular seco 3D, sometido a presión externa. Como se ha mostrado en trabajos anteriores, las ondas acústicas proporcionan una sonda no invasiva de la red de contactos heterogéneos que existe entre granos. Estas ondas pueden propagarse como ondas balísticas coherentes o como ondas de coda a través de la red, en función de la relación entre la longitud de onda y el tamaño de los granos. En los medios granulares secos, las ondas acústicas pueden utilizarse no sólo como sonda sino también como "bomba" para inducir reordenamientos en el medio. En este caso, intentamos crear una perturbación controlada a distancia mediante la inversión temporal de las ondas difundidas por el medio. Finalmente, monitoreamos los reordenamientos del medio granular inducidos de esta manera mediante una técnica de correlación cruzada de firmas acústicas.

Palabras Claves:

Acústica ultrasonora, Scattering múltiple, Focalización por inversión temporal, Parámetros de transporte, Medios granulares.

Table of Contents

1 Acoustic wave propagation in 2D scattering media: from the dilute to the compact case **5**

1.1 Fundamentals . . . 6

1.1.1 Dilute complex media and Independent scattering approximation . 6

1.1.2 Diffusion . . . 10

1.2 Wave transmission in dilute multiple scattering media . . . 12

1.2.1 Experimental set-up . . . 12

1.2.2 Measurement of scattering mean free path . . . 13

1.3 Acoustic transmission in 2D multiple scattering compact media . . . 19

1.3.1 Experimental set-up . . . 19

1.3.2 Experimental results . . . 20

1.4 Discussion and conclusions . . . 25

References . . . 27

2 Time-reversal focusing in immersed granular media for wave transport study **29**

2.1 Intensity wave transport in immersed granular media . . . 30

2.1.1 Diffusive transport . . . 30

2.1.2 Coherent backscattering cone . . . 39

2.2 Time-reversal as a means to measure transport parameters . . . 50

2.2.1 Fundamentals of time-reversal . . . 50

2.2.2 Link between time-reversal and transport parameters . . . 54

2.2.3 Physical model . . . 55

2.2.4 Stationary time-reversal . . . 63

2.2.5 Dynamic time-reversal . . . 68

2.3 Discussion and conclusions . . . 72

References . . . 74

3 Time-reversal in dry granular media for triggering rearrangements **77**

3.1 Fundamentals of dry granular media . . . 78

3.1.1 A dry assembly of grains as an effective elastic medium . . . 78

3.1.2 A dry assembly of grains as a disordered medium . . . 79
3.1.3 The importance of the contact force network . . . 80
3.1.4 Jamming and unjamming . . . 81
3.1.5 Elastic wave propagation and scattering . . . 84
3.2 Proof-of-principle experiment: time-reversal in a chaotic cavity . . . 86
3.2.1 Time-reversal in a 2D chaotic cavity . . . 87
3.2.2 Time-reversal experiment in a 3D chaotic cavity . . . 88
3.2.3 Bead dropping by time-reversal focusing . . . 90
3.3 Time-reversal experiment through a dry granular medium . . . 92
3.3.1 Experimental setup . . . 93
3.3.2 Sample preparation protocol . . . 93
3.3.3 Single-channel time-reversal experiment . . . 98
3.4 Time-reversal as a means for triggering rearrangement . . . 104
3.4.1 Single-channel time reversal . . . 104
3.5 Discussion and conclusions . . . 106
References . . . 109

4 Conclusions and perspectives **112**

Appendices **117**

Appendix A Time-reversal experiments in dry granular media using multi-channel time-reversal mirror . . . 118
A.0.1 Multi-channel time-reversal mirror . . . 119
A.0.2 Multi-channel high-amplitude time reversal . . . 123

Introduction

Wave propagation in random media has been a subject of interest for a long time in various areas of physics, from quantum waves in condensed matter to classical waves in optics or acoustics. In this thesis, our research is focused on acoustic wave propagation in a special class of scattering media, namely random packings of rods or beads, either dry or immersed in water.

An acoustic wave propagating in a non-homogeneous medium may undergo effects such as reflection, refraction or diffraction. These are commonly known as "scattering" events, and a medium where the wave is, on average, scattered more than once before leaving it out, is referred to as a multiple scattering medium. A wave traveling in this type of medium presents alterations in its amplitude, phase and propagation velocity, giving rise to an output wave that (a priori) has no relation with the input wave.

Such a medium is a nightmare for imaging. However, a multiple scattered wave can still give information about the medium through which it propagates, at least in an average sense.

After several scattering events, the wave begins to lose its coherence. In this context, the coherent part of the wave must be understood as the part that survives averaging over different configurations of disorder. For a medium having randomly distributed scatterers, it is then possible to define the characteristic length of coherent energy decay. This distance is known as the scattering or elastic mean free path. When the medium size exceeds a few times the mean free path, we can assume that the coherence is completely lost. Similarly, it is possible to define the characteristic time of energy absorption, referred to as the absorption time. This quantity is associated with the decay in energy produced by the time the wave propagates within the medium[1].

When the amount of scattering events becomes high enough such that the coherent wave has vanished, it is necessary to study the second momentum of the wavefield, namely the average intensity. It has already been known for a long time that the intensity averaged over the different configurations of disorder obeys a diffusion equation for sample sizes much larger than the scattering mean free path[2]. This suggests that the wave energy

[1]Sheng, P. (2006). Introduction to wave scattering, localization and mesoscopic phenomena (Vol. 88). Springer Science & Business Media.

[2]Tourin, A., Fink, M., & Derode, A. (2000). Multiple scattering of sound. Waves in random media, 10(4), R31.

propagates as a random walk controlled by a diffusion coefficient. The diffusion coefficient is the product of a velocity (the so-called energy velocity, that is neither the phase velocity nor the group velocity) and a characteristic length named the transport mean free path. This distance, which can be related to the scattering mean free path, can be interpreted as the length after which the wave has "lost its memory" of where it came from (in the sense of a random walk). When a medium exhibits this kind of behavior, we call it "diffusive", and the set of parameters that characterize it are called the transport parameters.

Unlike a pure random walk, wave propagation in a diffusive medium can, however, maintain some coherence. In other words, interference effects can survive disorder, which manifests itself in the Coherent Backscattering Effect (CBE) as shown by Tourin et al. with acoustic waves[3]. Interestingly, the CBE provides an efficient practical way of measuring independently the diffusion coefficient and the transport mean free path.

The fact that coherence survives disorder has also been very nicely illustrated in time-reversal experiments carried out in the early 1990s by Mathias Fink's group. A time-reversal mirror is a device that is able to capture a wavefield, to flip it in time and to backpropagate it in order to make it converge onto the source where it was emitted[4]. These pioneering experiments contributed to creating a new paradigm for wave manipulation. Contrary to long held beliefs, disorder is not always an impediment to focusing but can be turned into an ally[5], which opened new avenues for applications, especially in the field of wireless communications[6].

Interestingly, the coherent backscattering effect and time-reversal are closely related as was shown in two papers, by de Rosny et al. and by van Tiggelen in the early 2000's[7][8].

In this thesis, we have pushed the analogy to its end by demonstrating, both theoretically and experimentally, how the diffusion coefficient can be measured in a time-reversal experiment where the Time-Reversal Mirror is embedded in the scattering medium, here consisting of a collection of beads immersed in water.

So far, we have presented the perspective from the point of view of acoustic wave propagation, regardless of the precise characteristics of the propagation medium. However, in this thesis, we have also focused on a special type of media, namely granular media.

[3]Tourin, A., Derode, A., Roux, P., Van Tiggelen, B. A., & Fink, M. (1997). Time-dependent coherent backscattering of acoustic waves. Physical review letters, 79(19), 3637.

[4]Fink, M. (1992). Time reversal of ultrasonic fields. I. Basic principles. IEEE transactions on ultrasonics, ferroelectrics, and frequency control, 39(5), 555-566.

[5]Derode, A., Roux, P., & Fink, M. (1995). Robust acoustic time reversal with high-order multiple scattering. Physical review letters, 75(23), 4206.

[6]Montaldo, G., Lerosey, G., Derode, A., Tourin, A., de Rosny, J., & Fink, M. (2004). Telecommunication in a disordered environment with iterative time reversal. Waves in Random Media, 14(3), 287.

[7]De Rosny, J., Tourin, A., Derode, A., Van Tiggelen, B., & Fink, M. (2004). Relation between time reversal focusing and coherent backscattering in multiple scattering media: A diagrammatic approach. Physical Review E, 70(4), 046601.

[8]Van Tiggelen, B. A. (2003). Green function retrieval and time reversal in a disordered world. Physical review letters, 91(24), 243904.

A granular medium is a medium composed of many macroscopic solid particles[9]. This definition encompasses a large number of media, as well as many difficulties in working with them, since these particles can be of different materials, sizes and shapes. Despite this, granular media appear as a matter of course in our daily lives and in the industry. P.G. de Gennes mentioned that, after water, the second most manipulated material by mankind is precisely this kind of media[10].

Granular materials have the particularity that they can be found in solid, liquid or gaseous states. Typically, the size of the grains can be from microns to meters, which allows to neglect the Brownian motion of the grains. This implies that a statistical approach cannot be driven, since there is no "temperature" for the system to explore different states.

Granular materials are usually optically opaque. Thus, acoustic wave propagation offers a unique way of probing the set of interconnected force chains that appears in a 3D granular medium under stress[11], referred to as the force network.

Granular media have a peculiar position amongst random media. Most of the models developed for wave propagation in complex media rely on a basic continuous medium (the background), in which are randomly placed discrete scatterers that diffract waves propagating in the background. In a dilute medium approximation, the average effect of the scatterers can be represented by replacing the acoustic constants of the background by some new effective ones. The situation is much more complex in the case of granular media, since the scatterers are put in contact such that there is no more separation between a reference medium and the grains. Instead, we are left with two media: one in the porous space, the other one in the granular space. For large acoustic wavelengths, this situation was modelized a long time ago by Biot who predicted the existence of a slow compressional wave[12]. It must be pointed out that even with a porous space filled with air (dry granular medium), an acoustic wave can propagate through the contacts from one grain to another, which suggest a discretization of the problem.

In our work, we have addressed this issue experimentally, by first studying the transition from a 2D dilute medium to a 2D compact medium; and then by implementing acoustic methods to infer the transport parameters of both dry and immersed granular media.

Interestingly, acoustic waves can be also used as a pump, which may alter the force chains through which it propagates. Such a modification, which is not necessarily macroscopic but rather at the contact forces level, is called "rearrangement". A study from M.

[9] By macroscopic we mean larger than 1μm; for such a size one can neglect Brownian motion.

[10] de Gennes, P. G. (1999). Granular matter: a tentative view. Reviews of modern physics, 71(2), S374.

[11] Jia, X., Caroli, C., & Velicky, B. (1999). Ultrasound propagation in externally stressed granular media. Physical Review Letters, 82(9), 1863.

[12] Biot, M. A. (1956). Theory of propagation of elastic waves in a fluid-saturated porous solid. I. Low frequency range. The Journal of the acoustical Society of america, 28(2), 168-178.

Harazi et al. showed that time-reversal invariance is lost when the source emits a wave that has an amplitude high enough, indicating that the medium is being rearranged[13].

In this direction, what if the high amplitude is introduced in the phase two of a time-reversal experiment? Would it be possible to trigger rearrangements remotely if the amplitude focused back at the source is large enough? This is the last issue we addressed in this thesis.

This doctoral dissertation is organized as follows.

In the first chapter, the basic concepts of multiple wave scattering are presented. Using a simple 2D multiple scattering medium model composed of copper cylinders immersed in water, an experimental analysis is performed, where the results are confronted to the theoretical predictions. Then, the transition between a dilute and a compact medium is investigated, paying special attention to the validity range of the dilute medium approximation.

The second chapter is devoted to the study of a 3D granular medium immersed in water together with the determination of its transport parameters. In the first instance, we measure the diffusion coefficient by analyzing the average intensity profile of the wave transmitted through the medium. Then, the backscattered average intensity is analyzed and the Coherent Backscattering Effect is used to measure both the diffusion coefficient and the transport mean free path. Finally, an original experimental setup is implemented in the system where, according to theoretical predictions, time-reversal focusing exhibits its dependence on the diffusion coefficient.

In the third chapter, we proceed to study a dry 3D granular medium under an applied external pressure. In order to remotely generate rearrangements at a given place, we exploit the time-reversal focusing of acoustic waves. As a first proof of concept, we use time-reversal focusing in a reverberant cavity with a chaotic shape to trigger an "avalanche" of a single grain. Then, we move on to a dry granular medium. We first put our efforts in defining a controlled preparation protocol in order to ensure the reproducibility of the experiments. Then, we verify the stability of the granular medium when performing time-reversal experiments at low amplitudes. Finally, we study the behavior of the system when we increase the amplitude of the re-emission in phase two of the time-reversal process and manage to prove the possibility to create a controlled rearrangement around the initial source.

The final chapter summarizes the main results and presents some perspectives.

[13]Harazi, M., Yang, Y., Fink, M., Tourin, A., & Jia, X. (2017). Time reversal of ultrasound in granular media. The European Physical Journal Special Topics, 226(7), 1487-1497.

Chapter 1

Acoustic wave propagation in 2D scattering media: from the dilute to the compact case

Contents

1.1 Fundamentals 6

1.1.1 Dilute complex media and Independent scattering approximation 6

1.1.2 Diffusion 10

1.2 Wave transmission in dilute multiple scattering media 12

1.2.1 Experimental set-up 12

1.2.2 Measurement of scattering mean free path 13

1.3 Acoustic transmission in 2D multiple scattering compact media 19

1.3.1 Experimental set-up 19

1.3.2 Experimental results 20

1.4 Discussion and conclusions 25

References 27

Multiple scattering of waves is a long-standing subject that provides a basis for many phenomena observed both in everyday life and in various areas of physics. In seismology, the study of seismic waves (or coda waves) led to the understanding that the generation of long-lasting seismic signals is due solely to multiple scattering effects between the wave and inhomogeneities present in both the lower lithosphere and the earth's crust [1, 2]. In underwater acoustics, the study of backscattered waves produced by the ocean floor makes it possible to estimate their composition by acoustic mapping [3]. In optics, the study of random scattering of electromagnetic waves has made it possible to improve

telecommunications systems to date [4]. In quantum waves, the study of electron wave functions and their interaction with a disordered (or impure) crystalline lattice justifies the conductive properties of metals, as well as the case known as Anderson localization [5], giving rise to mesoscopic physics.

Throughout this chapter the basic concepts of multiple scattering media are presented. Initially, this kind of media is shown in its most general form, introducing the physical terms involved in working with them. Concepts such as the transport mean free path and the diffusion coefficient are duly presented, both theoretically and experimentally. Applied cases in the laboratory are shown, where the physical models presented are compared with experimental results in our complex media. In particular, this chapter focuses on two-dimensional multiple scattering systems.

1.1 Fundamentals

We speak of multiple scattering when a wave does not propagate freely in a medium, but is subjected to several scattering events. This kind of propagation media is commonly referred to as a "multiple scattering medium" or "complex medium". Multiple scattering can be originated by local changes in the density or compressibility in a fluid-fluid model, i.e. local changes in the specific acoustic impedance. Throughout this chapter we will consider scattering to be fully elastic, which means that each event alters the direction of wave propagation but not its frequency [6].

Green's formalism is commonly used to deal mathematically with multiple scattering phenomena. With it, it is possible to describe a wave propagating through a complex medium and, with the corresponding assumptions, to infer the characteristic parameters inherent to the system (also known as transport parameters).

1.1.1 Dilute complex media and Independent scattering approximation

Let us assume a homogeneous medium with propagation velocity c, whose dispersion relation is given by $k_0^2(\omega) = \omega^2/c^2$. If a short pulse is emitted at time $t = 0$ and at position $\mathbf{r} = \mathbf{r}'$, then, in the frequency domain, the corresponding wavefield satisfies

$$\left(\nabla^2 + k_0^2\right) G_0\left(\omega, \mathbf{r} - \mathbf{r}'\right) = \delta\left(\mathbf{r} - \mathbf{r}'\right). \tag{1.1}$$

Here the Green's function G_0 depends on both the frequency and the distance between the source and receiver, since it is a homogeneous medium. One method to solve this equation is to work in the spatial frequency domain, the $\mathbf{k}$-space,

$$G_0(\omega, \mathbf{r}-\mathbf{r}') = \int G_0(\omega, \mathbf{k})\, e^{-i\mathbf{k}(\mathbf{r}-\mathbf{r}')} d\mathbf{k},$$

which by sustitution in (1.1) leads to

$$G_0(\omega, \mathbf{k}) = \frac{1}{k_0^2(\omega) - k^2}. \tag{1.2}$$

The wave propagation is then expressed by equation (1.2), whose analytical form in real space depends on the spatial dimension.

When the wave travels through a medium that exhibits inhomogeneities, the wave propagation velocity becomes a function of the spatial variable $c = c(\mathbf{r})$. For media that do not change their properties in time, i.e. stationary media, the spatial dependence of the velocity can be translated into a spatial dependence of the wave number, which can be written as [6]

$$k^2(\mathbf{r}) = k_0^2 - \sigma(\mathbf{r}), \tag{1.3}$$

where $\sigma(\mathbf{r})$ is the perturbation from the homogenuous medium.

Substituting in the equation (1.1) we obtain that

$$\left(\nabla^2 + k_0^2\right) G(\omega, \mathbf{r}, \mathbf{r}') = \delta(\mathbf{r}-\mathbf{r}') + \sigma(\mathbf{r})\, G(\omega, \mathbf{r}, \mathbf{r}'). \tag{1.4}$$

The second term on the right-hand side in (1.4) appears as an additional source-term, which manifests the presence of inhomogeneities and can be interpreted as responsible for the scattering events.

For convenience, we define the two-entry operator $V(\mathbf{r_1}, \mathbf{r_2})$ as

$$V(\mathbf{r_1}, \mathbf{r_2}) = \sigma(\mathbf{r_1})\, \delta(\mathbf{r_1} - \mathbf{r_2}), \tag{1.5}$$

also known as *impurity potential operator*. With this definition, operator V contains all the information about the multiple scattered waves.

The Green's function satisfying equation (1.4) is a solution whose analytic form is given by

$$G(\omega, \mathbf{r}, \mathbf{r}') = G_0(\omega, \mathbf{r}-\mathbf{r}') + \iint G_0(\omega, \mathbf{r}-\mathbf{r_1})\, V(\mathbf{r_1}, \mathbf{r_2})\, G(\omega, \mathbf{r_2}, \mathbf{r}')\, d\mathbf{r_1} d\mathbf{r_2} \tag{1.6}$$

Such a solution can be written, by iterative substitution and rearrangement of the terms, as

$$G(\omega,\mathbf{r},\mathbf{r}') = G_0(\omega,\mathbf{r}-\mathbf{r}') + \iint G_0(\omega,\mathbf{r}-\mathbf{r_1})\,V(\mathbf{r_1},\mathbf{r_2})\,G_0(\omega,\mathbf{r_2}-\mathbf{r}')\,d\mathbf{r_1}d\mathbf{r_2} + \iiiint G_0(\omega,\mathbf{r}-\mathbf{r_1})\,V(\mathbf{r_1},\mathbf{r_2})\,G_0(\omega,\mathbf{r_2}-\mathbf{r_3}) \times V(\mathbf{r_3},\mathbf{r_4})\,G_0(\omega,\mathbf{r_4}-\mathbf{r}')\,d\mathbf{r_1}d\mathbf{r_2}d\mathbf{r_3}d\mathbf{r_4} + \cdots. \quad (1.7)$$

This solution can be interpreted as follows. The Green's function in a medium presenting a region where multiple scattering occurs, corresponds to the solution in the homogeneous medium plus a perturbation introduced by the inhomogeneities present in it. Thus, the solution is made up of the wave in the homogeneous medium plus a contribution that contains the scattering information present throughout its propagation. The way of writing equation (1.7) allows to interpret each term as the total contribution of those trajectories with the same amount of scattering events occurred. The first term, as mentioned, corresponds to the wave propagating through the homogeneous medium, i.e. without scattering events. The second term involves an integral that contains the information about the distribution of the scatterers; this term is the sum of all the paths between the emitter and the receiver that have a single scattering event. This term corresponds to the simple scattering, first order Born approximation [7]. Similarly, the third term considers the contribution of those trajectories with two scattering events. And so on.

Let us consider the average among many different configurations of disorder. Performing this operation on equation (1.6), we can write

$$\langle G(\omega,\mathbf{r}-\mathbf{r}')\rangle = G_0(\omega,\mathbf{r}-\mathbf{r}') + \iint G_0(\omega,\mathbf{r}-\mathbf{r_1})\,\Sigma(\omega,\mathbf{r_1}-\mathbf{r_2})\,\langle G(\omega,\mathbf{r_2}-\mathbf{r}')\rangle d\mathbf{r_1}d\mathbf{r_2}, \quad (1.8)$$

where the dependence on $\mathbf{r}-\mathbf{r}'$ has been written explicitly for the average Green's function.

The quantity $\Sigma(\omega,\mathbf{r_1}-\mathbf{r_2})$, which appears in (1.8), is known to as the "self-energy" operator. While the V operator describes the local perturbations for a particular configuration given by $\sigma(\mathbf{r})$, Σ is a nonlocal operator that represents the multiple scattering contribution that survives the disorder.

Throughout this chapter, we will consider the Independent Scattering Approximation (ISA). If we write the self-energy as a Taylor expansion of the density of scatterers, the ISA consist on doing a first-order approximation of it. Consequently, the mulitple scattering medium is considered a dilute medium [6–8]. This picture is substantially different from the simple scattering Born approximation, since the self-energy takes into account the

contribution of multiple scattering effects in the medium.

Scattering mean free path

Analogous to how we proceeded above, the solution of the equation (1.8) can be written in the same analytical form as (1.2) in the **k**-space, with an extra term corresponding to the self-energy operator

$$\langle G(\omega, \mathbf{k})\rangle = \frac{1}{k_0^2(\omega) - \Sigma(\omega, \mathbf{k}) - k^2}, \tag{1.9}$$

where this formula is known to as Dyson equation [6].

Under the ISA, the self-energy can be written as the density of scatterers multiplied by the scattering operator of a single scatterer. Furthermore, if we assume that the scatterers are isotropic and that their size is smaller than the wavelength, the self-energy can be considered independent of **k** over a certain frequency range [7, 8]. Thus, we can lump the wavenumber of the homogeneous medium and the self-energy into an effective wavenumber

$$k_e^2(\omega) = k_0^2(\omega) - \Sigma(\omega). \tag{1.10}$$

With the definition of the effective wave-number given by (1.10), the Dyson equation (1.9) reduces to the equation (1.2), exchanging k_0^2 to k_e^2. This means that the wave propagates as in a homogeneous medium with renormalized velocity. This solution in the renormalized medium plays the role of G_0 and we refer to it as the *effective* Green's function

$$G_e(\omega, \mathbf{k}) = \frac{1}{k_e^2(\omega) - k^2}. \tag{1.11}$$

In general, the effective wavenumber is a complex number. With this in mind, the imaginary part of k_e is responsible for an exponential decay in the effective Green's function. Because G_e is the one that survives after averaging over the different disorder configurations of the medium, such a function carries with it the *coherence* of what was emitted during the initial excitation. Therefore, such an exponential decay defines a characteristic decay-length of the coherent energy, known as the *scattering* or *elastic mean free path*. Mathematically, this quantity is given by the relation $\ell_S = 1/2\mathrm{Im}(k_e)$. Thus, the coherent energy transmission coefficient for a distance L is given by

$$T_c = \exp\left(-\frac{L}{\ell_S}\right). \tag{1.12}$$

Under the assumptions considered, the imaginary part of k_e can be written as the

density of scatterers (n) times the total scattering cross-section of a single scatterer σ_T[1]. [6, 8]. Thus, we can conclude that the scattering mean free path can be written as

$$\ell_S = \frac{1}{n\sigma_T}. \tag{1.13}$$

The total scattering cross-section for a single scatterer is defined as the differential scattering cross-section integrated over the solid angle

$$\sigma_T = \int \frac{d\sigma}{d\Omega} d\Omega.$$

The quantity $d\sigma/d\Omega$ is the scattered energy in the direction (θ, ϕ) in the solid angle $d\Omega$, for an incident plane wave [6].

1.1.2 Diffusion

When the thickness L of the multiple scattering medium becomes much larger than the scattering mean free path ℓ_S, the coherence is completely extinguished. In such a circumstance, the mean transmitted amplitude tends to zero $\langle G \rangle \to 0$. To study the propagation of a wave in such a case, it is essential to analyze the second momentum of the Green's function, which corresponds to the average intensity $\langle I \rangle = \langle GG^* \rangle$.

We start from the expression (1.6) for G and for its conjugate function G^* in the renormalized medium:

$$G\left(\omega, \mathbf{r_A}, \mathbf{r_B}\right) = G_e\left(\omega, \mathbf{r_A} - \mathbf{r_B}\right) + \iint G_e\left(\omega, \mathbf{r_A} - \mathbf{r_1}\right) V_e\left(\mathbf{r_1}, \mathbf{r_2}\right) G\left(\omega, \mathbf{r_2}, \mathbf{r_B}\right) d\mathbf{r_1} d\mathbf{r_2} \tag{1.14}$$

$$G^*\left(\omega, \mathbf{r'_A}, \mathbf{r'_B}\right) = G_e^*\left(\omega, \mathbf{r'_A} - \mathbf{r'_B}\right) + \iint G_e^*\left(\omega, \mathbf{r'_A} - \mathbf{r_1}\right) V_e^*\left(\mathbf{r_1}, \mathbf{r_2}\right) G^*\left(\omega, \mathbf{r_2}, \mathbf{r'_B}\right) d\mathbf{r_1} d\mathbf{r_2}. \tag{1.15}$$

V_e is the potential operator in the renormalized medium, which average over different disorder configurations $\langle V_e \rangle$ is zero.

From the expressions for G and G^*, we can find the intensity as the product between them. Likewise, considering the average of the intensity over different disorder configurations, we obtain the formula known as the Bethe-Salpeter equation [6]

[1] This relationship is known as the *optical theorem* and relates the total scattering cross-section to the imaginary part of the forward scattering amplitude.

$$\langle G\left(\omega,\mathbf{r_A},\mathbf{r_B}\right)G^{*}\left(\omega,\mathbf{r'_A},\mathbf{r'_B}\right)\rangle = G_e\left(\omega,\mathbf{r_A}-\mathbf{r_B}\right)G_e^{*}\left(\omega,\mathbf{r'_A}-\mathbf{r'_B}\right) + \iiiint G_e\left(\omega,\mathbf{r_A}-\mathbf{r_1}\right)G_e^{*}\left(\omega,\mathbf{r'_A}-\mathbf{r_2}\right)\Gamma\left(\mathbf{r_1},\mathbf{r_2},\mathbf{r_3},\mathbf{r_4}\right) \times \langle G\left(\omega,\mathbf{r_3},\mathbf{r_B}\right)G^{*}\left(\omega,\mathbf{r_4},\mathbf{r'_B}\right)\rangle d\mathbf{r_1}d\mathbf{r_2}d\mathbf{r_3}d\mathbf{r_4}. \quad (1.16)$$

This equation is mathematically analogous to the Dyson equation (1.8), where the four-entry operator $\Gamma\left(\mathbf{r_1},\mathbf{r_2},\mathbf{r_3},\mathbf{r_4}\right)$ plays the role of the self-energy. This operator Γ is called the vertex function.

In the diffusive process approximation, we treat the intensity propagation as a random walk. In this context, we have that the time-domain average intensity satisfies a diffusion equation of the form [6, 8]

$$D\nabla^2\langle I\left(t;\mathbf{r},\mathbf{r'}\right)\rangle - \frac{\partial\langle I\left(t;\mathbf{r},\mathbf{r'}\right)\rangle}{\partial t} = \delta\left(\mathbf{r}-\mathbf{r'}\right)\delta\left(t\right), \quad (1.17)$$

where D is the diffusion coefficient. D is related to another parameter called *transport mean free path* ℓ^* through the transport velocity v_T by the relation

$$D = \frac{1}{d}v_T\ell^*, \quad (1.18)$$

where the variable d is the spatial dimension of the physical model.

Transport parameters have different meanings in the characterization of diffusive multiple scattering media. On the one hand, the transport velocity measures the energy flow along the diffusive regime. On the other hand, the diffusion coefficient is a dynamic parameter representing the area covered per unit time by the diffusive halo. This parameter is related to the transport mean free path, which is the characteristic distance that the intensity travels before "losing its memory". This quantity is the characteristic distance after which the wave does not remember where it originated, i.e., it has completely lost coherence. The transport and the scattering mean free paths are quite different. However, these two characteristic distances can be linked by the relation [6, 7]

$$\ell^* = \frac{\ell_S}{1-\overline{\cos\phi}}, \quad (1.19)$$

where the function $\overline{\cos\phi}$ is the average cosine of the scattering angle by one scatterer.

1.2 Wave transmission in dilute multiple scattering media

1.2.1 Experimental set-up

Let us consider a 2D dilute medium composed of parallel copper cylinders, with diameter $d = 0.70$mm. The rods are arranged in a regular grid consisting of a square lattice, with lattice constant $b = (2.55 \pm 0.02)\,\mathrm{mm}$. The randomization of the system is realized by filling each grid space with a probability of 75%. With this preparation, the medium has a number density of scatterers $n = (0.115 \pm 0.002)\,\mathrm{mm}^{-2}$ and surface factor $\eta = (4.44 \pm 0.07)\,\%$. These values allow us to consider the system sufficiently random to fit the dilute media theory hypothesis [9]. A side image of the system is presented in Figure 1.1.



Figure 1.1: Image of the dilute multiple scattering system used during the experiments. Copper cylinders of diameter 0.7 mm are randomly arranged in a regular grid. The height of the scatterers is sufficiently larger than the diameter, so the system can be considered 2D.

Two identical *harisonic* I3-0108-S circular transducers with diameter 12.7mm and central frequency of 1.0MHz, are used to transmit and receive acoustic signals. The size and frequency are chosen for convenience, as they favor coherent transmission through the system. In the next section 1.3 this choice will be argued in more detail.

The transmission and reception is controlled computationally through a system *Lecoeur Electronics* connected to a PC. This electronic platform is capable of handling simultaneously and independently up to thirtytwo channels in emission and another thirtytwo channels in reception. This equipment allows to record signals with a sampling frequency up to 80MHz.

The emitter and receiver are placed 210mm apart and submerged in a tank filled with degassed water. Between the transducers is placed the multiple scattering system, which is 175mm wide and whose depths L range from $L = 24$mm to $L = 75$mm. Pictures of the

experimental setup, as well as a schematic representation of it, are presented in Figure 1.2.

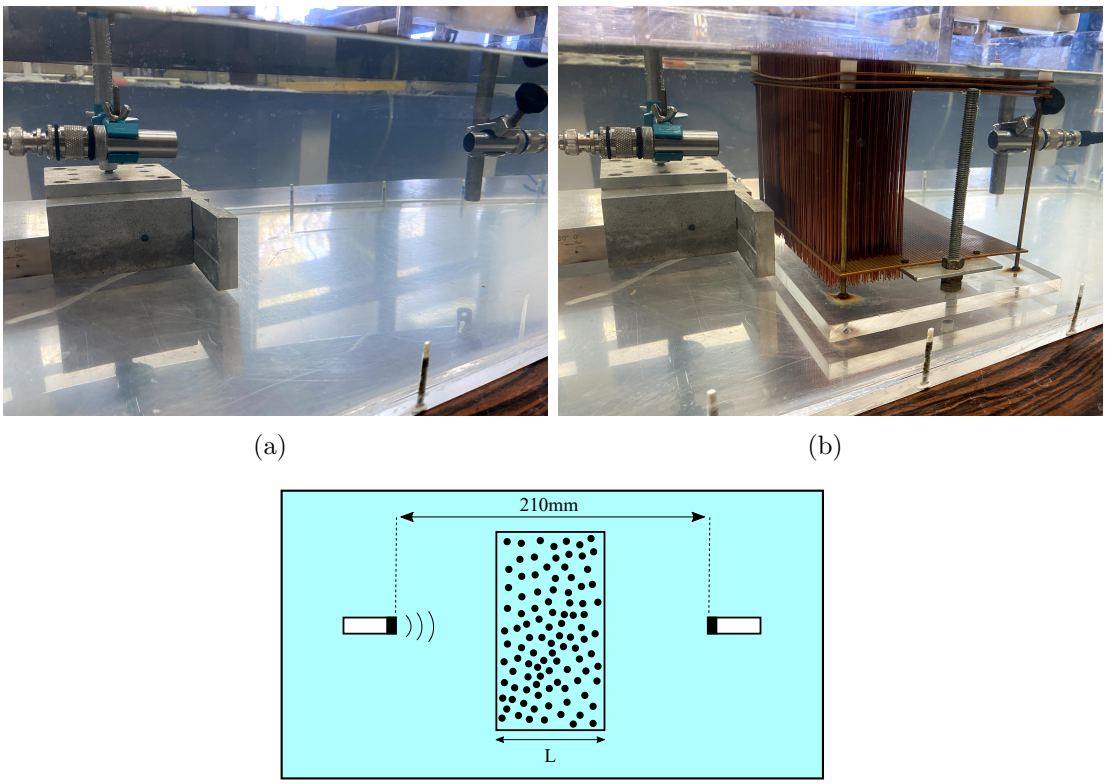


Figure 1.2: Experimental setup used for the measurement of the scattering mean free path. (a) and (b) Photographs of the experimental setup. Emitter and receiver are placed 210mm apart, inside a tank filled with degassed water. Between the transducers is placed the multiple scattering medium, which has a width of 175mm and a depth varying between 24mm and 75mm. (c) Schematic representation of the setup, including the distances considered during the measurements.

1.2.2 Measurement of scattering mean free path

The excitation signal is a 3-cycle sinusoid with a central frequency of 1.0MHz. The acoustic transmission through the medium is measured for five different values of L. For each of the values considered, we measure the transmission through twelve different configurations of disorder. The coherent contribution of the wave arises after configurational averaging. Followed by the calculation of the transmitted coherent intensity, we calculate the scattering mean free path of the system.

In the first instance, the transmission between emitter and receiver is measured through water as reference. This transmission and its time spectrum are shown in figure 1.3. Then, the multiple scattering system is placed between the emitter and receiver to measure the transmission through it. To consider the different disorder configurations,

the system is laterally translated a distance greater than the wavelength in water for the working frequency ($\lambda = c/f = 1.5$mm). By calculating the average transmitted wave along the different disorder configurations for different values of L, the transmitted coherent wave as a function of system depth can be calculated. Figure 1.4 presents the coherent transmission for each value of L along with its respective spectrum over time. On figure 1.5, a comprasion between the transmission through the system in a single disorder configuration and the coherent transmission after averaging over many configurations is presented. In it is seen that the average wave still contains incoherent contribution for later times. The cancelllation of the incoherent contribution is not total since the average is carried out for only twelve different configurations.

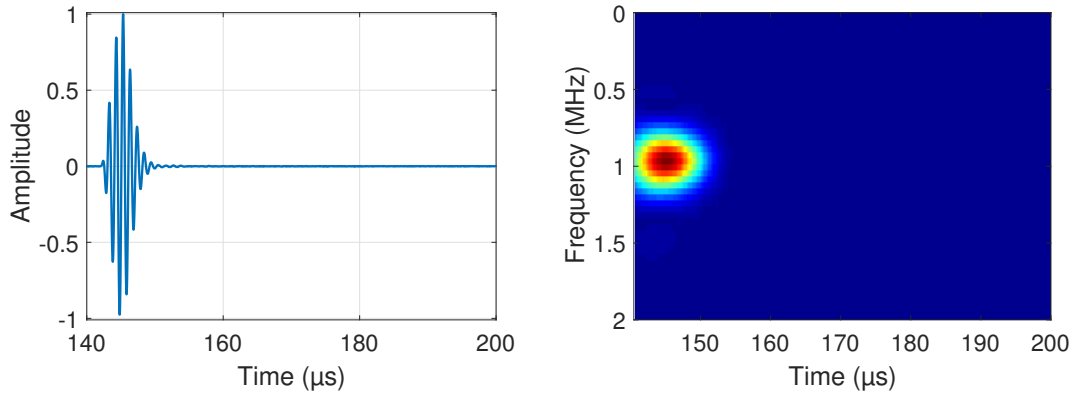


Figure 1.3: Transmitted wave through water. Emitted signal corresponds to a 3-cycle sinus with central frequency 1MHz. (a) Transmission in the time domain. (b) Frequency-time map of the transmitted wave.

Comparing the signal acquired for a particular disorder configuration with the average over many different configurations, it can be seen that the initial arrival is approximately identical. It is referred to as the ballistic wave.

To study the transmitted coherent energy, we have applied two processing methods. On the one hand, the coherent energy is calculated by integrating over time the average transmitted intensity [7]. On the other hand, the coherent energy is calculated by considering the maximum of the spectrum of the average transmitted intensity. As will be presented in the next section, it is pertinent to distinguish both methods, mainly when there is more than one central frequency in the acquired signals. In particular, since the transport parameters depend mostly on the central frequency, the calculation through the signal spectrum is an alternative method to validate the model used [10, 11].

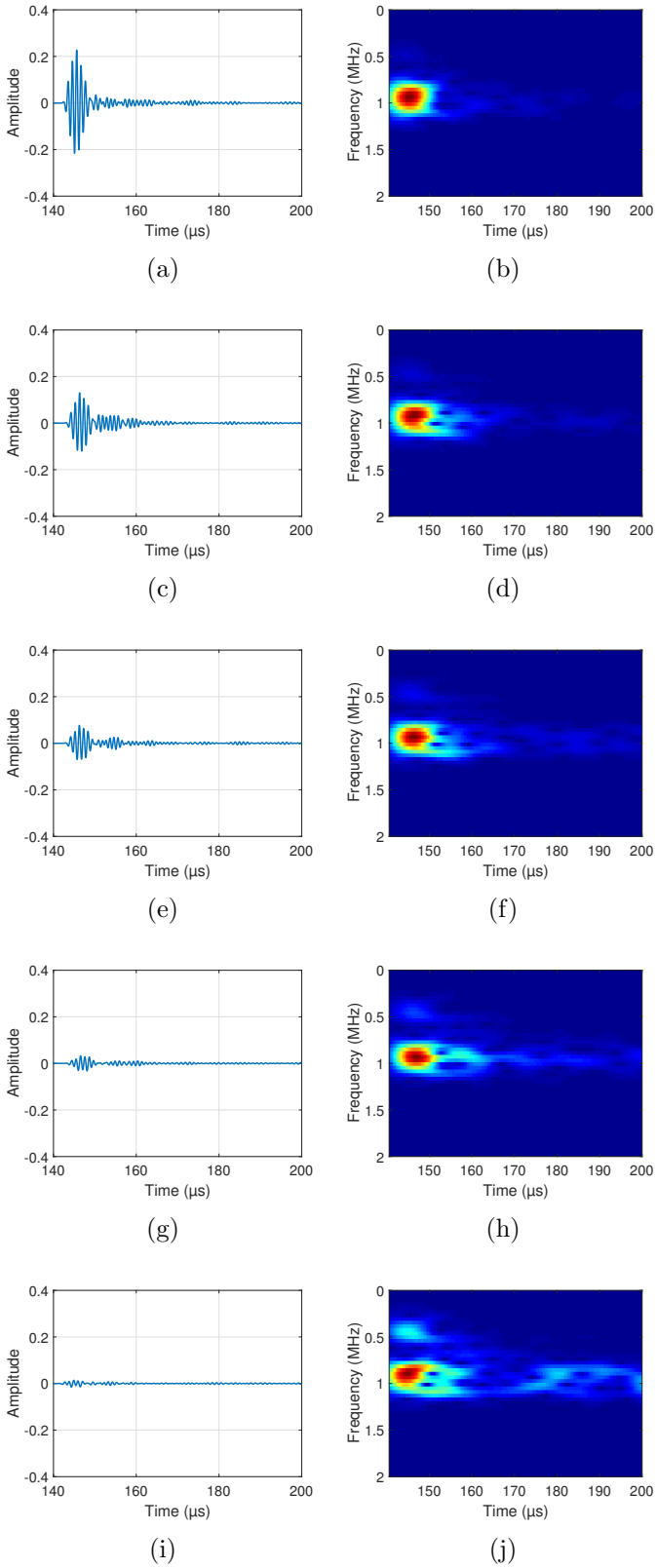


Figure 1.4: Average over 12 configurations of the transmitted wave through the multiple scattering system varying the width L of it. (a) and (b) $L = 24$mm. (c) and (d) $L = 37$mm. (e) and (f) $L = 49$mm. (g) and (h) $L = 62$mm. (i) and (j) $L = 75$mm.

First, the coherent energy was calculated by integrating the transmitted acoustic waves

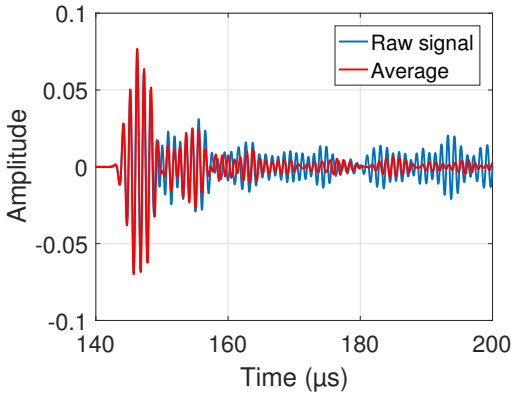


Figure 1.5: Comparison between transmitted wave through a disordered configuration (blue curve) with the average over twelve different configurations (red curve). The thickness used in this case is $L = 49$mm.

squared over time. Then, the dependence of the energy on the depth of the medium L was determined on a logarithmic scale. The data are fitted by a linear regression using the least-squares method, where the slope is related to the scattering mean free path according to the equation (1.12). The fit of the experimental data is presented in Figure 1.6. With this method, the value obtained for the scattering mean free path is

$$\ell_S = (10.05 \pm 0.37)\,\text{mm}, \tag{1.20}$$

where the errorbar comes from the fit.

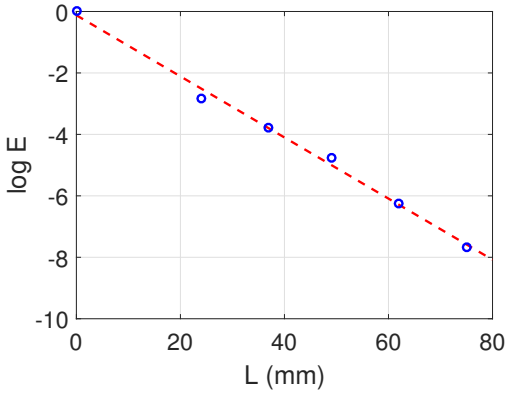
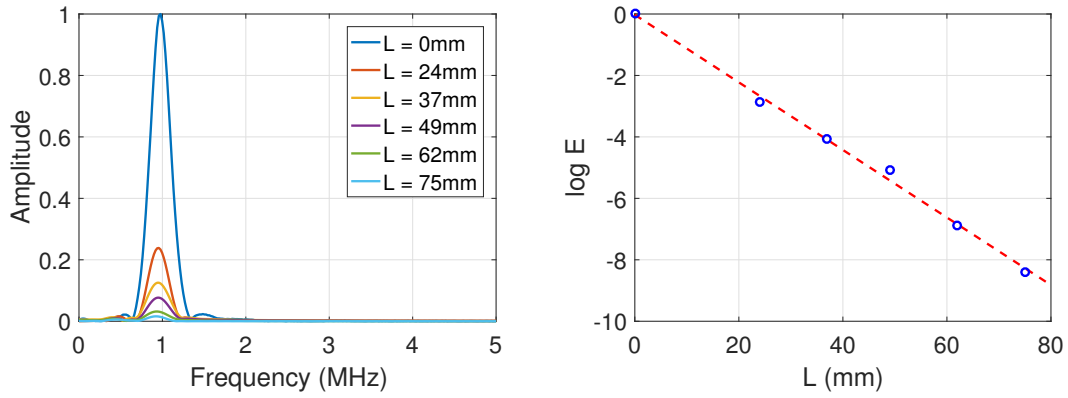


Figure 1.6: Fit of the experimental data for the coherent energy transmitted through the multiple scattering medium by varying L. The energy is calculated by integrating the entire signal in the time domain, in logarithmic scale. The value obtained for the mean free path of scattering from the slope of the fit is $\ell_S = (10.05 \pm 0.37)$mm.

On the other hand, the transmitted coherent energy is calculated by taking the squared amplitude of the spectrum at the central frequency. Figure 1.7(a) shows the spectrum of the transmitted coherent wave for different values of L. Proceeding to the energy calculation, again a linear regression using the least-squares method is used to fit the dependence of the coherent energy in terms of L, in logarithmic scale (see figure 1.7(b)).

Relating the slope of the regression to the elastic mean free path, the value obtained is

$$\ell_S = (9.65 \pm 0.42)\,\text{mm}. \tag{1.21}$$



(a) (b)

Figure 1.7: Data fitting for the coherent transmitted energy through the multiple scattering medium varying L. (a) Spectrum in terms of L. (b) Coherent energy calculated from the spectrum in log scale. The obtained value for the mean free path with the fit is $\ell_S = (9.65 \pm 0.42)$mm.

The two values obtained for the different methods chosen are very similar. However, in order to have a good reference, we resort to an analytical model. The simplest model that can be chosen for the experiment presented is a dilute medium composed of parallel rigid cylinders [12]. For the rigid cylinders, the pressure of the scattered wave field ψ_s far from the cylinder surface, for azimuthal angle ϕ, is proportional to

$$\psi_s(\phi) \propto \sum_{m=0}^{\infty} \epsilon_m \cos(m\phi) \sin(\gamma_m)\, e^{-i\gamma_m}, \tag{1.22}$$

where $\epsilon_0 = 1$ and $\epsilon_m = 2$ for $m > 0$. Meanwhile, γ_m is defined as

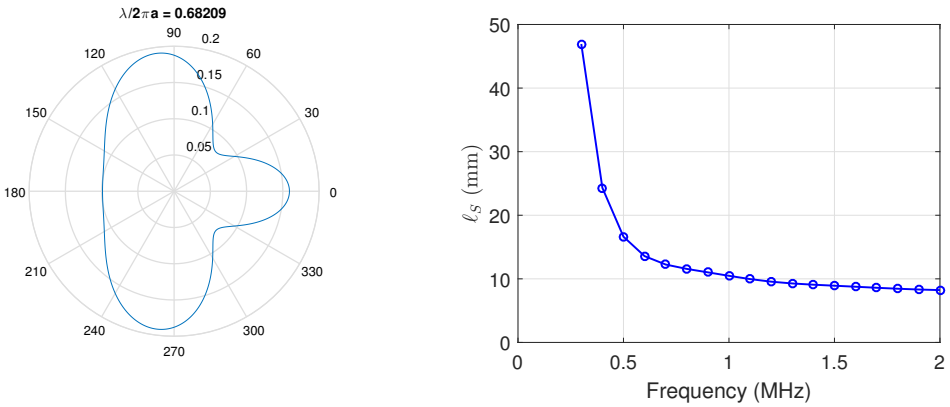
$$\tan\gamma_m = \begin{cases} \frac{J_1(ka)}{N_1(ka)} & m = 0 \\ \frac{J_{m-1}(ka) - J_{m+1}(ka)}{N_{m-1}(ka) - N_{m+1}(ka)} & m > 0 \end{cases},$$

where J_m and N_m are the mth-order Bessel functions, of first and second kind respectively.

In turn, the scattering cross-section $d\sigma(\phi)/d\phi$ can be calculated as a prefactor multiplied by the function $|\psi_s(\phi)|^2$. However, the quantity of interest for our purpose is the total scattering cross section σ_T, which can be calculated as simply as the integral over the angle ϕ. This leads to the expression

$$\sigma_T = \int_0^{2\pi} \frac{d\sigma(\phi)}{d\phi} d\phi = \frac{\lambda}{\pi^2} \int_0^{2\pi} |\psi_s(\phi)|^2\, d\phi, \tag{1.23}$$

where λ is the wavelength.



(a) (b)

Figure 1.8: Calculation of the scattering mean free path using a rigid cylinder model for different frequency values. (a) Scattering cross-sectional pattern of a rigid cylinder of radius $a = 0.35$mm for a frequency of 1.0MHz. (b) The scattering mean free path ℓ_S is calculated using the equation (1.13), with a value for the density equal to the experimental $n = 0.115\text{mm}^{-2}$. For a frequency of 1.0MHz we find a value of $\ell_S = 10.48$mm.

With the total cross-section for a rigid cylinder, we can use equation (1.13) to calculate an analytical value of the scattering mean free path. This calculation is carried out for different frequencies, considering a density of scatterers equal to that of our experiment $n = 0.115\text{mm}^{-2}$. In figure 1.8(a) the cross-section is plotted in the polar angle for $\lambda = 1.5$mm and the cylinder radius used ($a = 0.35$mm); meanwhile, in figure 1.8(b), the elastic mean free path obtained through equation (1.13) for frequencies between 0.3 and 2.0MHz is presented. Using these parameters, the obtained value for the scattering mean free path for a frequency of 1.0MHz is

$$\ell_S = 10.48\text{mm}. \tag{1.24}$$

The value calculated for the scattering mean free path is slightly larger than the one obtained from the experimental results, for the two methods considered. From the analytical calculation of the total effective cross section, under the assumption of rigid cylinders, the experimental results are similar, which means that there are no resonances or internal reflections in the scatterers and, therefore, they can be modeled as completely rigid. This model allows us to conclude that both the dilute system approximation, as well as the rigid cylinder approximation, are well justified for our experimental context.

1.3 Acoustic transmission in 2D multiple scattering compact media

1.3.1 Experimental set-up

Let us now consider a compact 2D multiple scattering system composed of parallel copper cylinders with diameter $d = 0.70\text{mm}$. The rods are arranged vertically between two supports, one at the bottom and the other at the top of the system (see figure 1.9(a)). During the preparation of the system, the number of scatterers is chosen and they are horizontally arranged evenly distributed. Then, the supports are adjusted to retain the cylinders in position, obtaining what is presented in figure 1.9(a). After setup, the surface area occupied by the rods is measured to calculate both density and surface fraction. With this procedure, the medium has an average density of $n = (1.86 \pm 0.04)\,\text{mm}^{-2}$. Likewise, the surface fraction determined for the system is $\eta = (72 \pm 2)\,\%$, which is comparable to the 2D random packing of hard disks $\eta_{\text{RCP}} = (82 \pm 2)\,\%$ [13].

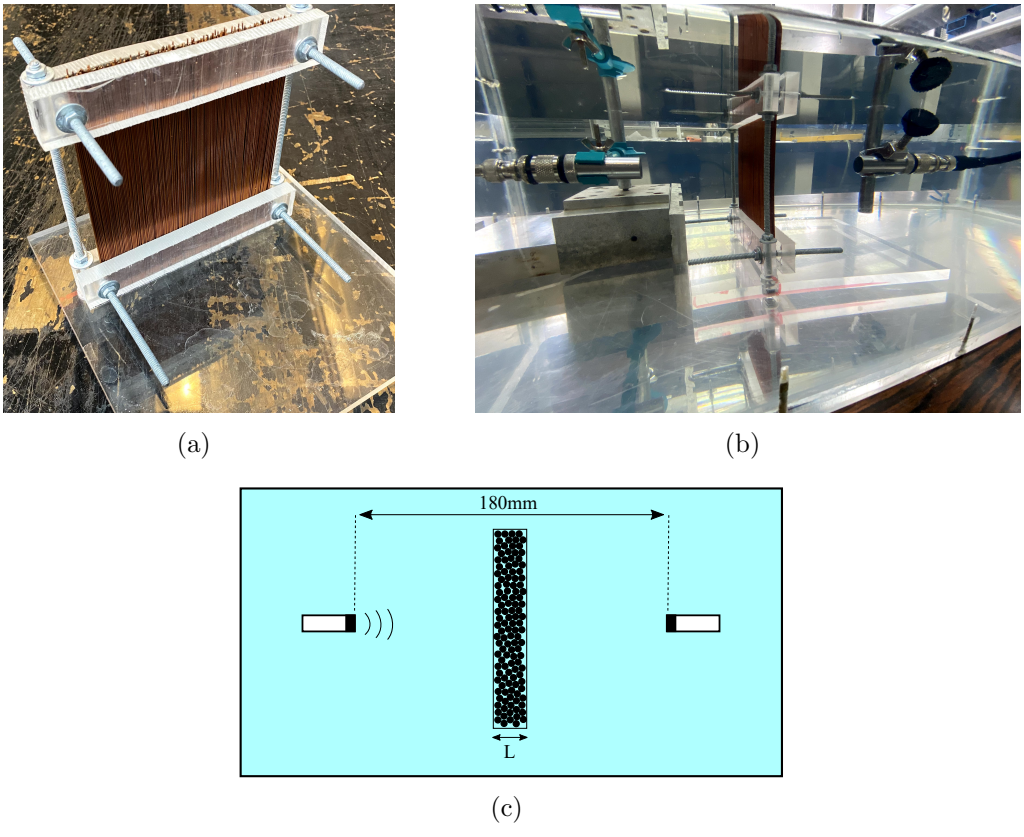


Figure 1.9: Experimental setup used with the compact multiple scattering system. (a) Image of the compact multiple scattering system. (b) Photograph of the experimental setup. (c) Schematic representation of the setup, including the distances considered during the measurements.

The emitter and receiver used are the same as those presented in section 1.2.1; two identical circular *harisonic* I3-0108-S transducers with diameter 12.7mm and central fre-

quency of 1.0MHz. The size of the elements is chosen to emphasize averaging over a larger surface area, as the transmission is expected to be clearly reduced due to the placement of the cylinders in contact. The absence of distance between each scatterer leads to a highly diffused signal, so the amplitude of the transmitted signal is extremely low. The averaging on the transducer surface avoids mixing of the transmitted signal with the background electrical noise, thus presenting an advantage to this type of experimental measurement.

The emitter and receiver are submerged in the tank filled with degassed water, this time placed at 180mm. Between the transducers is placed the multiple scattering system, with a width of approximately 120mm and a depth L varying between $L = 4.4$mm and $L = 8.0$mm. Figure 1.9(b) shows a picture of the experimental setup and 1.9(c) a schematic representation of it.

1.3.2 Experimental results

The initial excitation signal is a 3-cycle sinusoid with central frequency 1.0MHz. The transmitted acoustic wave is measured for ten different disorder configurations, for each size L of the system. The system depth values considered were $L = 4.4$mm, $L = 5.5$mm, $L = 6.2$mm, $L = 7.4$mm and $L = 8.0$mm. The transmission through water is recorded prior to measurement through the system. This transmission is then used as a reference for the rest of the measured signals.

In Figure 1.11 a single transmission through the multiple scattering system is compared with the averaged signal. In contrast to the case of the dilute system, we can see the appearance of a low-frequency ballistic pulse in the received signal, as previously found in densely packed granular media [14], and recently in finite difference numerical simulations for a 2D system of densely packed scatterers [15]. This low-frequency contribution can be attributed to the "wall" effect produced by the dense packing of scatterers, which enhances the propagation of longer wavelengths. The longer wavelength is not sensitive to the scatterers in the dense packing arrangement along its propagation, thus it sees the medium as an effective one.

Figure 1.10 shows the average transmitted signals and their respective spectrograms for the different values of L used. From the spectrograms it can be seen that the energy is distributed between two central frequencies: 0.4MHz and 1.0MHz. As L increases, the contribution of the lower frequencies becomes dominant, until the central frequency is almost extinguished for $L = 7.4$mm.

The transport parameters, usually, depend on the frequency; this is why, having two different spectral components, we will not obtain a well-defined value for the parameters when calculating the coherent energy by integration. However, it is possible to proceed to calculate the transmitted energy by resorting to its spectrum, differentiating the contributions of both frequencies separately.

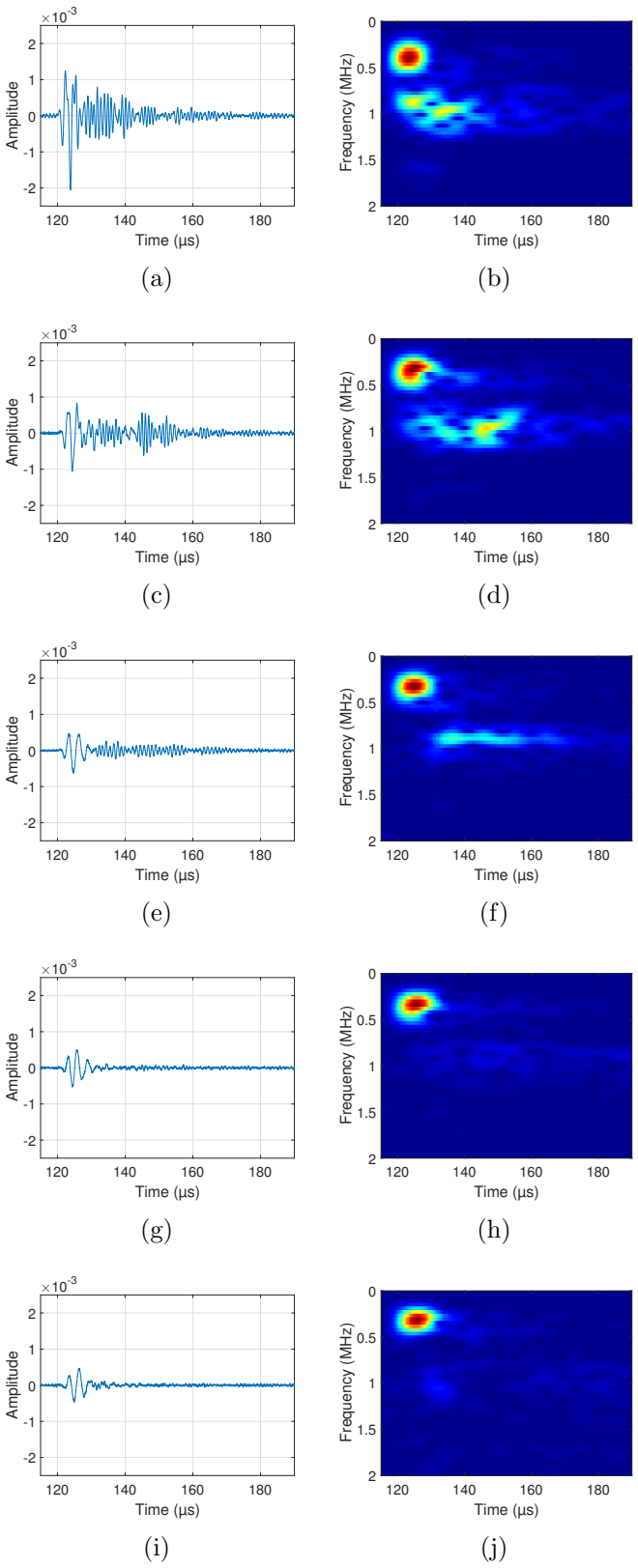


Figure 1.10: Average over 10 configurations of the transmitted wave through the multiple scattering system varying the width L of it. (a) and (b) $L = 4.4$mm. (c) and (d) $L = 5.5$mm. (e) and (f) $L = 6.2$mm. (g) and (h) $L = 7.4$mm. (i) and (j) $L = 8.0$mm.

Figure 1.12(a) presents the spectrum of the average transmitted signals for each value

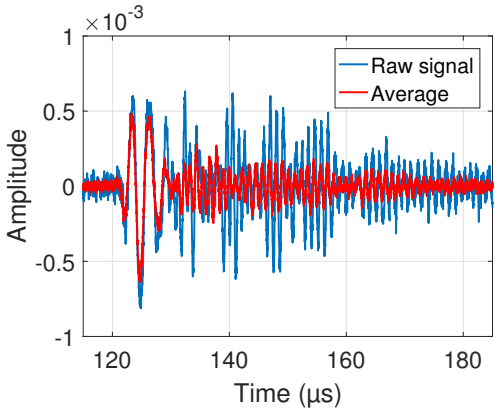


Figure 1.11: Comparison between transmitted wave through a disorder configuration (blue curve) with the average over ten different configurations (red curve) for a depth of $L = 6.20$mm.

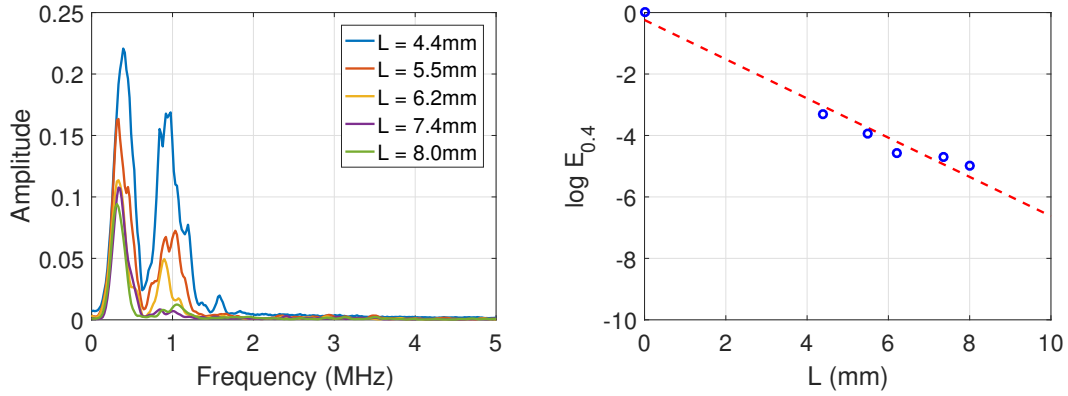


Figure 1.12: Data fit for coherent energy transmitted through the compact multiple scattering medium varying L. (a) Spectrum in terms of L. (b) Coherent energy for 0.4MHz calculated from the spectrum. In logarithmic scale, the linear least-squares fit is performed. The value obtained for the scattering mean free path from the fit is $\ell_S = (1.57 \pm 0.13)$mm.

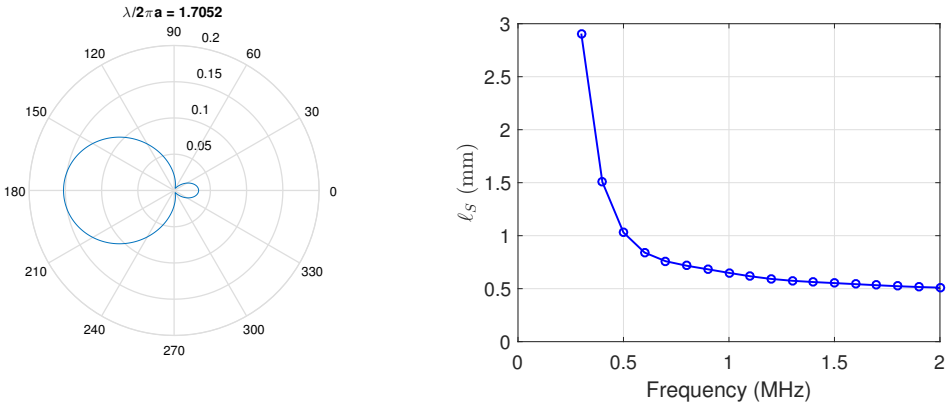
of L. It can be clearly seen that the coherent wave has two frequency components, centered at 0.4MHz and 1.0MHz. For the low frequency, the transmitted coherent energy is calculated from the spectrum, as was done earlier in the previous section. The energy is calculated around 0.4MHz. Figure 1.12(b) presents the fit for the energy in terms of the depth L (in logarithmic scale). The normalization of the energy is performed with reference to the transmission through water. For this frequency we see a good agreement between the fit and the experimental data. Using a linear regression, we obtain from the slope a value for the scattering mean free path of

$$\ell_S = (1.57 \pm 0.13)\,\text{mm}. \tag{1.25}$$

As proceeded in the previous section, an analysis of the expected scattering mean free path, given the experimental parameters, considered was performed. First, let us assume

that the model given by the equation (1.13) remains valid for our close-packed system, at least for the lower frequency. Considering our scatterers as rigid cylinders, the scattering cross-section can be calculated by the equation (1.22). Considering the cylinder radius $a = 0.35$mm and the density of scatterers as $n = 1.86$ scatterers/mm^2, the calculation of the total scattering cross-section was performed, and the scattering mean free path was estimated for a frequency range between 0.3MHz and 2.0MHz (see figure 1.13). The value obtained for ℓ_S for 0.4MHz is

$$\ell_S = 1.503\text{mm}. \tag{1.26}$$



(a) (b)

Figure 1.13: Calculation of the scattering mean free path using a rigid cylinder model for different frequency values. (a) Differential scattering cross section pattern for a rigid cylinder of radius $a = 0.35$mm, at a frequency of 0.4MHz. (b) The scattering mean free path ℓ_S is calculated via the equation (1.13), using a value for the density of scatterers equal to the experimental one $n = 1.86\text{mm}^{-2}$. For a frequency of 0.4MHz the obtained value of the scattering mean free path is $\ell_S = 1.503$mm.

Surprisingly, the result obtained from the dilute system model agrees well with the experimental results. The experimental value obtained for the scattering mean free path is quite close to that calculated from the dilute system model, for a frequency of 0.4MHz. For this frequency, we have a wavelength in water of about 3.75mm. If we compare this value with the size of the scatterers, $d = 0.7$mm, we can interpret that the wave does not "see" each scatterer by itself, but an effective medium instead. This fact allows us to use the dilute medium approximation, together with the assumption of rigid cylinders, for accurately estimating the value of the scattering mean free path for our experimental conditions.

On the other hand, for the 1.0MHz frequency we have to go one step further and perform different data processing. For this frequency, the wave undergoes enough scattering events to assume that it has entered a diffusive regime, as introduced in section 1.1.2. Such a propagation regime prevents us from proceeding with the dilute medium

model, not only because we are working with a compact system (which goes against the main idea of such approach), but because in this regime the coherent wave is practically extinguished (as shown in figure 1.10 for large values of L).

To address this propagation regime, it is necessary to consider the second momentum of the Green's function: the average over the disorder of the acoustic intensity. In our case, the coherent wave is mainly formed by a frequency lower than the central frequency. Therefore, given a fixed L, the coherent wave was subtracted from all acquired transmissions. Thus, the remaining signal is primarily the multiple scattered coda wave.

In this context, a solution for the diffusion equation, for the aligned transmitter and receiver and a medium size L, is given by the one-dimensional analytical solution expressed by [16]

$$I(t) \propto \frac{U_0}{2L} e^{-t/\tau_a} \sum_{n=0}^{\infty} \frac{(-1)^n}{\delta_n} \cos\left(\frac{n\pi\ell^*}{L}\right) \exp\left[-\left(\frac{n\pi}{L}\right)^2 Dt\right]. \tag{1.27}$$

With such a model, we get a measurement of the transport parameters involved in wave propagation. For $L = 8.0$mm in particular, the experimental data obtained for the average transmitted intensity is fitted with expression (1.27) (see figure 1.14). With this model, and assuming that the transport velocity is equal to the propagation velocity in water, we are able to measure the absorption mean time, the diffusion constant and to infer (using relation (1.18)) the transport mean free path. The values determined this way are

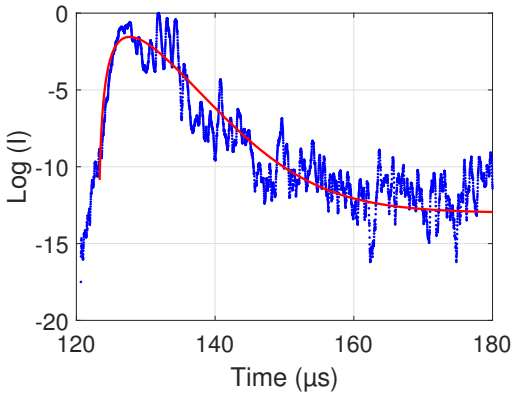


Figure 1.14: Fitting of average transmitted multiple scattered intensity for $L = 8.0$mm. The experimental data is fitted using equation (1.27), allowing to determine the transport parameters absorption time τ_a and the diffusion constant D.

$$\begin{cases} \tau_a = (10.0 \pm 0.2)\,\mu\text{s} \\ D = (1.12 \pm 0.02)\,\text{mm}^2/\mu\text{s} \\ \ell^* = (1.49 \pm 0.03)\,\text{mm} \end{cases} \tag{1.28}$$

With this model we were able to determine the transport parameters involved for the

frequency considered. As a reference, it is pertinent to consider the work carried out by Ma et al. [15]. The authors obtained experimental results for the transport mean free path that are of the same order as our experiments. Therefore, we may say that the assumption of a transport velocity comparable to the propagation velocity in water is reasonable.

Using a diffusion model we were able to measure the transport parameters of the system for the working frequency. Since the effective medium model is no longer valid for such frequency value, it is the second momentum analysis that gives us the necessary information to determine the parameters that characterize the medium in our experimental conditions.

1.4 Discussion and conclusions

Throughout this chapter we have studied the multiple scattering properties of two different systems: a dilute medium and a close-compact medium. Both sets of experiments were counterposed to the dilute medium approach. The parameter chosen to analyze our experimental results was the scattering mean free path, described by the equations (1.12) and (1.13).

The model was shown to be valid for the dilute system case, as presented in section 1.2. Using a system composed of parallel copper rods, we determined the scattering mean free path by varying the thickness of the medium. The experimental results obtained are in good agreement with what is expected from the dilute medium approximation and the rigid cylinder assumption. The value experimentally determined for ℓ_S is quite close to that estimated by the theoretical predictions.

In the close packing system the situation is different. By bringing the parallel cylinders closer together, we increased the surface fraction of the medium by a factor of almost fifteen times. Thus, as described in equation (1.13), there is a huge decrease in the elastic mean free path.

Increasing the number density of scatterers has several consequences. The most trivial one is that the approximation of a dilute medium is no longer applicable. Likewise, the appearance of a low-frequency ballistic wave becomes evident when analyzing the first momentum of the Green's function. This phenomenon has already been seen in granular media [14]. However, this low-frequency does not undergo such strong dispersion, as detailed in section 1.1. What is interesting in the transition from the dilute to the compact system is how the lower frequencies survive in transmission through the medium, emerging a low-frequency transmitted coherent wave. In particular, in our experiments, a low-frequency coherent wave survives transmission and averaging of disorder configurations, with a central frequency of 0.4MHz. Surprisingly, for this frequency value, the dilute medium approach still works. The values obtained for the scattering mean free path

are the same for both the experimental and the dilute medium model composed of rigid cylinders.

For the central frequency, the analysis of the experimental data is more complex. Since there is no coherent wave observable, we were forced to resort to an analysis of the sencond momentum of our transmitted signal. Using a solution to the diffusion equation, given by the expression (1.27), the experimental results were processed and the corresponding fit was made to the multiple scattered intensity data, averaged over different disorder configurations. In such a context, we were able to perform an estimation of the transport parameters involved in the acoustic wave propagation regime, obtaining experimental values comparable with those obtained by Ma et al. for a system composed of non-contact cylinders [15].

The transition between dilute and compact media is of special interest, since there is no physical model that fully explains wave propagation through complex media for a close-packed multiple scattering system. An optimization to consider is to analyze such a transition more smoothly by handling the mean distance between scatterers more accurately.

From this set of experiments we can conclude two things about the transition from dilute to compact media. First, increasing the number density of scatterers implies a strengthening of scattering and, thus, a decrease in the scattering mean free path. Secondly, a strong dispersion affects the wave transmission as a low-pass filter, which makes emerge a low-frequency coherent component as a primordial contribution to the transmitted signals through a dense-packed multiple scattering media.

References

[1] Keiiti Aki and Bernard Chouet. Origin of coda waves: source, attenuation, and scattering effects. *Journal of geophysical research*, 80(23):3322–3342, 1975.

[2] Ludovic Margerin, Michel Campillo, and Bart Tiggelen. Radiative transfer and diffusion of waves in a layered medium: new insight into coda q. *Geophysical journal international*, 134(2):596–612, 1998.

[3] Stelio Haniotis, Pierre Cervenka, Carlos Negreira, and Jacques Marchal. Seafloor segmentation using angular backscatter responses obtained at sea with a forward-looking sonar system. *Applied acoustics*, 89:306–319, 2015.

[4] Arnaud Tourin, Geoffroy Lerosey, Julien de Rosny, Arnaud Derode, and Mathias Fink. Time reversal telecommunications in complex environments. *Comptes Rendus Physique*, 7(7):816–822, 2006.

[5] Philip W Anderson. Absence of diffusion in certain random lattices. *Physical review*, 109(5):1492, 1958.

[6] Ping Sheng. *Introduction to wave scattering, localization and mesoscopic phenomena*, volume 88. Springer Science & Business Media, 2006.

[7] Arnaud Tourin, Arnaud Derode, Aymeric Peyre, and Mathias Fink. Transport parameters for an ultrasonic pulsed wave propagating in a multiple scattering medium. *The Journal of the Acoustical Society of America*, 108(2):503–512, 2000.

[8] Ad Lagendijk and Bart A Van Tiggelen. Resonant multiple scattering of light. *Physics Reports*, 270(3):143–215, 1996.

[9] Yamil Abraham. Estudio y caracterización de inversión temporal acústica a través de medios de scattering múltiple. 2017.

[10] Nicolas Viard, Bruno Giammarinaro, Arnaud Derode, and Christophe Barriere. Coherent transmission of an ultrasonic shock wave through a multiple scattering medium. *Physical Review E*, 88(2):023201, 2013.

[11] Gonzalo Garay, Nicolás Benech, Yamil Abraham, and Carlos Negreira. Nonlinear wave propagation through multiple scattering media and virtual time reversal focusing. *The Journal of the Acoustical Society of America*, 148(3):1315–1324, 2020.

[12] Philip McCord Morse and K Uno Ingard. *Theoretical acoustics*. Princeton university press, 1986.

[13] James G Berryman. Random close packing of hard spheres and disks. *Physical Review A*, 27(2):1053, 1983.

[14] Xiaoping Jia, C Caroli, and B Velicky. Ultrasound propagation in externally stressed granular media. *Physical Review Letters*, 82(9):1863, 1999.

[15] Qingqing Ma, Xiasheng Guo, Xiaoping Jia, Arnaud Tourin, and Dong Zhang. Ultrasonic multiple scattering parameters of densely packed cylinders immersed in water. *Acta Acustica*, 46(6):1178–1184, 2021.

[16] Xiaoping Jia. Codalike multiple scattering of elastic waves in dense granular media. *Physical Review Letters*, 93(15):154303, 2004.

Chapter 2

Time-reversal focusing in immersed granular media for wave transport study

Contents

2.1 Intensity wave transport in immersed granular media 30

2.1.1 Diffusive transport 30

2.1.2 Coherent backscattering cone 39

2.2 Time-reversal as a means to measure transport parameters . 50

2.2.1 Fundamentals of time-reversal 50

2.2.2 Link between time-reversal and transport parameters 54

2.2.3 Physical model 55

2.2.4 Stationary time-reversal 63

2.2.5 Dynamic time-reversal 68

2.3 Discussion and conclusions 72

References 74

In Chapter 1, we first study the propagation of ultrasound waves through a dilute 2D multiple scattering system formed by a set of copper rods immersed in water. Then, we present experimental results in a compact 2D system formed by the same rods but in a dense packing. This allowed us to reveal the change in ballistic wave behavior when moving from a dilute to a compact multiple scattering medium.

In this chapter, we focus our attention on the transport properties of a three-dimensional compact multiple scattering system consisting of a granular medium immersed in water. We present measurements of the transport parameters by two classical

methods, exploiting the average transmitted intensity and the Coherent Backscattering Effect (CBE), respectively. Finally, we present an original method to measure transport parameters based on the time-reversal focusing of acoustic waves.

2.1 Intensity wave transport in immersed granular media

2.1.1 Diffusive transport

J. Page et al. [1] have tested the application of the diffusion approximation to describe the propagation of ultrasonic waves through a submerged granular medium. In their experiment, a multiple scattering system consisting of a dense packing of glass beads is irradiated with a short ultrasonic pulse. The beads have a diameter of 1.0mm and are contained between thin disk-shaped cells. The emitted pulse is a 10-cycle signal with central frequency of 2.5MHz. In water, such frequency corresponds to a wavelength of $\lambda \simeq 0.6$mm. The transmitted acoustic wavefield is measured on the source axis with a hydrophone, whose diameter is less than the ultrasonic wavelength. Then, the transmitted intensity is averaged over different configurations of disorder. The configurations are changed by translating lateraly the multiple scattering medium. These measurements are repeated for different thicknesses L of the medium. The time-of-flight distribution measured for the average intensity, for three different sizes L, is shown in Figure 2.1. As the sample thickness increases, the peak decreases and is delayed in time.

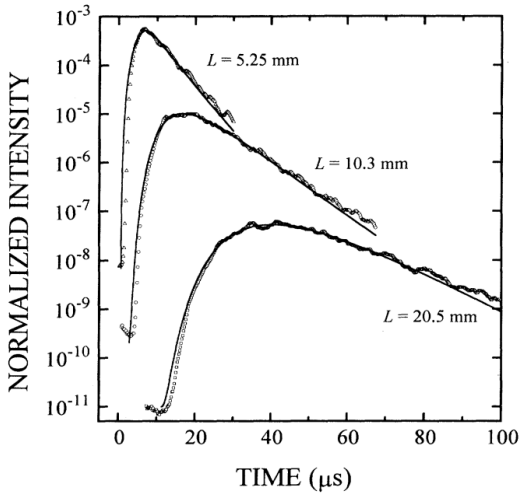


Figure 2.1: Time profile of the average intensity transmitted through a random close packed suspension of glass beads for three sample thicknesses L. The smooth and solid curves are the best least-squares fits to the diffusion theory, resulting in $D = (0.43 \pm 0.02)\,\mathrm{mm}^2/\mu\mathrm{s}$ and $\tau_a = (12 \pm 1)\,\mu\mathrm{s}$. Figure taken from [1].

The average transmitted intensity is fitted using the solution of the diffusion equation.

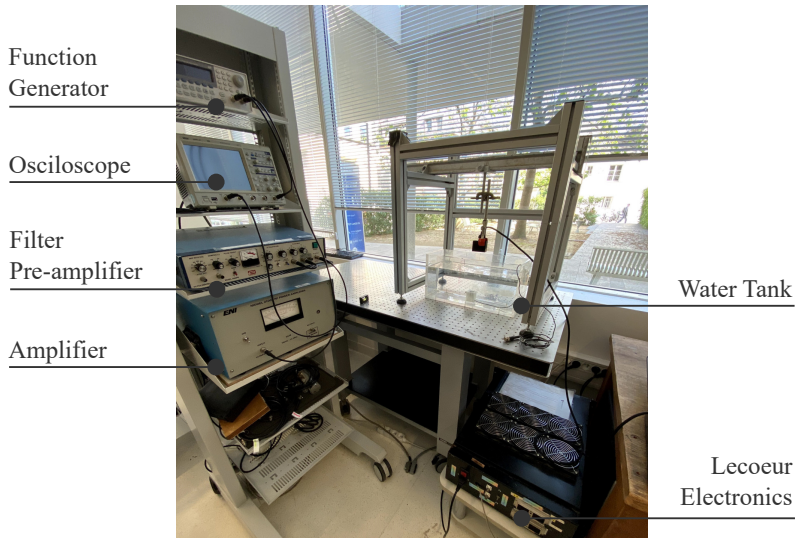
The energy flux is obtained from such solution for the energy density in a sample of thickness L, unbounded in the transverse directions. The least-squares fit gives consistent values for the transport parameters: $D = (0.43 \pm 0.02)\,\mathrm{mm}^2/\mu\mathrm{s}$ and $\tau_a = (12 \pm 1)\,\mu\mathrm{s}$. Furthermore, one can consider the transport mean free path to be equal to the penetration depths z_0. The first one can be interpreted as the distance after which the wave has lost its memory (i.e., its coherence). The second is the distance the wave has to travel before diffusion begins. Therefore, both lengths are closely related, allowing one to consider them the very same. The value for ℓ^* is determined from the measurement of the absolute transmission of a long wave train, obtaining $\ell^* = (0.80 \pm 0.05)\,\mathrm{mm}$.

The results obtained by the authors are a consistent proof of the validity of the diffusion approximation. From the time profile of the average transmitted intensity they determine both D and τ_a; meanwhile, from the absolute transmission, they determine ℓ^*. With these parameters, the transport velocity is then calculated as $v_T = 3D/\ell^* \simeq 1.6\mathrm{mm}/\mu\mathrm{s}$. Interestingly, the transport velocity is close to the measured velocity of ballistic propagation $1.7\mathrm{mm}/\mu\mathrm{s}$, both close to the speed of sound in water $1.5\mathrm{mm}/\mu\mathrm{s}$. As it will be described in the following section, these results will be the foundations for our own experiments in immersed granular packing.

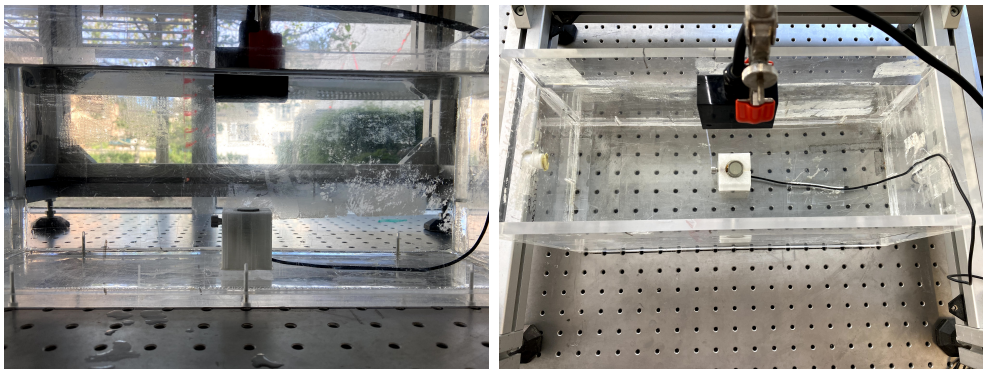
Experimental setup

Let us consider a random close-packed suspension of monodisperse glass beads, immersed in a water tank of 400mm long, 150mm deep and 200mm high. The beads were placed in the bottom of the tank and carefully mixed to ensure the randomness before each experiment. We consider the volume fraction to be near the random close-packing limit, i.e., about 60%. Two different bead diameters were used throughout the experiments presented in this chapter: 1.5mm and 5mm.

An array made of piezoelectric elements and a single element transducer were used to emit/receive acoustic waves. The transducer array consists of 128 rectangular elements of 0.315mm width and 15.0mm height each, with a pitch of 0.375mm and a total length of approximately 50.0mm, with a central frequency of 2.0MHz. Using a *Lecoeur Electronics* transmit/receive equipment, 64 channels of the array can be handled independently. The single-element transducer consists of a rectangular piezoelectric element of dimensions 0.50mm × 12mm, with a central frequency of 1.5MHz. A support made with a 3D printer holds the single element transducer at the bottom of the water tank. This element is manipulated by a set of equipment consisting of a function generator (Agilent 3320A), a 50dB RF amplifier (ENI model 2100L power amplifier) for emission, and an oscilloscope (LeCroy WaveJet 324a) and an analog filtering and pre-amplification device (Panametrics Pulser-Receiver model 5058PR) for reception. In figure 2.2 the described set-up is presented together with the emission/reception instruments utilized.



(a)



(b) (c)

Figure 2.2: (a) Picture of the experimental setup and devices utilized. (b) and (c) Water tank with the experimental arrangement of the emitter and receiver.

To proceed with the experimental measurements, the transducer array was placed in contact with the granular medium (see figure 2.3). Using a single channel of the array as the emitter and the mono-element transducer as the receiver, transmission measurements were taken for different distances L between them. Both emitter and receiver are manualy aligned before immersing the granular medium. Figures 2.3(a) and 2.3(b) show the pictures of the experimental setup, while figure 2.3(c) shows a schematic representation of it.

Experimental results

The central channel of the array excites the multiple scattering medium by emitting a 2-cycle sine wave with a central frequency of 2.0MHz, and the transmitted waveform is recorded by the single element transducer. The emission/reception was repeated for $N = 8$ different sample configurations for averaging. The whole sequence was then repeated for three different depths L. The chosen values for L were 25mm, 20mm and 15mm. These

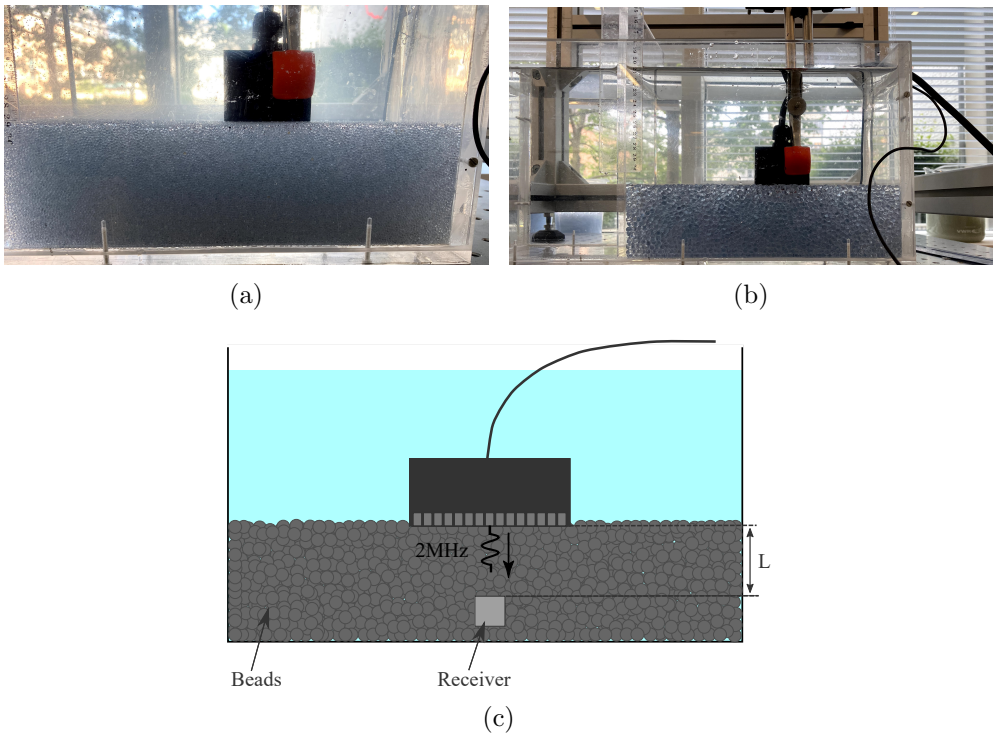


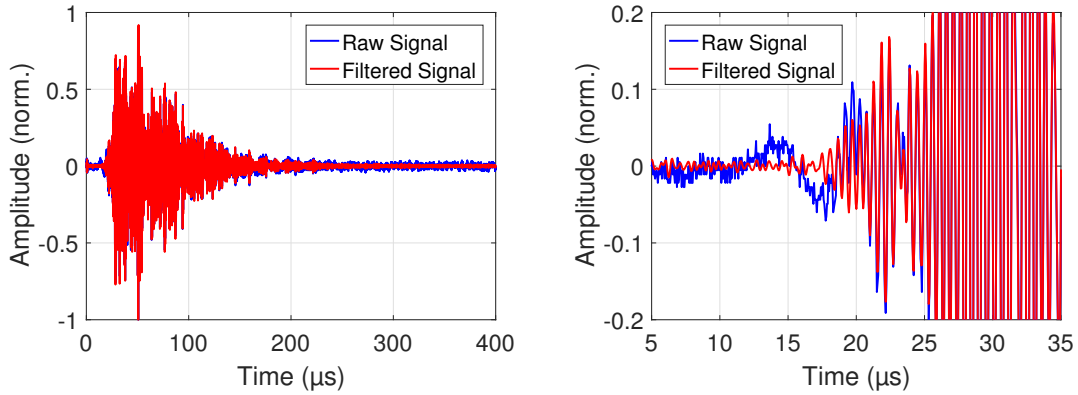
Figure 2.3: Pictures of the experimental setup for (a) 1.5mm and (b) 5mm beads. (c) Schematic figure of the setup. In this case, the bead packing height was kept constant and the distance L between emitter and receiver was modified.

measurements were performed for the two different bead sizes.

The acquired signal is composed of a low-frequency coherent pulse followed by a higher frequency coda wave, for the 1.5mm beads. This original observation is reminiscent of that reported in Chapter 1 for a 2D compact medium. The signal is computationally filtered with a bandpass between 1.0MHz and 3.0MHz, to eliminate the low-frequency ballistic contribution of the signal as well as to decrease the electronic noise introduced by the measuring elements. Figure 2.4(a) shows the comparison between a raw acquired signal and the same but filtered. In figure 2.4(b) a zoom near the first arrival is shown to evidence the presence of the low-frequency ballistic transmission. In this case, the acquired signal was for the 1.5mm diameter beads with a distance $L = 25$mm between emitter and receiver.

The transmitted intensity is calculated for every acquired signal, and then averaged over the N different configurations. Due to the low value chosen for N, after averaging there are still significant signal fluctuations in the average intensity that do not vanish. Therefore, to avoid this issue, the time of flight distribution is computationally smoothed by averaging using a sliding time window, to remove high frequency fluctuations.

The time of flight distribution is fitted using a solution of the diffusion equation model. For our experimental conditions, we consider the half-space in $z \geq 0$, where a point-like source located at the origin emits a Dirac's delta at $t = 0$. The receiver is located inside



(a) (b)

Figure 2.4: Transmitted signal for beads of 1.5mm diameter and a distance between emitter and receiver of $L = 25$mm. (a) Comparison between raw and bandpass filtered signals. (b) Zoom around arrival time to evidence the presence of coherent low-frequency contribution and how it is erased after filtering.

the multiple scattering medium at position $z = L$. Under these boundary conditions, the time of flight distribution in the z-axis is [2]

$$I(t) \propto \frac{e^{-t/\tau_a}}{(Dt)^{3/2}} \left[e^{-(\ell^* - L)^2/4Dt} - e^{-(\ell^* + L + 2z_0)^2/4Dt} \right], \tag{2.1}$$

where τ_a is the absorption time, ℓ^* the transport mean free path, D the diffusion coefficient and z_0 the penetration depth.

In order to decrease the amount of parameters involved, the following assumptions were considered. On the one hand, the penetration depths is expected to be approximately equal to the transport mean free path [1]. Hence, we fixed $z_0 \simeq \ell^*$. On the other hand, the transport mean free path is linked to the diffusion coefficient by the transport velocity v_T. As we proceeded in the previous Chapter, we will consider the transport velocity to be of the same order of magnitude than the propagation velocity in the homogeneous medium, i.e., in water. Thus, considering that v_T is equal to the velocity in water $c = 1.5\text{mm}/\mu\text{s}$, from equation (1.18) the transport mean free path is written as

$$\ell^* = \frac{3D}{c}. \tag{2.2}$$

With these assumptions, the remainning independent parameters are only the absorption time τ_a and the diffusion coefficient D. Assuming that the Thouless time is much larger than the absorption time, this latter governs the decay of the time of flight distribution at late times (equation (2.1)). Thus, it can be inferred by a linear fit in a logarithmic scale of the average intensity distribution. In figure 2.5 the time of flight distribution with its corresponding fit is presented for each value of L.

The transport parameters calculated from the fit of the data are in good agreement,

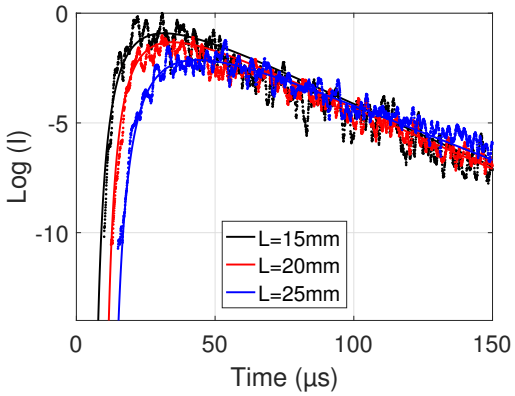


Figure 2.5: Time of flight distribution in logarithmic scale for different distances between emitter and receiver. In dots are shown the experimental data; in solid line the fit model from the solution to the diffusion equation. The transport parameters obtained from the fitting are $D_{1.5\text{mm}} = (0.96 \pm 0.05)\,\text{mm}^2/\mu\text{s}$ and $\tau_a^{1.5\text{mm}} = (23 \pm 1)\,\mu\text{s}$.

obtainning approximately the same values for the different distances between emitter and receiver L. Considering the mean value as the most representative and the largest error as the error range, the obtained set of parameters is

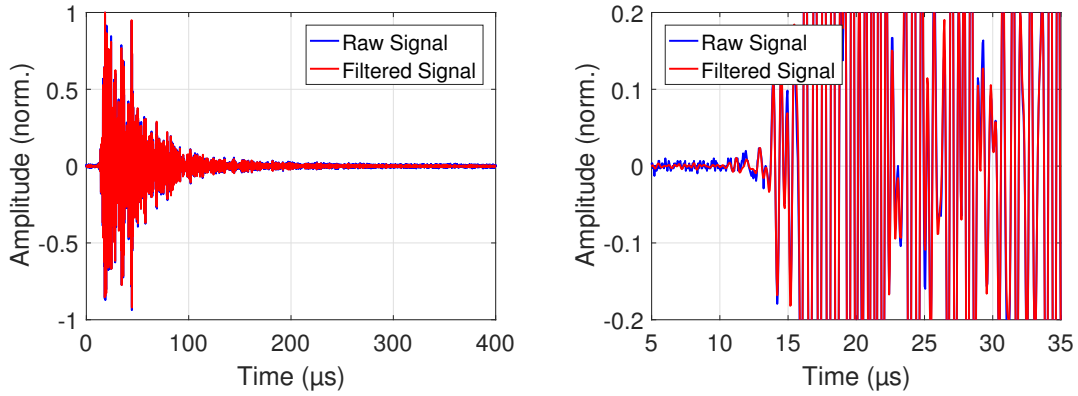
$$\begin{cases} \tau_a^{1.5\text{mm}} = (23 \pm 1)\,\mu\text{s} \\ D_{1.5\text{mm}} = (0.96 \pm 0.05)\,\text{mm}^2/\mu\text{s} \\ \ell^*_{1.5\text{mm}} = (1.9 \pm 0.1)\,\text{mm} \end{cases}, \tag{2.3}$$

where the transport mean free path is calculated through the diffusion coefficient, as expressed in equation (2.2).

The experimental data is well fitted by the diffusion theory. The value obtained for ℓ^*, under the assumption $v_T \simeq 1.5\text{mm}/\mu\text{s}$, is $\ell^* = 1.9\text{mm}$, which is in the same order of magnitude of the average mean bead size $d = 1.5\text{mm}$. It is necesary to precise that on our experiments, ℓ^* is not determined intependently, in contrast with what is measured in [1]. Nevertheless, even for the shortest distance between emitter and receiver $L = 15\text{mm}$, the diffusion approximation remains true. This is mainly due to the fact that the wave travels about 10 times the size of the beads, which is a distance enough to consider the propagation in the difussive regime [3]. On the other hand, the diffusion coefficient and absorption time are in the same order than those obtained by Page et al. [1]. Since both the bead diameter and the working frequency are in the same order, it is expected to obtain similar values for the transport parameters.

An analogous procedure is carried for the 5mm bead size. A 2-cycles sine wave with frequency 2.0MHz is emitted from the central channel of the array and the transmission is meassured by the single element transducer. Again, the experiment is repeated for $N = 8$ different configurations of disorder, for each distance $L = 25\text{mm}$, $L = 20\text{mm}$ and $L = 15\text{mm}$. The acquired signals are filtered with a band-pass between 1MHz and 3MHz

to eliminate any low-frequency coherent contribution and to reduce electronic noise. In figure 2.6(a) a particular transmission is presented, comparing both raw and band-passed signals, while in figure 2.6(b) a zoom around its arrival time is shown. Comparing this measurements to the those with smaller beads, the low-frequency coherent contribution seems to be neglectable in the 5mm bead size case.



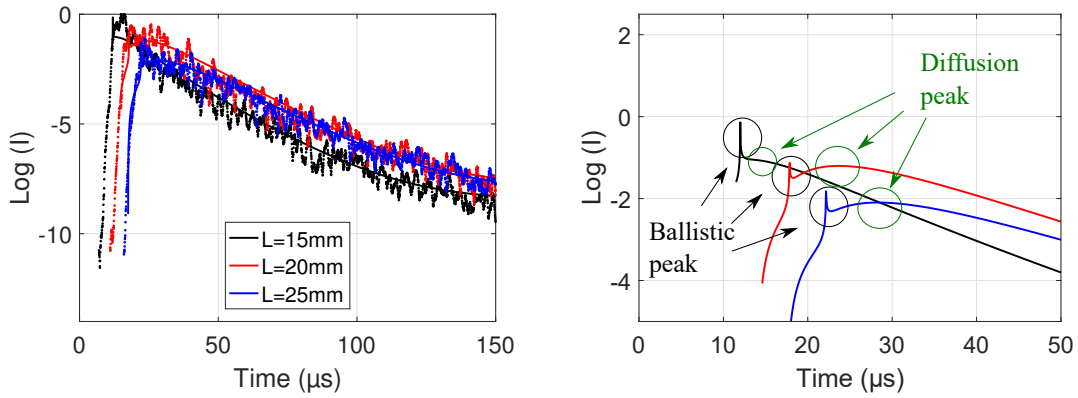
(a) (b)

Figure 2.6: Transmitted signal for beads of 5mm diameter and a distance between emitter and receiver of $L = 25$mm. (a) Comparison between raw and bandpass filtered signals. (b) Zoom around arrival time to evidence the difference between raw and filtered signals. Contrary to the case with smaller beads, for this bead size the coherent low-frequency contribution is negligible.

Proceeding as before, the average transmitted intensity is calculated for the different values of L. However, for this size of beads, the distance between emitter and receiver is about 3-5 times the scatterer's size. Thus, the diffusion approximation is not the right model to fit our experimental data. Instead, the *Radiative Transport Theory* is a more accurate model. The Radiative Transfer Equation (RTE) details how the average radiated intensity in a given direction depends on spatial and temporal variables. Although this equation does not fully describe wave propagation, it is accurate for the mean intensity transmission, as it happens to be in our experimental context. By writting the energy density in terms of the amount of scattering events, one may apply the Born approximation to keep the first-order scattered intensity. Then, it has been deduced analitically an approximated solution for RTE in a 3D infinite media. For a pulsed point-like source, the expression is given by [4, 5]

$$I(r,t) \propto \frac{e^{-t/\tau_a} e^{-ct/\ell_S}}{4\pi r^2} \delta\left(t - \frac{r}{c}\right) + \frac{\left(1 - r^2/c^2t^2\right)^{1/8}}{\left(4\pi \ell_S ct/3\right)^{3/2}} \times e^{-t/\tau_a} e^{-ct/\ell_S} G\left(\frac{ct}{\ell_S}\left[1 - \frac{r^2}{c^2t^2}\right]^{3/4}\right) H\left(t - \frac{r}{c}\right), \quad (2.4)$$

where H is the Heaviside function, and $G(x) \approx \exp(x)\,(1 + 2.026/x)^{1/2}$.



(a) (b)

Figure 2.7: (a) Time of flight distribution in logarithmic scale for different distances between emitter and receiver. In dots are shown the experimental data; in solid line the fit model from the solution to the RTE. The transport parameters obtained from the fitting are $\ell_S^{5\text{mm}} = (5.4 \pm 0.7)\,\text{mm}$ and $\tau_a^{5\text{mm}} = (21 \pm 1)\,\mu\text{s}$. (b) Zoom near the begining of the arrival time for the obtained fittings. The ballistic peaks are pointed out with black circles, while the diffusion peaks as green ones.

The time of flight distribution is fitted with equation (2.4) for the three values of L. The transmitted intensities obtained and their corresponding fits are presented in figure 2.7(a). For this case, the RTE fits properly the experimental curves. For the three fits the values obtained for the transport parameters are similar. From the fittings we obtain the parameters of the absorption time τ_a and the scattering mean free path ℓ_S; nevertheless, it is possible to estimate also the diffusion coefficient. As expressed by Zhou et al., there are two maximums in the theoretical solution given by (2.4): the ballistic and the diffusion peaks, as represented in the zoom presented in 2.7(b). In particular, the second peak can be related to the diffusion coefficient by the approximated relation [5, 6]

$$D \approx 0.1 \frac{L^2}{t_M}, \tag{2.5}$$

where t_M is the time of the diffusion peak. Then, the transport parameters obtained from the fits and the calculations are

$$\begin{cases} \tau_a^{5\text{mm}} = (21 \pm 1)\,\mu\text{s} \\ \ell_S^{5\text{mm}} = (5.4 \pm 0.7)\,\text{mm} \\ D_{5\text{mm}} = (1.5 \pm 0.3)\,\text{mm}^2/\mu\text{s} \end{cases} . \tag{2.6}$$

If we understand the scattering mean free path as the distance the wave has to travel between each scattering event, and since our system is composed of beads in contact, it is natural to expect a scattering mean free path which is comparable to the bead size.

Effectively, we obtained a value that is about the size of the beads (5mm), which make our results consistent.

Now, we can take a step further and relate the scattering mean free path with the transport mean free path using the relation given by (1.19). Considering spheres with radius $a = 2.5$mm and central frequency of 2.0MHz, we have that $\overline{\cos\phi} = 0.18$. From the value obtained from the scattering mean free path $\ell_S^{5\text{mm}} = (5.4 \pm 0.7)\,\text{mm}$, we calculated the transport mean free path, obtaining $\ell^*_{5\text{mm}} = (6.5 \pm 0.9)\,\text{mm}$. However, this calculation considers that the scattering pattern from each bead is essentially the same, i.e. under the independent scattering approximation. Such behaviour is not necessarily valid in our system, because we cannot expect the scattering to be identical for each bead since they are in contact. Nevertheless, as a first-order approximation, we can use it to estimate the value of the transport mean free path.

As it is mentioned in [5], the value for the diffusion coefficient is related to the diffusion peak in the average intensity profile. The results presented in figure 2.7 show that the tendency of both experimental data and the fits are in good agreement. Then, it allows us to consider that the diffusion coefficient is in the right order of magnitude.

Furthermore, with these values, it lead us to use the relation (1.18) to estimate a transport velocity, obtaining $v_T = 3D/\ell^* \sim 0.69\text{mm}/\mu\text{s}$. This value is about half the propagation velocity in water, which is against of what was estimated for the small beads measurements. In the next section, a further analysis in the transport velocity will be carry out by measuring independently the transport parameters D and ℓ^*.

On the other hand, the absorption time is the decay ratio for large times. In a logarithmic scale, it can be associated with the slope of the curve. Once again, we find a good agreement in the tendency between experimental data and fit, which implies that we are in the good order of magnitude for this parameter too.

Summary

We measure the transport parameters of a close-packing suspension made of glass beads immersed in water. In particular, for the chosen frequency, we distinguish two clearly different situations. On the one hand, a medium composed by beads which diameter (1.5mm) implies a propagation that is purely diffusive. In such a case, we used a 3D half-space model that suits our experimental conditions. On the other hand, a system composed of bigger beads (5mm) made the overall propagation regime a mixture of multiple scattering and diffusive. Then, the diffusion model does not fit correctly the experimental data. Instead, a solution of the RTE is used, obtainning a good agreement between the physical model and the experimental results. Thus, this model allows us to measure more accurately the transport parameters in such situation where diffusion is not yet isotropic.

For the small beads case, we measure the absorption time and the diffusion coefficient.

Then, assuming that the transport velocity is equal to that in water, we were able to calculate the transport mean free path through equation (2.2). We obtained a value of $\ell^* \simeq 1.9$mm, comparable to the bead size 1.5mm. In the next section, we will measure independently both transport mean free path and diffusion coefficient, to have a more accurate estimation on the transport velocity and to validate the approximation $v_T \sim c$.

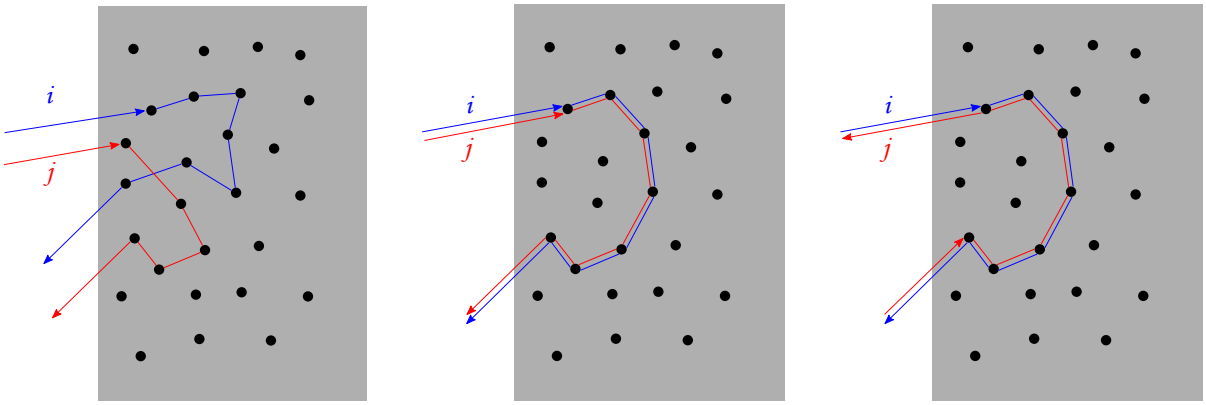
Finally, in the 5mm beads case, we utilized the solution of the RTE to measure the absorption time and the scattering mean free path. For the first one, we obtained a value comparable to that for the smaller beads, meaning that absorption is not due to viscous losses in fluid-solid interface [1]. For ℓ_S we obtained a value quite similar to the bead size. An estimation for the transport mean free path is also presented, however it is not completely accurate since it requires the independent scattering approximation. Such assumption is not strictly obey in our system, since the theory does not contemplate scatterers that are touching each other. Furthermore, since we are working in the range $2.5\ell_S < L < 5\ell_S$, we find two peaks in our averaged transmitted intensity, in agreement with [5]. As detailed in figure 2.7(b), we found both ballistic and diffusion peaks in our fittings. Then, it was possible to estimate the diffusion coefficient through the relation (2.5). Finally, using relation (1.18), we estimated a transport velocity v_T of about half the propagation velocity in water. This value will be further verified in the following section.

2.1.2 Coherent backscattering cone

In the previous section, we chose to describe wave intensity transport as a random walk, forgetting the phase carried by the multiple scattered waves. This description is not completely adequate since interference phenomena can survive disorder, as highlighted by the Coherent Backscattering Effect. The coherent backscattering cone occurs when an incident plane wave impinges on a multiple scattering medium and one observes the reflected intensity. This latter exhibits peaks and dips of intensity characteristic of a speckle pattern. However, after averaging over disorder, an enhanced intensity cone appears in the backscattering direction, an effect referred to as the "coherent backscattering effect". It can be explained as follows. The reflected intensity can be decomposed on pairs of scattering paths. Each pair can be put in one of three families by their contribution to the intensity, which can be expressed as the sum over the product of two scattering paths i and j

$$I = |A|^2 = \sum_{i,j} A_i A_j^*. \tag{2.7}$$

The first one, the "speckle family", is composed of pairs of paths that follow different scattering sequences so that their contributions average out to zero (figure 2.8(a)). The second one, the "incoherent family", is made of pairs of paths which follow the same



(a) Speckle family (b) Incoherent family (c) Coherent family

Figure 2.8: Schematic representation of the three families pairs in the backscattering intensity cone. (a) The speckle family corresponds to those which travel through different paths and, hence, their contribution to the average intensity is nule. (b) The incoherent family contribute to the intensity as an isotropic distribution; the paths taveled are exactly the same. (c) The coherent family corresponds to identical paths but traveled in oposite direction.

sequences of scattering in the same order (figure 2.8(b)). On average they lead to an isotropic distribution of intensity. These paths are the only ones that are retained in the so-called Boltzmann approximation. In the third family, the two paths travel through the same scatterers but in opposite directions (figure 2.8(c)). Under the reciprocity assumption, the two corresponding waves constructively interfere in the incident direction, having accumulated the same phase along the two paths. On average we thus have twice as much intensity in the incident direction as in the other directions. Another way of saying this is that the probability of returning to the source is twice as great for a multiple scattered wave than for a random walker (without memory). A macroscopic consequence of this effect is a decrease of the diffusion coefficient, precursor of Anderson ("strong") localization, hence the other name "weak" localization of the coherent backscattering effect.

The coherent backscattering cone has been observed for different types of waves. The first experimental demonstration was reported in optics in the 80's [7, 8]. Then experiments performed with acoustic and elastic waves showed the same effect in the 90's [9–11].

Interestingly, while the CBE is the manifestation that the diffusion equation fails in describing all aspects of wave propagation in multiple scattering media, it also offers a means of measuring both the diffusion coefficient and the transport mean free path [6, 10]. This method manifests through the cone's width, which dependence relies on the characteristic transport distance.

We can intuitively see the dependence of the coherent backscattering cone width on the characteristic parameters of the multiple scattering medium. The directivity pattern present in the backscattered intensity is characterized by the three families mentioned above. In the $-k_0$ direction, a two-to-one amplitude ratio with the background is present, where the coherent and incoherent families contribute by the same factor. However,

when we deviate from the backscattering direction, this amplitude ratio decays due to the difference in acoustic paths. This phase shift is given by a relation of proportionality with the transverse distance $|\mathbf{r} - \mathbf{r}'|$ between the entry and exit points of the wave in the system. In the stationary case, the characteristic distance of the medium is the transport mean free path ℓ^*. For the case where the distance $|\mathbf{r} - \mathbf{r}'|$ is greater than ℓ^*, the incoherent contribution becomes dominant. Therefore, coherence contributes to intensity only when $|\mathbf{r} - \mathbf{r}'| \leq \ell^*$. The path difference between two acoustic rays that are backscattered an angle θ from the direction $-k_0$ is approximately $\theta\ell^*$. Likewise, it is expected that the interference is constructive when $\theta\ell^* \leq \lambda$. Thus, we can say that the characteristic angular width of the coherent backscattered intensity is $\Delta\theta \simeq \lambda/\ell^*$. When the distance a between planes is sufficiently large, i.e. in the far-field, we have that the spatial half-width of the cone is given by

$$\delta_{\mathrm{S}} \propto \frac{\lambda a}{\ell^*}. \tag{2.8}$$

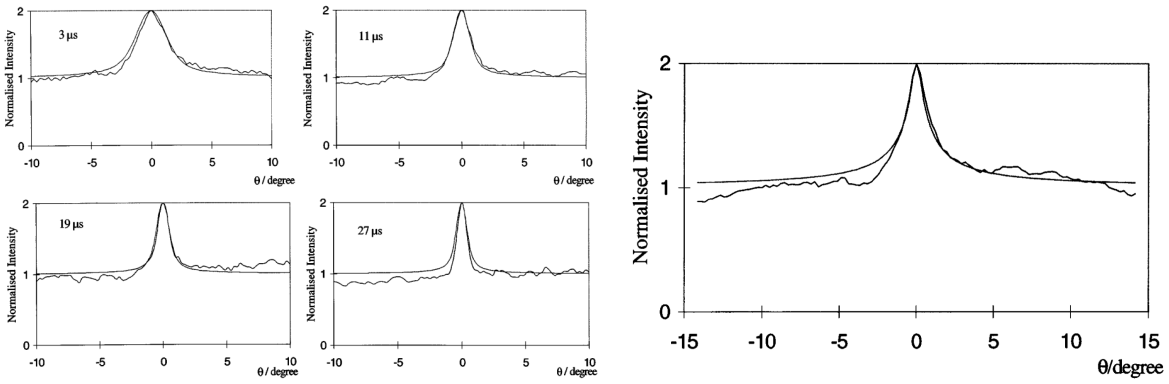
Similarly, in the dynamic case, we have that the characteristic distance of the system is given by the width of the diffusive halo as a function of time $\sqrt{Dt}$. Therefore, the spatial width of the dynamic backscattering cone is

$$\delta_{\mathrm{D}} \propto \frac{\lambda a}{\sqrt{Dt}}. \tag{2.9}$$

Tourin et al. proved, in a 2D multiple scattering system, the dependence between the backscattering cone and the transport parameters [10]. They determined an expression for both the dynamic and stationary cone's width in terms of the transpor parameters, relations that were verified experimentally. In the dynamic case, figure 2.9(a), the cone's width gets narrower when the time grows, which dependence on the diffusion coefficient D is similar to the expression (2.9). In the stationary case, the cone's width is sensitive to the transport mean free path ℓ^*, as presented in equation (2.8). The experimental results for the stationary case is shown in figure 2.9(b).

A clear advantage exposed by the authors, relies on that the coherent backscattering effect allows to measure independently both transport parameters D and ℓ^*. This means that, with both dynamic and stationary cones, one may determine also the transport velocity v_T which links the parameters measured. They showed this and presented the corresponding calculations. The multiple scattering medium utilized by them was a system composed of parallel steel rods of diameter 0.8mm, with mean distance 2.4mm between them and an average density of $n = 0.1857\mathrm{mm}^{-2}$. Working at a central frequency of 3.2MHz, they obtained the corresponding values $D = 3.2\mathrm{mm}^2/\mu\mathrm{s}$ and $\ell^* = 4.8\mathrm{mm}$. With such values, the transport velocity calculated was $v_T = 2D/\ell^* = 1.3\mathrm{mm}/\mu\mathrm{s}$, which is slightly lower than the propagation velocity in water.

A more recent work, carried out by Cobus et al., presents the dynamic coherent



(a) (b)

Figure 2.9: Coherent backscattering cone in a 2D multiple scattering system. (a) The dynamic backscattered cone gets narrower as time grows (figures for 3μs, 11μs, 19μs and 27μs), where its width is sensitive to the diffusion coefficient, D. (b) On the other hand, the stationary cone is obtained after time-integrating the backscattered acoustic intensity, where the cone's widht is sensitive to the transport mean free path, ℓ^*. Figures extracted from [10].

backscattering in a 3D graunlar media immersed in water [12]. In their work, the authors use a slab-shaped mesoglass granular media composed of aluminum beads, brazed together to form a disordered elastic network. The beads mean diameter was 3.93mm, with a polydispersity of 20%, and a bead volume fraction of 55%. The sample has a cross-section of $230 \times 250\text{mm}^2$ and thickness $L = 25$mm. In their experiment, the sample is waterproofed by covering it with an acoustically transparent plastic film, so that the ultrasonic waves propagate only through the elastic network. The working frequency was 1.6MHz, wich implies a wavelength in water of about 0.94mm. The medium is excited using one single channel of a N-elements array made of piezoelectric transducers. The backscattered acoustic wavefield is measured with the N channels, for a total of 302 different configurations by translating the array paralel to the medium surface. In figure 2.10 the experimental results obtained for different times, with the corresponding theoretical model fit, are presented.

In paralel to the experimental results in a 3D granular medium, Cobus et al. presented a physical model adapted to the coherent backscattering of acoustic waves in a 3D medium. Under these conditions, the authors present the behaviour expected of the coherent backscattered cone's width and its dependence with the diffusion coefficient. For a slab-like system of thickness L, the cone's half-width at half-maximum is given by the expression

$$k_0 \delta_{\mathrm{D}} = \Gamma_{\mathrm{D}} \left(\frac{a}{\sqrt{Dt}} \right), \tag{2.10}$$

where k_0 is the wavenumber in water, a the distance between the array and the surface of the medium, D the diffusion coefficient and Γ_{D} a dimensionless constant which value is near unity, as it happens in 2D media [10]. This expression holds under the assumption

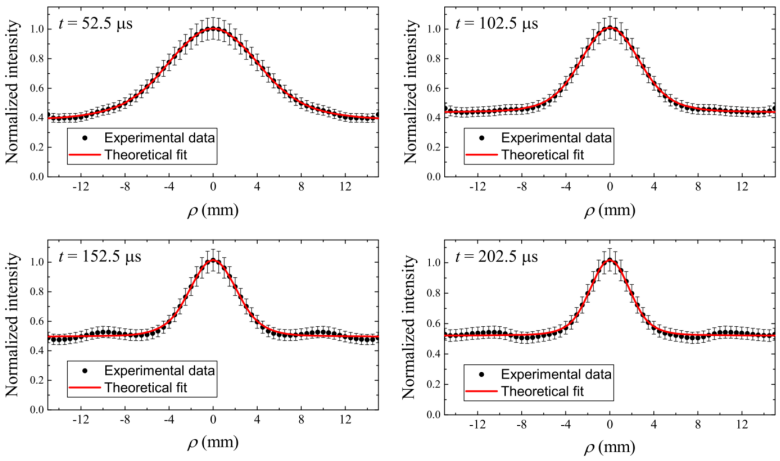


Figure 2.10: Dynamic coherent backscattering cone for a 3D granular medium immersed in water. The dynamic backscattered cone is presented for 52.5μs, 102.5μs, 152.5μs and 202.5μs, comparing respectively the experimental results with the corresponding fit from the physical model. Figure extracted from [12].

of small scattering mean free path, i.e. $a \gg \ell_S$, and for distances in the diffusive far-field, which is satisfied if $a^2 \gg 4Dt$. Then, the backscattered cone is expected to be nearly a Gaussian shaped cone, giving rise to expression (2.10). Furthermore, by integrating in time the intensity profile of the dynamic case, the authors express that, also in a 3D medium, it is expected to find a relation for the cone's width in the stationary case that depends on the inverse of the transport mean free path ℓ^* [12]

$$k_0\delta_S = \Gamma_S\left(\frac{a}{\ell^*}\right). \tag{2.11}$$

For simplification, we are going to assume that the dimensionless constant Γ_S is also near unity.

We then conclude that, comparing the expressions for 2D and 3D, equations for the cone's half-width at half-maximum are quite similar. In the dynamic case, it is expected to have a dependence in the cone's width proportional to $(Dt)^{-1/2}$; meanwhile, in the stationary case, we can expect a dependence inversely proportional to ℓ^*.

Experimental setup

The experimental measurement of the coherent backscattering cone was carried out for the two bead sizes mentioned before: monodisperse beads of 1.5mm and 5mm respectively. The array of piezoelectric elements was placed at a fixed distance $a = 90$mm, which acts as both emitter and receiver. One channel of the array emits an initial excitation composed of 15-cycle sinus of central frequency 2.0MHz. The echo is recorded by 32 channels, with the emitting source in the center of them. To improve the amount of configurations needed, the emission/reception process was repeated for each of the 32 channels between

positions 16 and 48. The backscattered intensity was finally averaged for the 32 different emissions over 10 different configuration of disorder. For both bead sizes, the volume of beads used was kept fixed by filling the tank to a height of approximately 70mm. A schematic representation of the experimental setup is presented in figure 2.11.

Figure 2.12(a) shows a characteristic measured wave, while figures 2.12(b) and 2.12(c) present the average intensity in logarithmic scale and the average normalized intensity (according to the emitting channel), respectively. Comparing the figures we see how the coherent backscattered cone arises after normalizing the average received intensity. In this case the measurements correspond to 1.5mm diameter beads.

On the other hand, figure 2.13 shows the respective same results for the 5mm beads case.

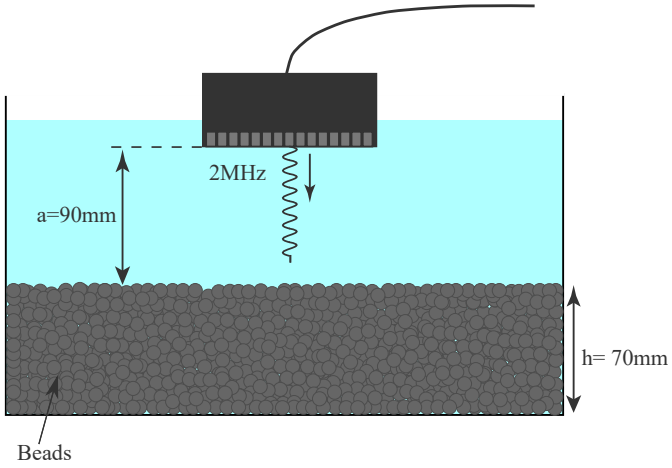


Figure 2.11: Schematic representation of the experimental setup for measuring the coherent backscattering cone. The array of piezoelectric elements is placed at a distance of 90mm above the surface of the multiple scattering medium, where a 15-cycle sine wave is emitted with a single channel at a frequency of 2.0MHz. The bottom of the tank is filled with beads up to a height of 70mm.

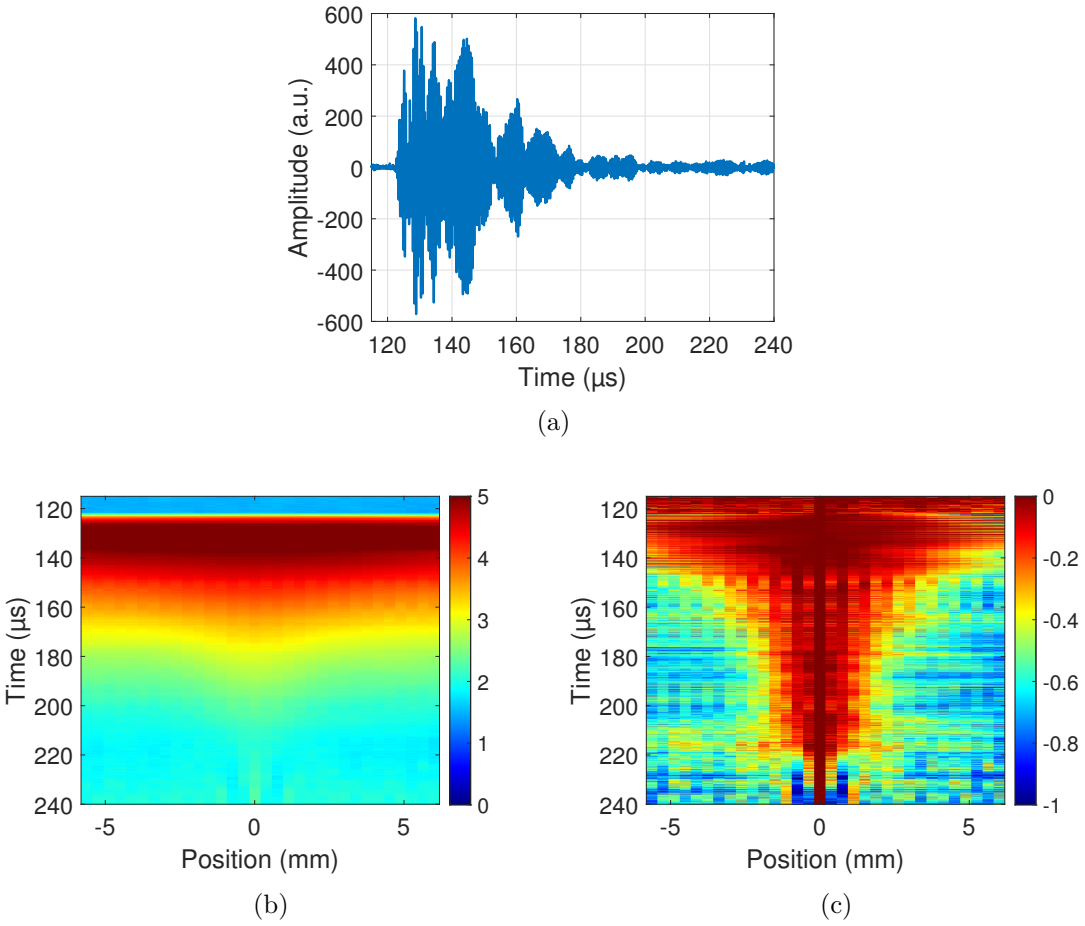
Dynamic cone

For the dynamic cone we consider time windows of 5μs duration, where we average the received intensity for each channel. We obtain the spatial profile of the cone as a function of the time of the respective window.

The half-width at half-maximum was calculated for each time window. The measured values were fitted by a curve of the form

$$\delta_{\mathrm{D}}(t) = \frac{A}{\sqrt{t - B}}, \tag{2.12}$$

where A contains information about the parameters of the experiment and the diffusion coefficient D (according to the equation (2.10)) and B represents the time delay at which the diffusive process starts.



(a)

(b)

(c)

Figure 2.12: Experimental results for 1.5mm diameter beads. (a) Signal received by a single element of the transducer array. (b) Average intensity in time and space, in logarithmic scale. (c) Average intensity normalized by the transmitter channel, also in logarithmic scale. One can see how the appearance of the coherent backscattering cone is manifested when normalization is performed.

The fit obtained for the system composed by the 1.5mm diameter beads is

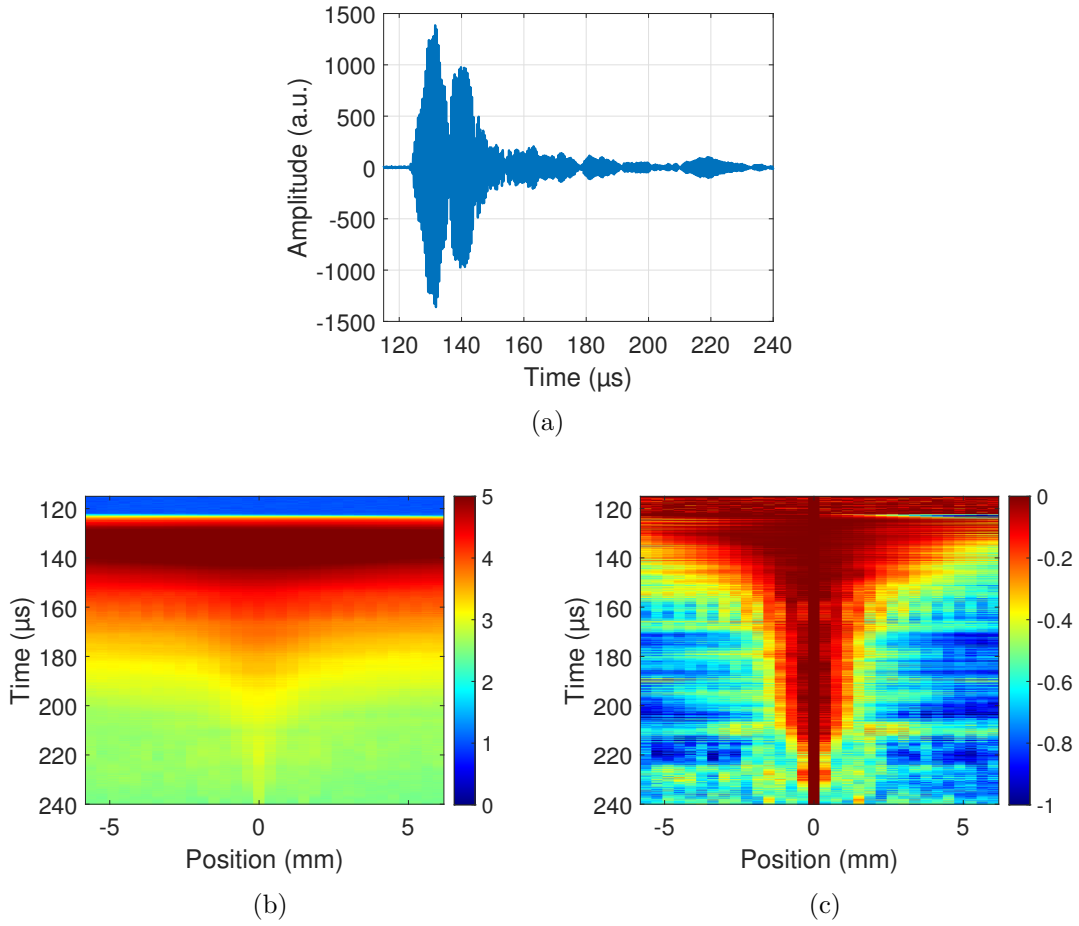
$$\delta_{\mathrm{D}}(t) \simeq \frac{12.6\mathrm{mm} \cdot \mu\mathrm{s}^{\frac{1}{2}}}{\sqrt{t - 137\mu\mathrm{s}}}, \tag{2.13}$$

which implies a value for the diffusion coefficient

$$D_{1.5\mathrm{mm}} = (0.72 \pm 0.03)\,\mathrm{mm}^2/\mu\mathrm{s}. \tag{2.14}$$

Here the errorbar comes from the fit.

First, we can see that the obtained time delay with the fit corresponds to 137μs, which is no other than the time when diffusion begins. The value obtained makes sense, since it is near the arrival time of the echo measured by the array. Nevertheless, we can do an estimation of this value. The excitation signal consist on a $15-$cycles sinusoid, with central frequency 2.0MHz, which means a duration of 7.5μs. Then, if we consider



(a)

(b)

(c)

Figure 2.13: Experimental results for 5 mm diameter beads. (a) Signal received in a single channel. (b) Average intensity in logarithmic scale. (c) Average intensity normalized by the transmitter channel, also in logarithmic scale.

the reflection of such signal with the surface of granular medium, which is (of course) coherent, we have 7.5μs. Also, considering the propagation distance between emitter and receiver, we have $2a = 180$mm that the wave travels through water, meaning that we have 120μs of propagation in water. These values give us a total of 135μs, which is quite close to the time obtained with the fit.

Secondly, we can compare the value for D with that obtained by the time of flight distribution (measured by transmission in the previous section 2.1.1). We can see that the diffusion coefficient is slightly lower. The methods utilized imply a 25% difference in the measurement of D. However, even if both methods return values in the same order, we can be more confident in the measurements by the dynamic coherent backscattering due to the amount of averaging considered. While in the time-of-flight distribution measurements we averaged over eight different configurations, in the coherent backscattering we worked over more than ten times this amount.

Analogously, for the 5mm diameter beads case we find that

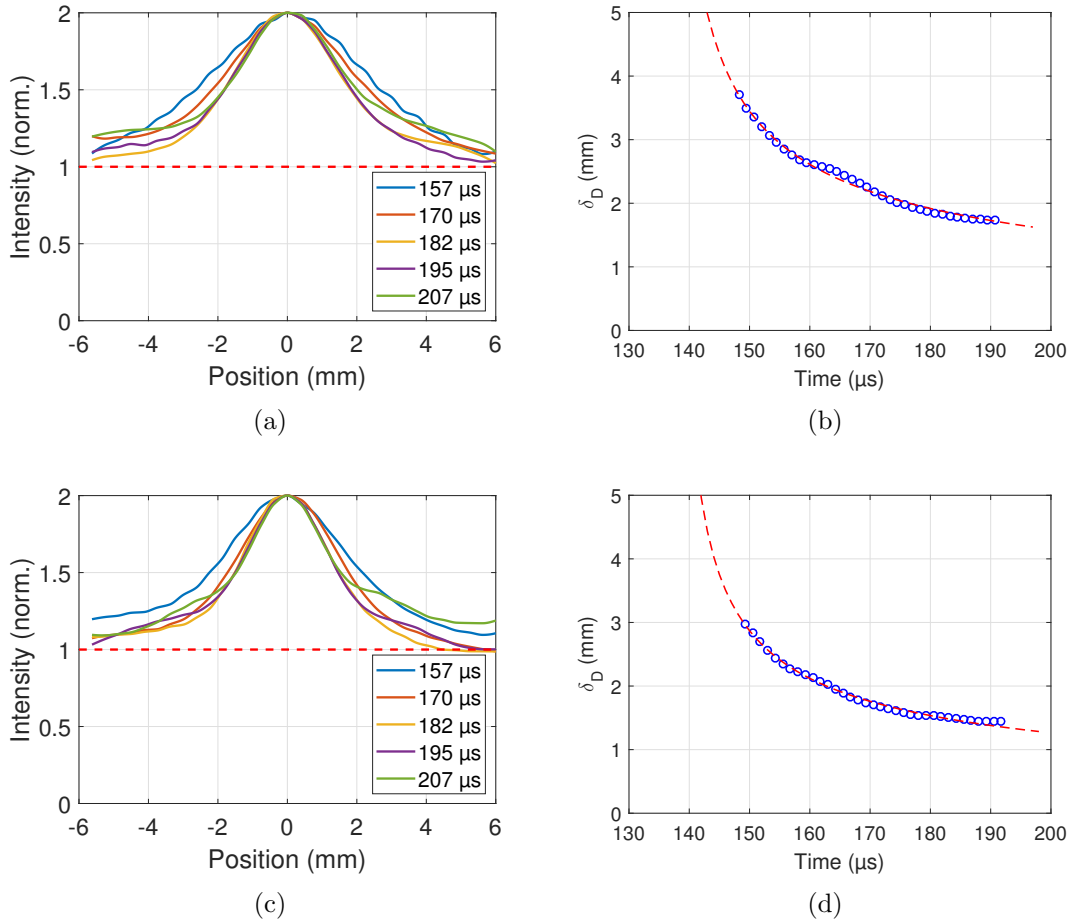


Figure 2.14: Experimental results for the dynamic cone. (a) and (b) correspond to 1.5mm beads and (c) and (d) correspond to the 5mm bead case. (a) and (c) Dependence of the backscattering cone for different times where the intensity is averaged over windows of 5μs duration. (b) and (d) show the half-width at half-maximum as a function of time, with its corresponding fit.

$$\delta_{\mathrm{D}}(t) \simeq \frac{9.96\mathrm{mm}\cdot\mu\mathrm{s}^{\frac{1}{2}}}{\sqrt{t-138\mu\mathrm{s}}}, \tag{2.15}$$

where we infer a diffusion coefficient of

$$D_{5\mathrm{mm}} = (1.16 \pm 0.04)\,\mathrm{mm}^2/\mu\mathrm{s}. \tag{2.16}$$

Again, we find a delay in time that is in good agreement with our experimental conditions, under the same reasoning as before.

The diffusion coefficient give us, also for this bead size, a value that differs about 30% from what we obtained with the time-of-flight distribution. However, the value in the previous section was only a rough estimation, since we use the RTE model to fit our data. At the end of this section we will go deeper in the comparison between parameters.

Stationary cone

For the stationary cone, we consider the mean intensity averaged over the measured time excluding the first arrival. In our experiment we consider a time window of 100μs, comprised between 140μs and 240μs. In the figure 2.15 we see the profile of the stationary backscattered cone for each of the bead sizes considered.

From the results obtained experimentally (presented in figure 2.15) we can estimate the value of the transport mean free path ℓ^* by using the expression (2.11) for δ_S. Thus, we have for 1.5mm diameter beads

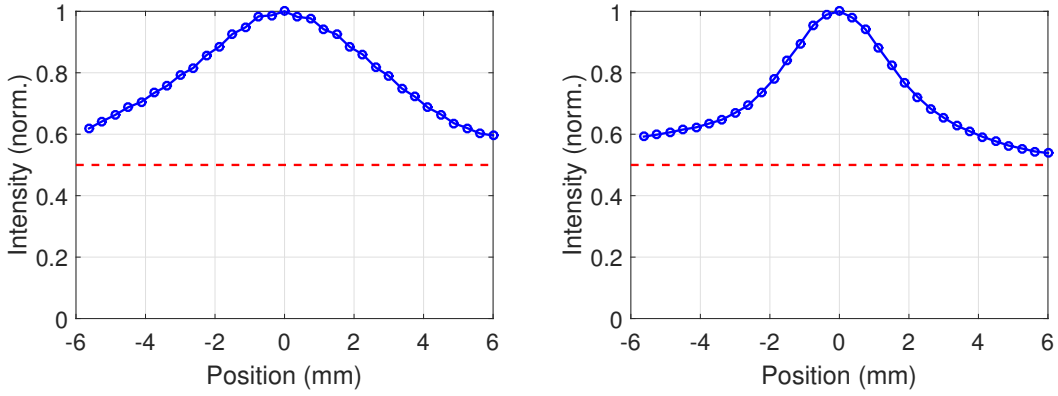


Figure 2.15: Experimental results for the stationary backscattering cone. (a) Stationary cone for 1.5mm beads. (b) 5mm beads.

$$\ell^*_{1.5\text{mm}} = (3.15 \pm 0.16)\,\text{mm}. \tag{2.17}$$

Here the errorbar is calculated from the standard deviation of the intensity.

We see that the transport mean free path (for this bead size) is approximately twice the size of the beads and approximately 1.5 times the value measured by the TOF distribution. Such difference arise from the assumption made for the diffusion approximation in the averaged transmitted intensity: the transport velocity is equal to the wave propagation velocity in water. If we combine the transport parameters measured by both dynamic and stationary coherent backscattering cone, we may calculate the transport velocity in the multiple scattering medium. By using equation (1.18), for our 3D medium, we obtain a velocity $v_T = 3D/\ell^* \simeq 0.68\text{mm}/\mu\text{s}$. This velocity is about half of the propagation velocity in water, which means that the medium is strongly diffusive for the frequency utilized. Moreover, the transport velocity is found to be in the strong diffusion range and not in the localization regime, where the velocity of the energy tends to increase above the one of ultrasound propagating in water [12, 13].

Such low values for the transport velocity have already been found in similar experiments. In particular, in the work of Schriemer et al., the authors find reasonant peaks

and dips of the transport velocity, in terms of the product of the wavenumber in water k_0 with the beads radius a [14]. Based on a spectral function approach, the physical model fits the experimental data obtained by the authors with a good agreement between the curves. In particular, close to the value $k_0 a \simeq 6.5$, it appears a dip in the transport velocity which reaches values close to 0.75mm/μs. In our experiment, for a normalized frequency of $k_0 a \simeq 6.3$ we obtained a transport velocity of $v_T = 0.68$mm/μs, which is in concordance with what is presented by the authors in their work.

Then, having determined the transport velocity, now we can do a more accurate evaluation of the diffusion time obtained in (2.13). The arrival time seen in the acquired signals is approximately 124μs. Then, if we add the reflection in the medium's surface (as mentioned before), we have to add 7.5μs. Finally, considering the time for diffusion to start as ℓ^*/v_T, we have another term of 4.6μs. Thus, we have a total time of 136μs, quite close to the value given by the fit 137μs.

Meanwhile, for 5mm beads we obtain

$$\ell^*_{5\text{mm}} = (5.22 \pm 0.23)\,\text{mm}. \tag{2.18}$$

For this bead size, the value obtained for the transport mean free path is in good agreement with what we found for the time-of-flight distribution using the RTE solution model. If we proceed as before, we can estimate the transport velocity in the medium. Using equation (1.18), we have that $v_T = 3D/\ell^* \simeq 0.67$mm/$\mu$s. Once again, we have a similar diffusive regime for our frequency range and bead size considered. In this case, the comparison with [14] is no longer possible, since for this bead size gives $k_0 a \simeq 21$, which is larger than the range measured by the authors in their work. Nevertheless, we can compare the transport velocity measured by CBE with that determined by the fit using the solution to the RTE, we see that both methods give us very similar values. However, the porcentual differences in the transport parameters are about the 20%, thus we can assure this measurement within such range.

Furthermore, we can evaluate the diffusion time of the fit presented in (2.15). Reasoning as before, we obtain a value for the delay that is roughly 139μs, again quite similar to the value determined with the fit 138μs.

Summary

In this section we presented an experimental study of the coherent backscattering cone, both dynamic and stationary, to determine the transport parameters of our multiple scattering medium.

On the one hand, we measured the diffusion coefficient for the two bead sizes considered. Comparing with the values obtained in the previous section by the study of the TOF distribution, the results are in the same order of magnitude. The difference

between the diffusion constant D inferred from these two methods (TOF and CBE) is about $20\% - 30\%$.

On the other hand, we have measured the transport mean free path using the two methods. The values obtained are in good agreement for $d = 5$mm. For the 1.5mm beads the case is more particular. By analyzing the TOF distribution the value obtained is about the bead size, $\ell^* = 1.9$mm. Meanwhile, in the CBE experiment, the obtained value is $\ell^* = 3.15$mm, which is about twice the size of the beads. This difference arises in the fact that, for the TOF analysis, we assume that the transport velocity is equal to the propagation velocity in water, which not seems to be a reliable approximation.

Thus, by independently measuring D and ℓ^* using the CBE, we found that the energy velocity turns out to be about half the value of acoustic wave propagation in water. Such result is reminiscent of what was obtained in previous works [14, 15], where the resonances scattering is resposible for the decrease of the energy transport velocity.

2.2 Time-reversal as a means to measure transport parameters

2.2.1 Fundamentals of time-reversal

Time-reversal is a topic with several years of study in many areas of physics related to wave propagation [16–19]. The basic principle behind it is to exploit the time-reversal invariance of the wave equation. For this invariance to hold, the medium might satisfy three simple hypothesis: linearity, determinism and time-invariance. Time-reversal is robust enough to hold, even if one of these suppositions is not strictly valid [20].

A simple description of the time-reversal process can be described into two steps. The first step, also known as "forward step", consists on the excitation of the medium with a function $s(t)$ from a point-like source located at position $\mathbf{r_A}$. The wave propagates through the medium and is recorded by a receiver, known as *Time-Reversal Mirror* (TRM), located at a position $\mathbf{r_B}$. The wave recorded this way can be writen as

$$p(\mathbf{r_B}, t) = G(\mathbf{r_B}, \mathbf{r_A}, t) * s(t) \tag{2.19}$$

where the function $G(\mathbf{r_B}, \mathbf{r_A}, t)$ is the impulse response of the medium between positions $\mathbf{r_A}$ and $\mathbf{r_B}$, and $*$ is the time-domain convolution product.

In the second step, the "backward step", the TRM emits the previously recorded signal but flipped in time. This way, the wave measured at a position $\mathbf{r}$ is

$$p_{TR}(\mathbf{r}, t) = G(\mathbf{r}, \mathbf{r_B}, t) * p(\mathbf{r_B}, -t). \tag{2.20}$$

Substituting the expression for p, we have that

$$p_{TR}(\mathbf{r},t) = G(\mathbf{r},\mathbf{r_B},t) * [G(\mathbf{r_B},\mathbf{r_A},-t) * s(-t)]\,. \tag{2.21}$$

Assuming reciprocity in the medium, we have that $G(\mathbf{r_A},\mathbf{r_B},t) = G(\mathbf{r_B},\mathbf{r_A},t)$. Thus, rearranging terms

$$p_{TR}(\mathbf{r},t) = [G(\mathbf{r},\mathbf{r_B},t) * G(\mathbf{r_A},\mathbf{r_B},-t)] * s(-t)\,. \tag{2.22}$$

We may write the quantity in straight brackets as $G(\mathbf{r},\mathbf{r_B},t) * G(\mathbf{r_A},\mathbf{r_B},-t) = G(\mathbf{r},\mathbf{r_B},t) \star G^*(\mathbf{r_A},\mathbf{r_B},t)$, where $\star$ denotes the cross-correlation product. Finally, exploiting ergodicity, equation (2.22) can be written as the configurational average of the Green's functions product

$$p_{TR}(\mathbf{r},t) = \langle G(\mathbf{r},\mathbf{r_B},t)\, G^*(\mathbf{r_A},\mathbf{r_B},t)\rangle * s(-t)\,. \tag{2.23}$$

Thus we obtain that the time-reversal spatial focusing, at the recompression time $t = 0$, is a statistical estimator of the correlation length [21].

When a medium presents randomly distributed local variations of impedance, wave propagation becomes complex. However, as long as the hypothesis are holded, the system maintains its time-reversal invariance despite inhomogeneities. It is possible to perform time-reversal even if a multiple scattering medium is present in the propagation region [16, 17].

At the early 90's, Fink, Cassereau and Wu introduced the concept of a "time-reversal cavity" [22]. A point-like source creates a spherical pulse that propagates through the medium, which can contain inhomogeneities. The initial pulse is distorted during its propagation and then is recorded by a closed surface of receivers that surrounds the source. In a second step, the surface of receivers emit the recorded signals but flipped in time. The wave propagates back to the initial source, like watching it as a video backwards. A schematic representation is presented in figure 2.16.

The application of a time-reversal cavity is impossible in a real experiment. In this direction, the concept of TRM is introduced. The idea consists in locating several transducers in a limited surface. Of course, the part of the wave that propagates (or is scattered) in directions outside the TRM aperture will be lost. This loss of information leads to a degradation of the focal spot. Nevertheless, this effect can be compensated when the propagation medium is complex as it is reminded in the next paragraph.

Time-reversal through multiple scattering media

Time-reversal of acoustic waves through multiple scattering systems is a topic studied for many years. One of its first experiments was performed by Derode, Roux and Fink [17]. The authors present a time-reversal experiment through a multiple scattering system

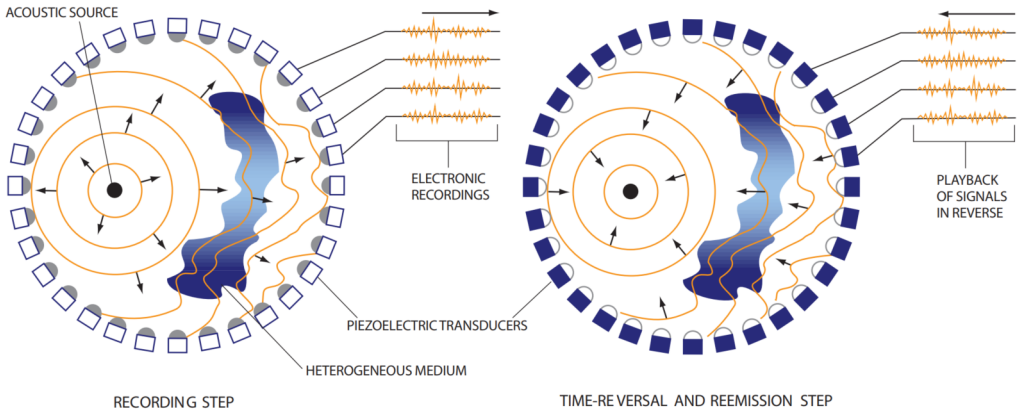


Figure 2.16: Scheme of the time-reversal cavity. In a first step, a point-like source emits a brief pulse that propagates through the cavity (left scheme). The transmitted wave-field is recorded by a closed surface made of transducers that surrounds the source location (then the name "time-reversal cavity"). In a second step, the transducers emit the recorded signals flipped in time (right scheme). The re-emitted signals propagate through the cavity, focusing back to the source location. Figure extracted from [23].

made of paralel steel rods, using a finite size TRM conformed by several piezoelectric transducers (a linear array of 96 elements). In the forward step, the source S emits a brief pulse that propagates through the medium and is recorded by the TRM (figure 2.17(a)). In the backward step, the TRM emits the time-reversed signals and the source S records the acoustic wavefield in the transversal direction x (figure 2.17(b)).

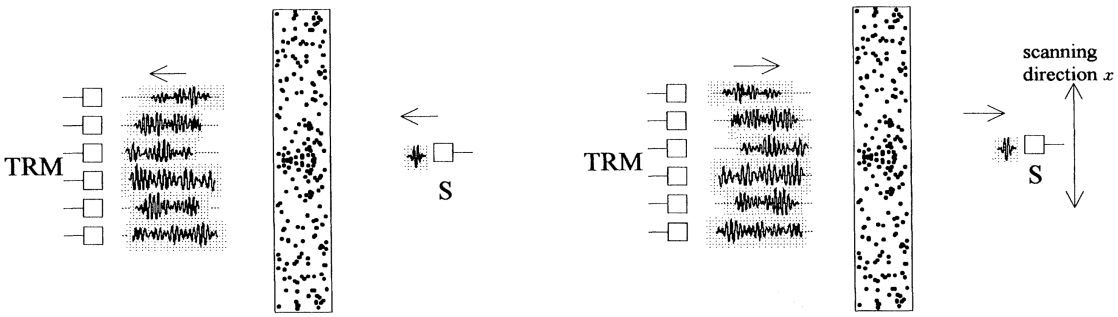
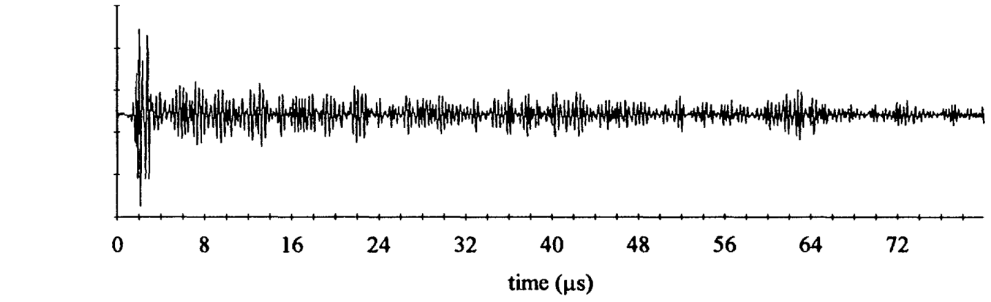
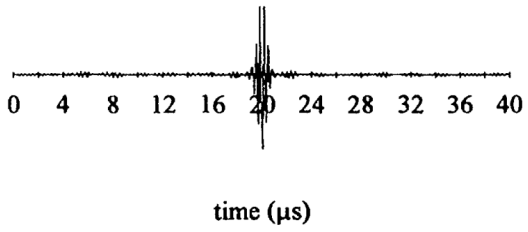


Figure 2.17: Acoustic time-reversal experiment through a multiple scattering system composed by paralel cylinders immersed in water. (a) Forward step of time-reversal. A source S emits a brief impulse that propagates through the slab-like medium. At the other side, a TRM records the transmitted wave in several positions. (b) Backward step, the TRM emits the recorded signals flipped in time and send them back to the medium. The source S now works as a receiver, recording the time-reversed acoustic field along the x-direction. Figures extracted from [17].

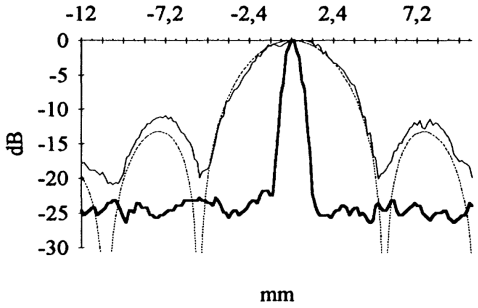
Figure 2.18(a) shows the time signal acquired by a single channel of the TRM. Due to the multiple scattering medium, the recorded signal's duration is much larger than the emitted one, spreading over time its energy. Contrary to what one would expect, the



(a)



(b)



(c)

Figure 2.18: Time-reversal focusing and recompression measurements. (a) Received signal by one channel of the TRM during step one. (b) Recompression measured at S after the time-reversed signals traveled back their paths to the source, with duration about 1μs (same as the initial excitation). (c) Time-reversal spatial focusing in the transversal direction x. The focusing obtained in water is compared to the difraction model (thin line and dashed line, respectivly); the thick line corresponds to the time-reversal through the multiple scattering medium, which is much narrower than the difraction limit thanks to the presence of the multiple scattering system. Figures extracted from [17].

received waveform at S after time-reversal presents a peak of significant amplitude and of very short duration (about 1μs, figure 2.18(b)), proof that all the signals emitted by the TRM elements arrive in phase at the source position at this instant. It is important to remark that the wave is able to travel back its path even in the presence of a strongly scattering medium. This is impossible for the case of particles, where it is needed to know the position and velocity of them with infinite accuracy [17].

By moving the source in the x direction it is possible to measure the spatial focusing of the time-reversal through the multiple scattering system. Compared to the difraction limit, the focusing obtained with the medium in between S and the TRM gets narrower (see figure 2.18(c)). The effect of multiple scattering, rather than worsening spatial focusing improves it significantly, operating as an acoustic lens. The presence of the multiple scattering medium allows the TRM to detect wavevectors that, in an homogeneous medium, would be out of its apperture and impossible to register. Thus, the medium works as a virtual enhancement of the apperture of the TRM, which allows it to capture information that otherwise would be lost.

2.2.2 Link between time-reversal and transport parameters

In the section 2.1.1 we have shown how the transport parameters can be measured through the average transmitted intensity [1] or by using the coherent backscattering cone [6, 24]. Previous studies have evidenced that there is a close relation between CBE and TR [25], even though the latter has never been used as a method for measuring transport parameters. In this section we expose the time-reversal focusing dependence with the transport parameters, exploiting its similarities with the coherent backscattering cone.

Let us consider a half-space multiple scattering medium immersed in water; a source S is located at a distance a from its surface and, inside the medium, a TRM is located at depth z_T. A schematic representation of the situation is shown in figure 2.19. Under these circumstances, time-reversal focusing becomes sensitive to transport parameters. During step one, a Dirac's pulse is emitted by S and propagates towards the multiple scattering medium where, after several scattering events, the wave is acquired by the TRM. In step two, the TRM emits the time-reversed signal, which is recorded in the source's plane at D, obtaining a wavefield given by equation (2.23)

$$p_{TR}\left(\mathbf{r_D}, t\right) = \left\langle G\left(\mathbf{r_D}, \mathbf{r_{TRM}}, t\right) G^*\left(\mathbf{r_S}, \mathbf{r_{TRM}}, t\right)\right\rangle. \tag{2.24}$$

This expression can be interpreted, as presented in the previous section, as if a source is located inside the multiple scattering medium and two detectors are placed outside the medium at S and D.

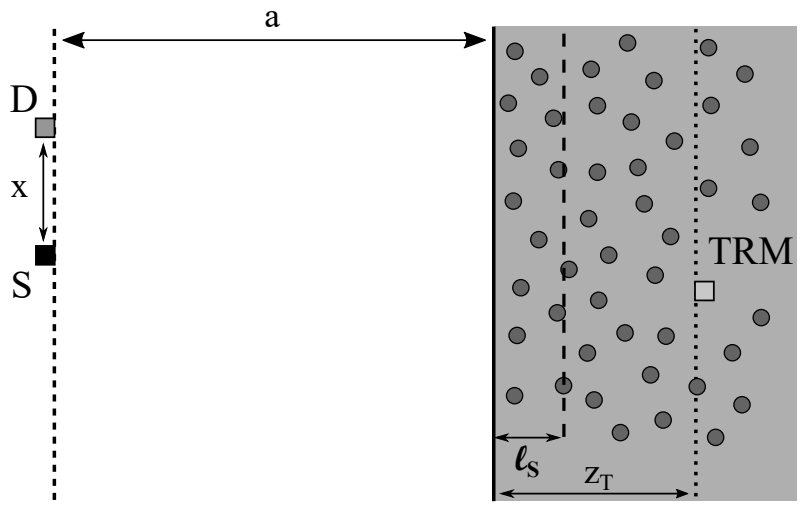


Figure 2.19: Schematic representation of the setup in which time-reversal focusing is expected to be sensitive to the transport parameters of the multiple scattering medium. Figure modified from [26].

The van Cittert-Zernike theorem states that, for an incoherent source of size L, the correlation length of the wavefield measured in a plane at a distance a is given by [27–29]

$$l \propto \frac{\lambda a}{L}. \tag{2.25}$$

Then, in our physical context we have that, for values of z_T larger than ℓ_S, the size of the diffusive halo at the system's surface is approximately z_T. Thus, through relation (2.25), we may expect a focusing width which is inversely proportional to the halo size z_T. Then, we may write

$$\delta_{\mathrm{S}} \propto \frac{\lambda a}{z_T}. \tag{2.26}$$

In the dynamic case, time-reversal is carried out by selecting time windows from the acquired signal. In such a situation, the size of the diffusive halo at the surface of the medium is proportional to the diffusion length $\sqrt{Dt}$. Then, we may expect that the focus width evolves with time as

$$\delta_{\mathrm{D}} \propto \frac{\lambda a}{\sqrt{Dt}}. \tag{2.27}$$

2.2.3 Physical model

So far we explained the expeceted dependence for this particular picture. With the main idea of how the time-reversal focusing depends on the parameters presented, we will carry out now a futher more formal calculation for our problem.

We would like to thank Bart van Tiggelen for developing the calculations presented in this section.

Let us assume the multiple scattering medium to be semi-infinite in the half space $z > 0$.

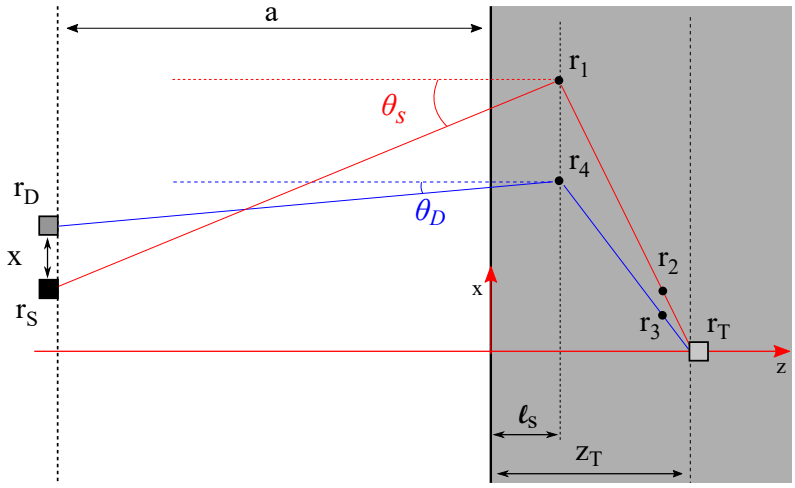


Figure 2.20: Schematic representation and variables involved for notation. The multiple scattering system is in the half-space $z > 0$, while the detection plane is located at position $z = -a$.

When a Dirac pulse is emitted from the point-like source at $\mathbf{r_S}$, the signal received at $\mathbf{r_T}$ is $G(\mathbf{r_T}, \mathbf{r_S}, t)$; i.e., the Green's function between points $\mathbf{r_S}$ and $\mathbf{r_T}$. A part of this signal, referred to as the Time-Reversed Window (TRW), is then selected to produce

$G(\mathbf{r_T}, \mathbf{r_S}, t)\, W\left(\frac{t-t_0}{T}\right)$, where W is the rectangle function. The corresponding signal is flipped in time and sent back from $\mathbf{r_T}$. Finally the signal received at a position $\mathbf{r_D}$ is given by

$$\begin{aligned} F_{t_0}(\mathbf{r_D}, \mathbf{r_S}, t) &= \left[W\left(\frac{-t-t_0}{T}\right) G(\mathbf{r_T}, \mathbf{r_S}, -t) \right] \otimes G(\mathbf{r_D}, \mathbf{r_T}, t) \\ &= \int W\left(\frac{\tau - t_0}{T}\right) G(\mathbf{r_T}, \mathbf{r_S}, \tau)\, G(\mathbf{r_D}, \mathbf{r_T}, t+\tau)\, d\tau \\ &= \int_{t_0 - T/2}^{t_0 + T/2} G(\mathbf{r_T}, \mathbf{r_S}, \tau)\, G(\mathbf{r_D}, \mathbf{r_T}, t+\tau)\, d\tau. \end{aligned}$$

Under the assumption of reciprocity, $G(\mathbf{r_T}, \mathbf{r_S}, t) = G(\mathbf{r_S}, \mathbf{r_T}, t)$ such that $F_{t_0}(\mathbf{r_D}, \mathbf{r_S}, t)$ can be written as

$$F_{t_0}(\mathbf{r_D}, \mathbf{r_S}, t) = \int_{t_0 - T/2}^{t_0 + T/2} G(\mathbf{r_S}, \mathbf{r_T}, \tau)\, G(\mathbf{r_D}, \mathbf{r_T}, t+\tau) d\tau. \tag{2.28}$$

The width of the focal spot can thus be determined by analysing, at instant $t = 0$, the variation of $F_{t_0}(\mathbf{r_D}, \mathbf{r_S}, 0) = \int_{t_0 - T/2}^{t_0 + T/2} G(\mathbf{r_S}, \mathbf{r_T}, \tau)\, G(\mathbf{r_D}, \mathbf{r_T}, \tau) d\tau$. As a function of the distance $X = |\mathbf{r_D} - \mathbf{r_S}|$ around the source, $F_{t_0}(\mathbf{r_D}, \mathbf{r_S}, 0)$ is a statistical estimator of the spatial correlation function $\langle G(\mathbf{r_S}, \mathbf{r_T}, t_0)\, G(\mathbf{r_D}, \mathbf{r_T}, t_0) \rangle$ for a point source located in $\mathbf{r_T}$ [30].

We are interested in following the width of the focal spot as a function of the position t_0 of the TRW. The calculation is more tractable in the frequency domain, which asks for a Laplace transform:

$$C(\mathbf{r_D}, \mathbf{r_S}, \Omega) = \int_0^\infty \langle G(\mathbf{r_S}, \mathbf{r_T}, t)\, G(\mathbf{r_D}, \mathbf{r_T}, t) \rangle e^{i(\Omega + i\epsilon)t} dt$$

Then, by decomposing $G(\mathbf{r_S}, \mathbf{r_T}, t)$ and $G(\mathbf{r_D}, \mathbf{r_T}, t)$ on their frequency components, we can write:

$$C(\mathbf{r_D}, \mathbf{r_S}, \Omega) = \int_0^\infty \int_{-\infty}^\infty \int_{-\infty}^\infty \langle G(\mathbf{r_S}, \mathbf{r_T}, \omega_1)\, G(\mathbf{r_D}, \mathbf{r_T}, \omega_2) \rangle e^{-i\omega_1 t} e^{-i\omega_2 t} e^{i(\Omega + i\epsilon)t} d\omega_1 d\omega_2 dt.$$

Exploiting that $\int_0^\infty e^{i(\Omega + i\epsilon - \omega_1 - \omega_2)t} dt = \delta(\Omega + i\epsilon - \omega_1 - \omega_2)$, we get

$$C(\mathbf{r_D}, \mathbf{r_S}, \Omega) = \int_{-\infty}^\infty \langle G(\mathbf{r_S}, \mathbf{r_T}, \omega_1)\, G(\mathbf{r_D}, \mathbf{r_T}, \Omega + i\epsilon - \omega_1) \rangle d\omega_1.$$

The function $G(\mathbf{r_D}, \mathbf{r_T}, t)$ is real; thus, it is satisfied that $G(\mathbf{r_D}, \mathbf{r_T}, \Omega - \omega) = G(\mathbf{r_D}, \mathbf{r_T}, \omega - \Omega)^*$. By using the change of variables $\omega_1 \to \omega_1 + \Omega/2 + i\epsilon/2$, we obtain:

$$C(\mathbf{r_D}, \mathbf{r_S}, \Omega) = \int_{-\infty}^{\infty} \langle G(\mathbf{r_S}, \mathbf{r_T}, \omega - \Omega/2 - i\epsilon/2) G^*(\mathbf{r_D}, \mathbf{r_T}, \omega + \Omega/2 + i\epsilon/2) \rangle d\omega.$$

The quantity of interest is then $\langle G(\mathbf{r_S}, \mathbf{r_T}, \omega - \Omega/2) G^*(\mathbf{r_D}, \mathbf{r_T}, \omega + \Omega/2) \rangle$, which obeys the following equation [3]:

$$\begin{aligned}\langle G(\mathbf{r_S}, \mathbf{r_T}, \omega - \Omega/2) G^*(\mathbf{r_D}, \mathbf{r_T}, \omega + \Omega/2) \rangle = \\ G_e(\mathbf{r_S}, \mathbf{r_T}, \omega - \Omega/2) G_e^*(\mathbf{r_D}, \mathbf{r_T}, \omega + \Omega/2) + \\ \int_1 \int_2 \int_3 \int_4 G_e(\mathbf{r_S}, \mathbf{r_1}, \omega - \Omega/2) G_e^*(\mathbf{r_D}, \mathbf{r_4}, \omega + \Omega/2) \Gamma(\mathbf{r_1}, \mathbf{r_2}, \mathbf{r_3}, \mathbf{r_4}) \dots \\ G_e(\mathbf{r_2}, \mathbf{r_T}, \omega - \Omega/2) G_e^*(\mathbf{r_3}, \mathbf{r_T}, \omega + \Omega/2) d\mathbf{r_1} d\mathbf{r_2} d\mathbf{r_3} d\mathbf{r_4} \quad (2.29)\end{aligned}$$

where G_e is the effective Green's function.

At this step, we make the following hypothesis:

1. The TRM is supposed to be at a depth $z_T \gg \ell_S$, such that the first term on the right handside of (2.29) can be disregarded.
2. The frequency of the internal oscillations ω is much larger than the frequency of the enveloppe Ω: $\omega \gg \Omega$.
3. Considering the ladder approximation, the vertex function writes:

$$\Gamma(\mathbf{r_1}, \mathbf{r_2}, \mathbf{r_3}, \mathbf{r_4}) = \tilde{P}(\mathbf{r_1}, \mathbf{r_2}) \delta(\mathbf{r_1} - \mathbf{r_4}) \delta(\mathbf{r_2} - \mathbf{r_3}). \quad (2.30)$$

With these assumptions, equation (2.29) is simplified to:

$$\begin{aligned}\langle G(\mathbf{r_S}, \mathbf{r_T}, \omega - \Omega/2) G^*(\mathbf{r_D}, \mathbf{r_T}, \omega + \Omega/2) \rangle = \\ \int_1 \int_2 G_e(\mathbf{r_S}, \mathbf{r_1}, \omega) G_e^*(\mathbf{r_D}, \mathbf{r_1}, \omega) \tilde{P}(\mathbf{r_1}, \mathbf{r_2}) G_e(\mathbf{r_2}, \mathbf{r_T}, \omega) G_e^*(\mathbf{r_2}, \mathbf{r_T}, \omega) d\mathbf{r_1} d\mathbf{r_2},\end{aligned}$$

where only the propagator $\tilde{P}$ still depends on Ω.

After an inverse Laplace transform over Ω , we obtain

$$\langle G\left(\mathbf{r_S},\mathbf{r_T},t\right)G^{*}\left(\mathbf{r_D},\mathbf{r_T},t\right)\rangle =$$
$$\int_1\int_2 G_e\left(\mathbf{r_S},\mathbf{r_1},\omega\right)G_e^{*}\left(\mathbf{r_D},\mathbf{r_1},\omega\right)\tilde{P}\left(\mathbf{r_1},\mathbf{r_2},t\right)G_e\left(\mathbf{r_2},\mathbf{r_T},\omega\right)G_e^{*}\left(\mathbf{r_2},\mathbf{r_T},\omega\right)d\mathbf{r_1}d\mathbf{r_2}. \quad (2.31)$$

Using the theorem of images, the propagator $\tilde{P}\left(\mathbf{r_1},\mathbf{r_2},t\right)$ linking the points $\mathbf{r_1}$ and $\mathbf{r_2}$ in half-space $z>0$ can be deduced from the solution of the diffusion equation in an infinite medium [2].

$$\tilde{P}\left(x_1,x_2,y_1,y_2,z_1,z_2,t\right)=\frac{e^{-\rho_{12}^2/4Dt}}{(Dt)^{3/2}}\left[e^{-(z_1-z_2)^2/4Dt}-e^{-(z_1+z_2+2z_0)^2/4Dt}\right]$$

where $\rho_{12}=\sqrt{\left(x_1-x_2\right)^2+\left(y_1-y_2\right)^2}$ is the lateral distance between points $\mathbf{r_1}$ and $\mathbf{r_2}$ along the sample interface.

On the other hand, we have:

$$\begin{cases}\left|G_e\left(\mathbf{r_2},\mathbf{r_T},\omega\right)\right|^2=\frac{e^{-|\mathbf{r_2}-\mathbf{r_T}|/\ell_S}}{(4\pi)^2|\mathbf{r_2}-\mathbf{r_T}|^2}\\ G_e\left(\mathbf{r_S},\mathbf{r_1},\omega\right)=\frac{e^{ik|\mathbf{r_S}-\mathbf{r_1}|}}{4\pi|\mathbf{r_S}-\mathbf{r_1}|}e^{-\frac{z_1}{2\ell_S\cos\theta_S}}\\ G_e^{*}\left(\mathbf{r_D},\mathbf{r_1},\omega\right)=\frac{e^{-ik|\mathbf{r_D}-\mathbf{r_1}|}}{4\pi|\mathbf{r_D}-\mathbf{r_1}|}e^{-\frac{z_1}{2\ell_S\cos\theta_D}}\end{cases}$$

where, in the expressions for G_e and G_e^{*}, the phase in the skin layer has been neglected. Furthermore, if $|\mathbf{r_S}-\mathbf{r_D}|\ll a$, one can assume $\cos\theta_S=\cos\theta_D=\mu$.

Thus, the integral we have to perform is:

$$\langle G\left(\mathbf{r_S},\mathbf{r_T},t\right)G^{*}\left(\mathbf{r_D},\mathbf{r_T},t\right)\rangle =$$
$$=\iint\frac{1}{(4\pi)^4}\frac{e^{-\frac{|\mathbf{r_2}-\mathbf{r_T}|}{\ell_S}}}{|\mathbf{r_2}-\mathbf{r_T}|^2}\frac{e^{ik|\mathbf{r_S}-\mathbf{r_1}|}}{|\mathbf{r_S}-\mathbf{r_1}|}\frac{e^{-ik|\mathbf{r_D}-\mathbf{r_1}|}}{|\mathbf{r_D}-\mathbf{r_1}|}e^{-z_1/\mu\ell_S}\tilde{P}(\mathbf{r_1},\mathbf{r_2},t)d\mathbf{r_1}d\mathbf{r_2}$$

$$\simeq\iint\frac{e^{ik|\mathbf{r_S}-\mathbf{r}|}}{|\mathbf{r_S}-\mathbf{r}|}\frac{e^{-ik|\mathbf{r_D}-\mathbf{r}|}}{|\mathbf{r_D}-\mathbf{r}|}e^{-z/\mu\ell_S}\frac{e^{-\rho^2/4Dt}}{(Dt)^{3/2}}\left[e^{-(z-z_T)^2/4Dt}-e^{-(z+z_T+2z_0)^2/4Dt}\right]dzd^2\rho,$$

since the term $e^{-\frac{|\mathbf{r_2}-\mathbf{r_T}|}{\ell_S}}/|\mathbf{r_2}-\mathbf{r_T}|^2$ selects out the value of the integrand at $\mathbf{r_2}=\mathbf{r_T}$.

Also, we have

$$|\mathbf{r_S}-\mathbf{r}|=\sqrt{a^2+\rho^2},$$

which can be approximated as

$$|\mathbf{r_D} - \mathbf{r}| = \sqrt{a^2 + (\rho\cos\phi - X)^2 + (\rho\sin\phi)^2}$$

$$= \sqrt{a^2 + \rho^2 - 2\rho X\cos\phi + X^2}$$

$$\simeq \sqrt{a^2+\rho^2}\sqrt{1 - \frac{2\rho X\cos\phi}{(a^2+\rho^2)}}$$

$$\simeq \sqrt{a^2+\rho^2}\left[1 - \frac{\rho X\cos\phi}{(a^2+\rho^2)}\right].$$

So, we obtain

$$\langle G(\mathbf{r_S}, \mathbf{r_T}, t)\, G^*(\mathbf{r_D}, \mathbf{r_T}, t)\rangle$$

$$\simeq \int \rho d\rho \int d\phi \int dz \frac{e^{-z/\mu\ell_S}}{a^2+\rho^2} e^{ik\frac{\rho X\cos\phi}{\sqrt{a^2+\rho^2}}} \frac{e^{-\rho^2/4Dt}}{(Dt)^{3/2}} \left[e^{-(z-z_T)^2/4Dt} - e^{-(z+z_T+2z_0)^2/4Dt}\right] \quad (2.32)$$

The term depending on z in the integrand does not vary much over a thickness ℓ_S. Thus, we can do the approximation

$$\int dz e^{-z/\mu\ell_S} f(z) \simeq \mu\ell_S f(0).$$

The integral we have to calculate is

$$\langle G(\mathbf{r_S}, \mathbf{r_T}, t)\, G^*(\mathbf{r_D}, \mathbf{r_T}, t)\rangle$$

$$\simeq \int_0^\infty \rho d\rho \int_0^{2\pi} d\phi \left(\frac{\mu\ell_S}{a^2+\rho^2}\right) \frac{e^{-\rho^2/4Dt}}{(Dt)^{3/2}} \left[e^{-z_T^2/4Dt} - e^{-(z_T+2z_0)^2/4Dt}\right] e^{ik\frac{\rho X\cos\phi}{\sqrt{a^2+\rho^2}}}.$$

Using that

$$\begin{cases} \cos\theta = a/\sqrt{a^2+\rho^2} \\ \sin\theta = \rho/\sqrt{a^2+\rho^2} \\ \tan\theta = \rho/a \\ d\rho = (a/\cos^2\theta)\, d\theta \end{cases},$$

it is possible to change the integration variables to obtain

$$\langle G(\mathbf{r_S}, \mathbf{r_T}, t)\, G^*(\mathbf{r_D}, \mathbf{r_T}, t)\rangle$$

$$\simeq \ell_S \int_0^{\pi/2} d\theta \sin\theta \frac{e^{-a^2\tan^2\theta/4Dt}}{(Dt)^{3/2}} \left[e^{-z_T^2/4Dt} - e^{-(z_T+2z_0)^2/4Dt}\right] \int_0^{2\pi} d\phi e^{ikX\sin\theta\cos\phi}$$

$$\simeq \ell_S \int_0^{\pi/2} d\theta \sin\theta \frac{e^{-a^2\tan^2\theta/4Dt}}{(Dt)^{3/2}} \left[e^{-z_T^2/4Dt} - e^{-(z_T+2z_0)^2/4Dt}\right] J_0(kX\sin\theta).$$

Where we finally arrive to the following formula

$$\langle G(\mathbf{r_S}, \mathbf{r_T}, t)\, G^*(\mathbf{r_D}, \mathbf{r_T}, t)\rangle$$

$$\simeq \ell_S \left[\frac{e^{-z_T^2/4Dt} - e^{-(z_T+2z_0)^2/4Dt}}{(Dt)^{3/2}}\right] \int_0^{\pi/2} d\theta \sin\theta e^{-a^2\tan^2\theta/4Dt} J_0(kX\sin\theta) \quad (2.33)$$

When the whole received signal is flipped in time and backpropagated, the resulting signal received at $\mathbf{r_D}$ writes

$$F(\mathbf{r_D}, \mathbf{r_S}, t) = \int_{-\infty}^{+\infty} G(\mathbf{r_S}, \mathbf{r_T}, \tau)\, G(\mathbf{r_D}, \mathbf{r_T}, t+\tau)\, d\tau$$

Thus, the focal spot can be predicted by analysing the variation of $F(\mathbf{r_D}, \mathbf{r_S}, t=0)$ against the distance $X = |\mathbf{r_D} - \mathbf{r_S}|$ between the orignal source and the receiver in the focal plane.

Time-reversal focusing in a disordered scattering medium is a self-averaging process [30], such that we have to calculate the corresponding average:

$$F(X,0) = \int_0^{+\infty} dt \langle G(\mathbf{r_S}, \mathbf{r_T}, t)\, G(\mathbf{r_D}, \mathbf{r_T}, t)\rangle$$

$$= \int_0^{+\infty} dt \ell_S \left[\frac{e^{-z_T^2/4Dt} - e^{-(z_T+2z_0)^2/4Dt}}{(Dt)^{3/2}}\right] \int_0^{\pi/2} d\theta \sin\theta e^{-a^2\tan^2\theta/4Dt} J_0(kX\sin\theta)$$

Defining the variable $b = a^2\tan^2\theta + z_T^2$ or $b = a^2\tan^2\theta + (z_T+2z_0)^2$, we can apply the following known solution

$$\int_0^{+\infty} \frac{e^{-b^2/4Dt}}{(Dt)^{3/2}} dt = \frac{2\sqrt{\pi}}{Db}.$$

Thus, we finally obtain

$$F(X,0) \propto \int_0^{\pi/2} d\theta \sin\theta J_0(kX\sin\theta) \left[\frac{1}{\sqrt{a^2\tan^2\theta + z_T^2}} - \frac{1}{\sqrt{a^2\tan^2\theta + (z_T+2z_0)^2}}\right],$$

or

$$F(X,0) \propto \int_0^{\pi/2} d\theta \sin 2\theta J_0(kX\sin\theta) \left[\frac{1}{\sqrt{a^2\sin^2\theta + z_T^2\cos^2\theta}} - \frac{1}{\sqrt{a^2\sin^2\theta + (z_T+2z_0)^2\cos^2\theta}}\right]. \quad (2.34)$$

From equation 2.34 it is possible to do the corresponding numerical calculations to predict experimental results. Figure 2.21 shows the variation of the half-width stationary time-reversal focusing in terms of the inverse of the depths z_T. The curve is plotted in adimensional units: the half-width times the wavevector against the source's plane distance over the TRM depth. The theoretical model is compared with the width expected from cuspid-like focusing given by the equation [26, 31]

$$\Psi \propto \exp\left(-\frac{z_T k |x|}{a}\right). \quad (2.35)$$

In expresion (2.35) it is needed to consider an offset of the focal width, since it is no

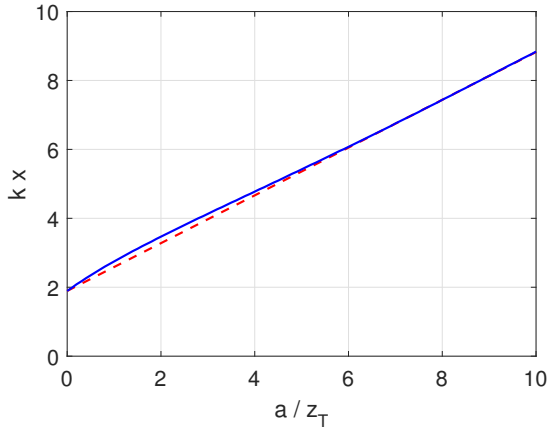


Figure 2.21: Comparison of the half-width at half-maximum for the time-reversal theoretical model given by equation (2.34) (solid blue line) and that given by (2.35) with an extra offset (dashed red line). The width predicted by both models are plotted in terms of the ratio between the source distance with the medium (a) and the TRM depth z_T. For large values of a/z_T (greater than 6) the two curves are identical, having the same slope $\ln(2) \simeq 0.69$.

contemplated by it. This offset arises from the difraction limit λ and is calculated from the model (2.34). The value obtained for the offset gives a value of $1.89kx$, which corresponds to a half-width of $1.89\lambda/2\pi \sim \lambda/\pi$.

For large values of a/z_T, greater than 6, the tendency of both curves is identical. The dependence of the focal width becomes linear, with a slope value $\ln(2) \simeq 0.69$, in agreement with equation (2.35) for $a \gg z_T$.

Experimental approach

To experimentally proceed with the physical situation described, the setup shown in figure 2.22 was implemented. An array of transducers, made of 64 channels is located at a distance a from surface of the multiple scattering medium. A TRM is located inside the granular medium, at a depht z_T from its surface. All the system is immersed in water. In the forward step, the system is excited by a 2-cycles sinusoid with central frequency 2.0MHz, emitted from the array's central channel and received by the TRM. In the backward step, the TRM flips in time the acquired signal and send it back to the array, which measures the acoustic wavefield with the 64 channels. The process is repeated for several configurations for dirorder averaging.

The experiments performed to characterize the time-reversal focusing can be divided into three groups. First, the dependence of the focusing width on the distance a was studied, keeping fixed the depth of the TRM z_T. This first analisys allows us to verify the far-field assumption. Second, we studied the dependence of the focusing width on the depth z_T of the TRM, keeping fixed the distance between the source and the multiple scattering medium a. Finally, we kept both the distance a and the depth z_T fixed and

studied the focusing width as a function of time by time-reversing selected time windows in the transmitted coda obtained in step one.

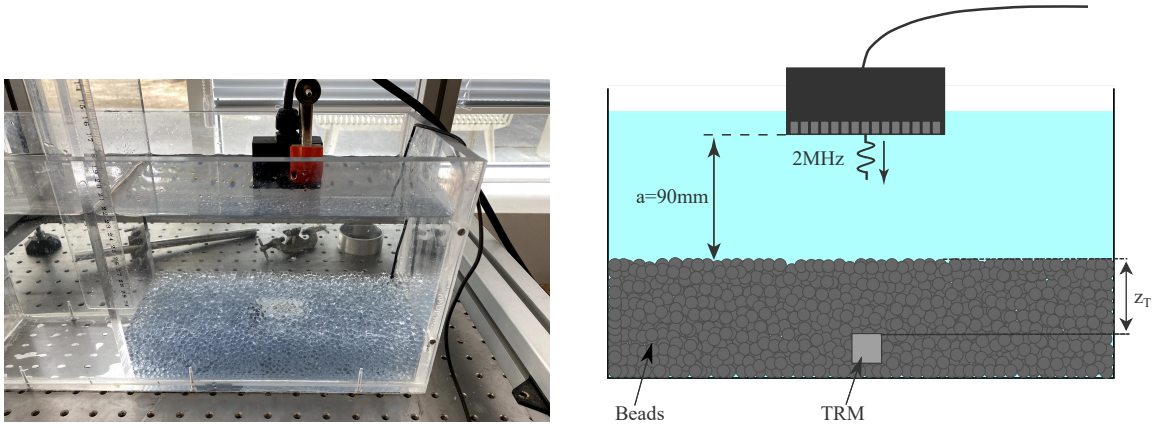


Figure 2.22: Experimental setup used for time-reversal focusing when the TRM is immersed in the multiple scattering medium. (a) Photograph of the experimental setup, where the transducer can be seen immersed in the medium. Here the beads used correspond to 5mm. (b) Schematic representation of the setup detailing the variables to be considered during the experiments, such as the distance a between the source and the multiple scattering system or the depth of the TRM z_T.

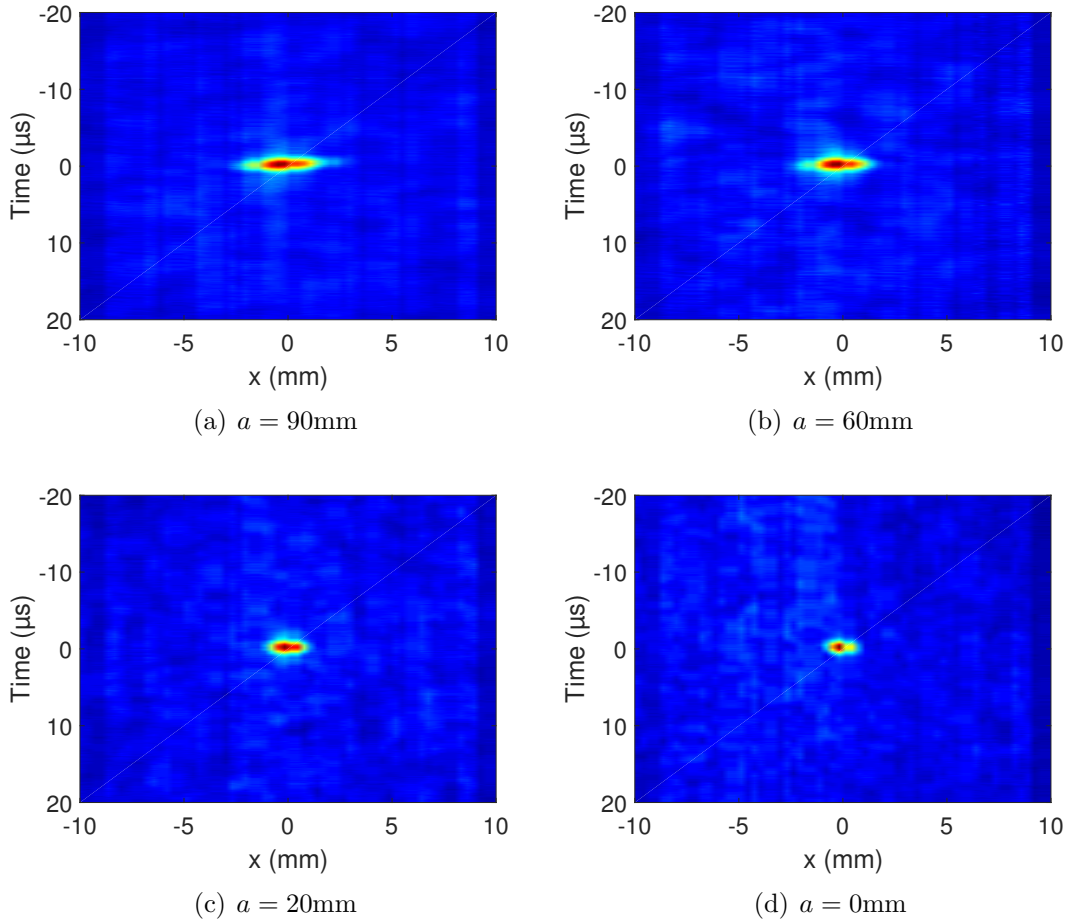
2.2.4 Stationary time-reversal

Width dependence with the source's distance

In this section, we present the results obtained for the time-reversal focusing while keeping fixed the depth z_T of the TRM and varying the distance between the source and the multiple scattering medium a. For this purpose, $z_T = 25$mm was chosen. The distance a was varied from 90mm to the surface of the diffusive medium. The source emits 2-cycle of a sine wave with central frequency 2.0MHz. The wave detected by the TRM is filtered with a bandpass between 1.0MHz and 3.0MHz. Eight different configurations of disorder were measured for the two bead sizes considered.

In this experiment the quantity that varies is a. Therefore, based on the equation (2.26), we can expect the focal width of the time-reversal to have a linear dependence on the distance between the source's plane and the multiple scattering medium. Figure 2.23 shows the evolution of focusing as a function of distance a for 1.5mm beads. Figure 2.24 show the same evolution for 5mm beads.

Plotting the focal width as a function of distance a, we find that the dependence predicted by the equation (2.26) is satisfied, as shown in the figure 2.25. The negative values of a correspond to the source going inside the multiple scattering medium.



(a) $a = 90$mm (b) $a = 60$mm

(c) $a = 20$mm (d) $a = 0$mm

Figure 2.23: Average B-scan of time-reversal focusing evolution as a function of the distance between the source and the multiple scattering medium for 1.5mm beads.

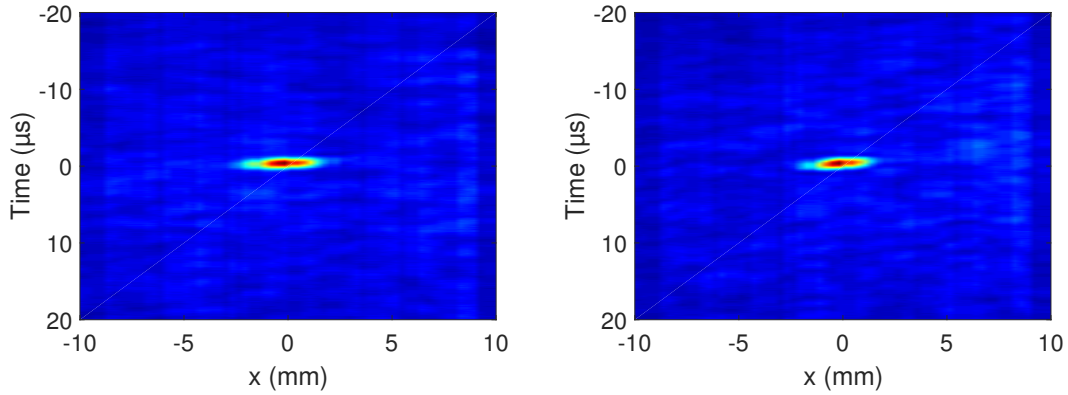
Fitting the experimental results for positive values of a, we have that the expression for the focal half-width at half-maximum as a function of distance are, for both bead sizes

$$\delta_{1.5\text{mm}} \simeq 0.0101a + 0.604\text{mm} \tag{2.36}$$

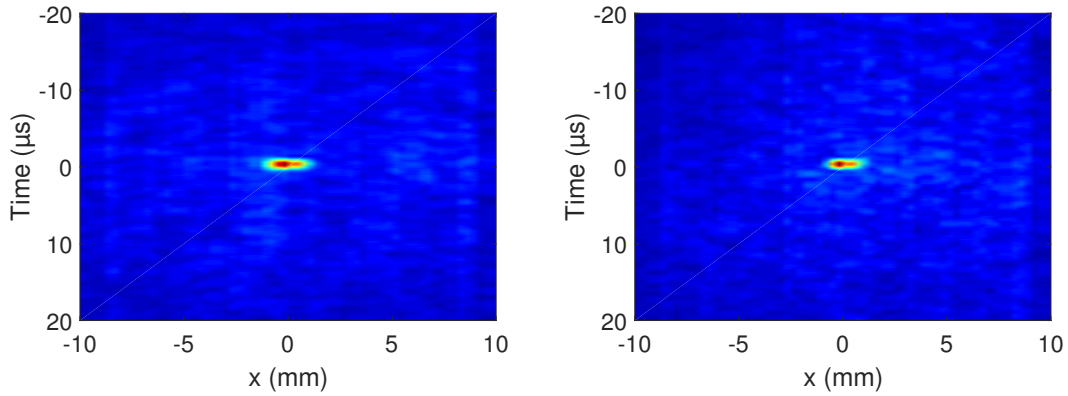
$$\delta_{5\text{mm}} \simeq 0.00837a + 0.666\text{mm}. \tag{2.37}$$

From figure 2.25, and equations (2.36) and (2.37), we see how the focal width for a fixed depth z_T varies linearly with the distance between the source and the multiple scattering medium. This behavior is faithful to what is expected from the expression (2.26), where the correlation length varies linearly with the distance between the diffusive medium and the viewing plane. Furthermore, we see that the focal width saturates at a minimum value when the source starts to be in contact with the multiple scattering medium.

From equations (2.36) and (2.37), we can say that time-reversal focusing behaves

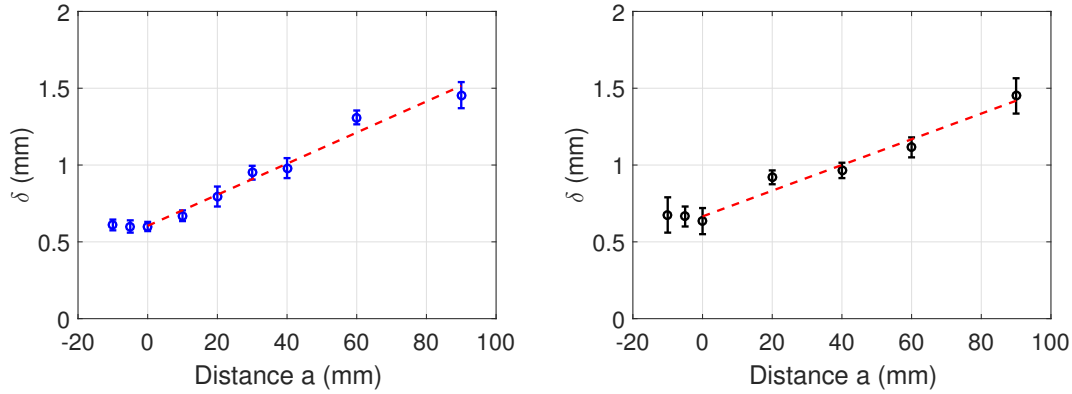


(a) $a = 90$mm (b) $a = 60$mm



(c) $a = 20$mm (d) $a = 0$mm

Figure 2.24: Average B-scan of time-reversal focusing evolution as a function of the distance between the source and the multiple scattering medium for 5mm beads.



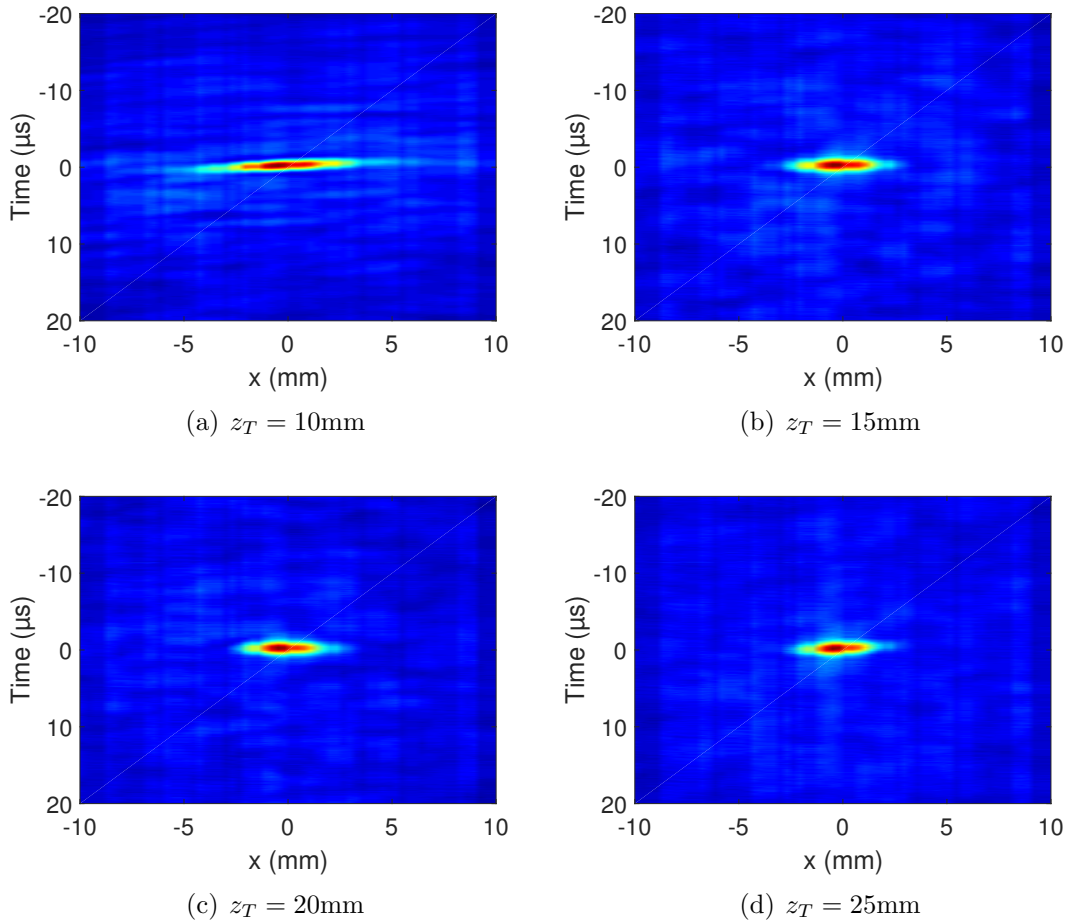
(a) (b)

Figure 2.25: Focal half-width dependence on the distance between source and multiple scattering medium. (a) 1.5mm beads; (b) 5mm beads.

similarly for both bead sizes. Comparing the fits with what is expected in the experiment using equation (2.26), we see that the slopes differ from the ratio λ/z_T by a coefficient near the value of $1/3$. However, what is interesting is the appearance of an independent

term of similar value for the two fits. Also, when the source is located inside the medium, we see how the focal width becomes constant equal to this independent term. Thus, such saturation in the time-reversal focusing corresponds to the effect of the near-field. Finally, we may say that such term depends only on the experimental conditions, and not strictly to the bead size utilized.

Width dependence with the depth



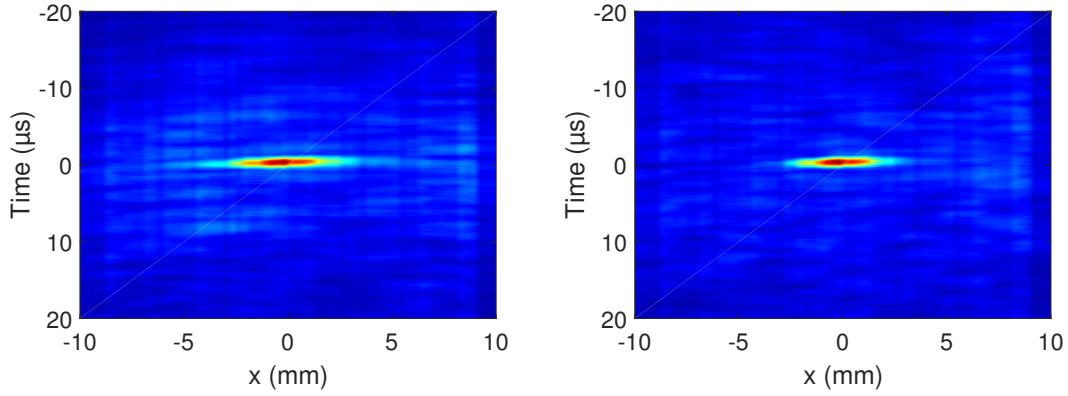
(a) $z_T = 10$mm (b) $z_T = 15$mm

(c) $z_T = 20$mm (d) $z_T = 25$mm

Figure 2.26: Average B-scan of the time-reversal focusing evolution as a function of the TRM depth. We can see how the focusing decreases the larger the z_T is, as expected from the expression (2.26). Results obtained for 1.5mm beads.

In this experiment we proceeded as follows. The source located at a distance $a = 90$mm emits 2-cycle of a sine wave with central frequency of 2.0MHz. The TRM, which is located at a depth z_T that is varied between 10mm and 25mm, detects the transmitted wave. This wave is bandpass filtered between 1.0MHz and 3.0MHz to remove both low-frequency ballistic contribution and the electronic noise. The acquired signal is computationally time-reversed and re-emitted with the TRM. The piezoelectric array now works as a receiver, detecting the time-reversed acoustic field. For each depth z_T the process is

repeated for eight different configurations of disorder. Figure 2.26 shows the evolution of the time-reversal field as a function of the depth z_T for beads of 1.5mm diameter. One can see how the time-reversal focusing decreases as z_T increases. Figure 2.27 shows the same evolution for bead size 5mm.



(a) $z_T = 10$mm (b) $z_T = 15$mm

(c) $z_T = 20$mm (d) $z_T = 25$mm

Figure 2.27: Average B-scan of the time-reversal focusing evolution as a function of the TRM depth. Again, the focusing gets narrower as z_T gets larger. Results obtained for 5mm beads.

The experiment was performed for z_T values of 10mm, 15mm, 20mm and 25mm. As seen in the previous section, we should expect a focal width dependence that can be approximated as $\frac{K_1}{z_T} + K_2$. The experimental results obtained for both bead sizes, along their respective fits, are shown in figure 2.28. Indeed, we found that the fits obtained are in good agreement with the experimental results. The parameters found for the fits are similar, given by

$$\delta_{1.5\text{mm}} \simeq \frac{15.1\text{mm}^2}{z_T} + 0.862\text{mm} \tag{2.38}$$

and

$$\delta_{5\text{mm}} \simeq \frac{13.6\text{mm}^2}{z_T} + 0.890\text{mm}. \tag{2.39}$$

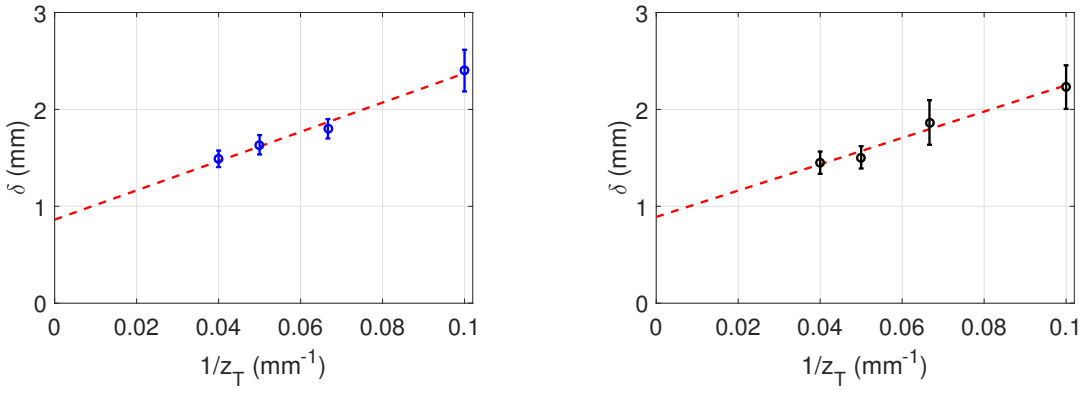


Figure 2.28: Evolution of the focal half-width as a function of the depth at which the TRM is placed, z_T. (a) Results for 1.5mm diameter beads. (b) Results for 5mm diameter beads.

The slopes obtained for the different bead size are quite similar. In both cases the results obey the tendency described in figure 2.21. Furthermore, by comparison with equation (2.35), it is expected to have a slope comparable to $\lambda a \ln 2/2\pi \simeq 7.45\text{mm}^2$. We found that the slopes determined experimentally for both bead sizes are about twice the value expected from the model.

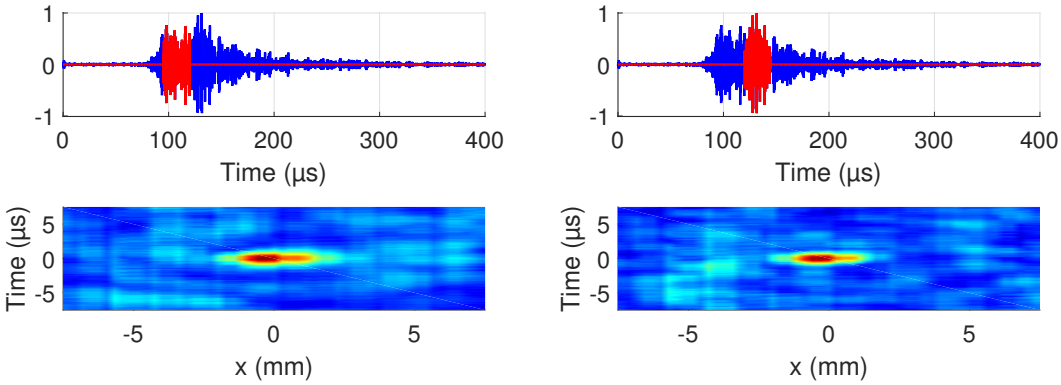
On the other hand, we obtain an independent term on the corresponding fits. Due to the difraction limit, the minimum value for time-reversal focusing is settle by $\lambda/2$, thus explainning the presence of such independent term. In our case, it should be roughly λ/π, as discussed in section 2.2.3. Considering our experimental conditions, $\lambda/\pi \sim 0.24$mm, which is about three times smaller than the values we have determined for our data.

2.2.5 Dynamic time-reversal

So far we have analyzed the stationary time-reversal, i.e., time-reversing the whole signal acquired by the TRM and studying the dependence of the focusing in terms of the distance a between the source and the medium and in terms of the depth of the TRM z_T. For the dynamic time-reversal we will set $a = 90$mm and $z_T = 25$mm, so that time is the only relevant variable. The experiment is repeated over eight different configurations of disorder for averaging the time-reversal focusing acquired.

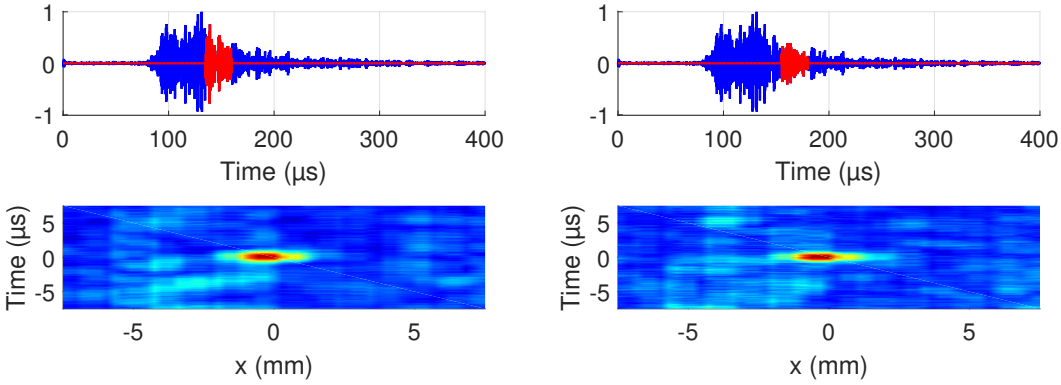
To perform the dynamic time-reversal, the coda signal recorded by the TRM is divided into time windows of 25μs duration. With this choice, the signal-to-noise ratio of the time-reversed wavefield improves, compared with smaller time windows. The time step chosen between two consecutive time windows is 5μs, to maintain the time resolution of the time-reversal focusing width.

In figure 2.29 time-reversal focusing is shown for several time windows. In 2.29(e) the fit realized for the half-width at half-maximum is presented. The fitting function utilized corresponds to the equation (2.33). The obtained value for the diffusion coefficient is



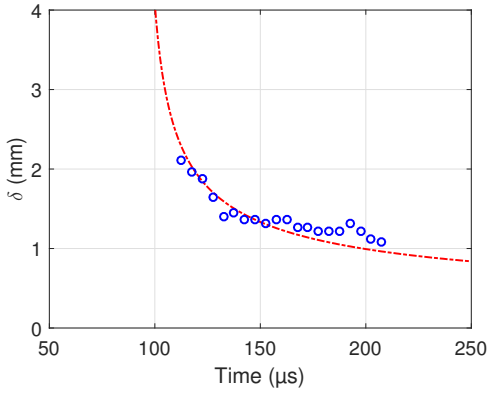
(a) t=108μs

(b) t=133μs



(c) t=148μs

(d) t=168μs

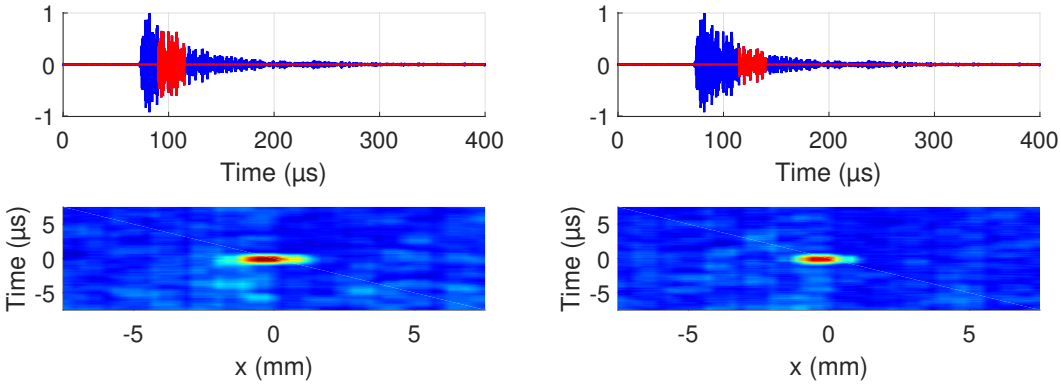


(e)

Figure 2.29: Time-dependent focal width for the dynamic time-reversal for 1.5mm diameter beads. The focal width decreases as the time of the window goes deeper in the coda wave, as presented in figures from (a) to (d). (e) Results obtained for the half-width at half-maximum dependence with the time-reversed time window. The experimental results (blue circles) are fitted using equation (2.33) (red dashed line), giving a diffusion coefficient of $D_{1.5\text{mm}} \simeq 0.82\text{mm}^2/\mu\text{s}$.

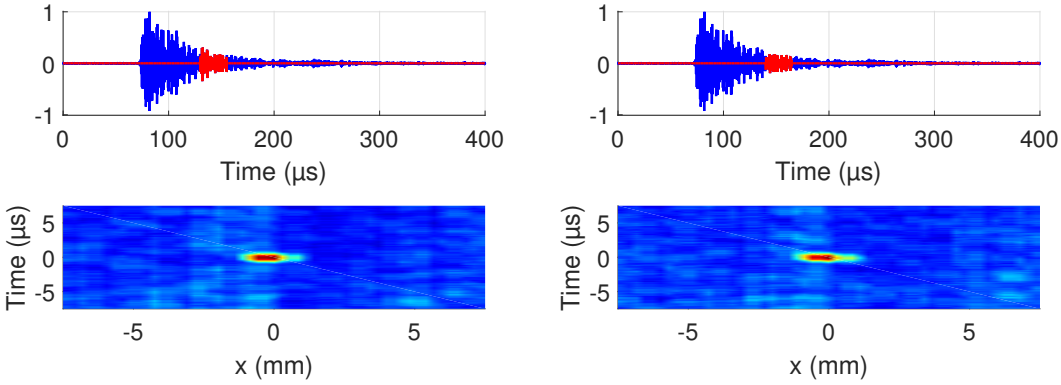
$$D_{1.5\text{mm}} = (0.82 \pm 0.07)\,\text{mm}^2/\mu\text{s}. \tag{2.40}$$

Analogously, for 5mm beads the results shown in figure 2.30 were obtained. The



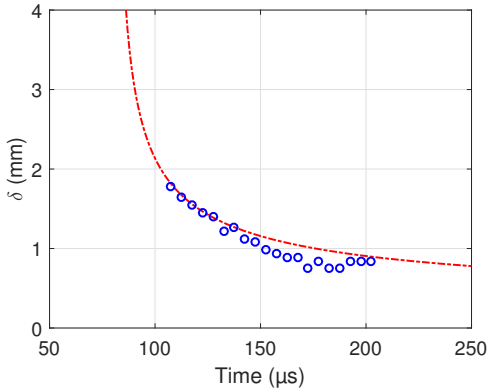
(a) t=103μs

(b) t=128μs



(c) t=143μs

(d) t=153μs



(e)

Figure 2.30: Time-dependent focal width for the dynamic time-reversal for 5mm diameter beads. The experimental results obtained for the focal half-width are fitted using equation (2.33) (blue circles and red dashed line respectivly). The diffusion coefficient calculated from the fit is $D_{5\text{mm}} \simeq 1.01\text{mm}^2/\mu\text{s}$.

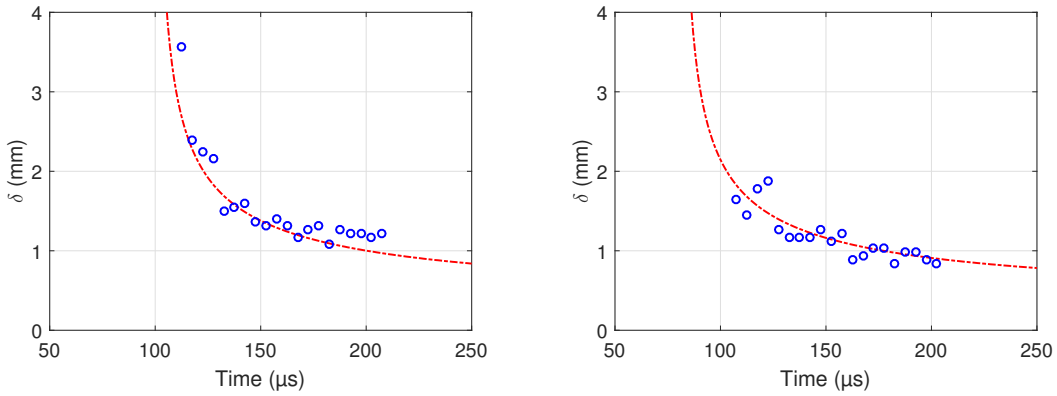
diffusion coefficient inferred from the fit is

$$D_{5\text{mm}} = (1.01 \pm 0.10)\,\text{mm}^2/\mu\text{s} \tag{2.41}$$

The values obtained for both diffusion coefficients are in good agreement with the

methods introduced at the beginning ot this chapter. Utilizing the theoretical model given by equation (2.33) it was possible to relate the time-reversal focusing to the transport parameters and to calculate the diffusion coefficient of our system.

As a final experiment, we compared the time-reversal experiments presented in this section with a single configuration experiment. Exploitting the self-averaging behaviour of time-reversal process, it would be expected to have a similar result in a single realization of the experiment with those obtained after averaging over different disorder configurations [30].



(a) 1.5mm bead size. (b) 5mm bead size.

Figure 2.31: Time-dependent focal width of the dynamic time-reversal for one particular configuration of disorder. (a) Experimental results obtained for 1.5mm diameter beads. The data is fitted using equation (2.33) (blue circles and red dashed line respectivly). The diffusion coefficient calculated for this configuration is $D \simeq 0.89\text{mm}^2/\mu\text{s}$. (b) Experimental results for 5mm diameter beads. The diffusion coefficient calculated for this configuration is $D \simeq 0.91\text{mm}^2/\mu\text{s}$.

By analyzing each configuration of the experiment, the results seems consistent with what was obtained after averaging. In figure 2.31 are presented the experimental results for a particular disorder configuration (for both 1.5mm and 5mm beads). Once again, the fit is done by applying equation (2.33). Even if the global trend is obeyed, there are discrepancies with what obtained after averaging. The values calculated for the diffusion coefficient for every configuration is enclosed around an errorbar of about 10% of the averaged quantity.

For the 1.5mm bead size the diffusion coefficient calculated was $D_{1.5\text{mm}} \simeq 0.82\text{mm}^2/\mu\text{s}$, meanwhile for each independent configuration the values obtained are in the range $D = (0.83 \pm 0.11)\,\text{mm}^2/\mu\text{s}$. The results for a particular configuration are presented in figure 2.31(a).

For the 5mm bead size the diffusion coefficient calculated was $D_{5\text{mm}} \simeq 1.01\text{mm}^2/\mu\text{s}$. Again, the values determined for independent configurations are in the range of about 10% of the average value, obtainning $D = (1.00 \pm 0.12)\,\text{mm}^2/\mu\text{s}$. The results for a particular configuration is presented in figure 2.31(b).

Comparing the values measured by dynamic time-reversal with those obtained by other methods, we can see that the diffusion coefficient is in the expected order of magnitude.

2.3 Discussion and conclusions

Throughout this chapter, the determination of transport parameters for the system under consideration was studied in several ways. First, the time-of-flight distribution (the average time-dependent intensity) was studied as a means to determine the absorption time, the diffusion coefficient and the transport mean free path. In one case, the time of flight distribution was analyzed using a solution of the diffusion equation, under the assumption that the intensity is purely diffusive. On the other case, the intensity exhibits a behaviour intermediate between a purely ballistic and a purely diffusive regime. Thus, the radiative transport theory is more accurate to face the situation.

Then, the coherent backscattering cone were presented and implemented to measure both the diffusion coefficient and the transport mean free path independently. In particular, for the case of the small beads, we have a discrepancy in the value determined for ℓ^*, where by analysis of the TOF we obtain a value that is half of what is obtained through the CBE experiment. However, in the first one, we assume that the transport velocity is equal to the propagation velocity in water, which is not necessarily true. Indeed, with the values obtained for the diffusion coefficient and the transport mean free path, we determined that the transport velocity for our system is $v_T \simeq 0.68\text{mm}/\mu\text{s}$, value that is near half of the velocity in water. Such a value, compared with the state of the art, indicates the presence of resonances in our scatterers [14, 15].

Finally, time-reversal was used to measure the diffusion coefficient D, which is undoubtly the most important contribution of this chapter. We used an experimental set-up where a source is placed in the far-field from the multiple scattering medium, while the TRM is immersed in the system at a depth larger than the mean free path. In such a configuration, the diffusion coefficient can be inferred by following the focal spot measured in a plane parallel to the medium's surface and containing the source. The full theory was developed with the help of Bart Van Tiggelen. From a practical point of view, this method is of course less practicable than the coherent backscattering cone, since it requires the TRM to be placed inside the medium. However, it has the advantage to be a self-averaging method. Time-reversal is actually known to be a self-averaging process [30]. This sugests that the diffusion coefficient can be determined on one single configuration of disorder. A clear example of this is presented in figure 2.31, where the diffusion coefficient is obtained from one single configuration and compared to the one measured from the average over eight configurations. When using the CBE, the average is needed over many configurations of disorder (70 configurations in the case of Tourin et al. [10]). Finally, it should be pointed out that this method is nothing else but a way of measuring

the correlation function of the acoustic wave field which would be produced by a source placed at the TRM position. It also means that the depth of such a source can be retrieved by measuring the spatial correlation of the resulting field in far-field outside the medium.

References

[1] JH Page, HP Schriemer, AE Bailey, and DA Weitz. Experimental test of the diffusion approximation for multiply scattered sound. *Physical Review E*, 52(3):3106, 1995.

[2] Eric Akkermans and Gilles Montambaux. *Mesoscopic physics of electrons and photons*. Cambridge university press, 2007.

[3] Ping Sheng. *Introduction to wave scattering, localization and mesoscopic phenomena*, volume 88. Springer Science & Business Media, 2006.

[4] JCJ Paasschens. Solution of the time-dependent boltzmann equation. *Physical Review E*, 56(1):1135, 1997.

[5] Hao Zhou, Xiaoping Jia, Li-Yun Fu, and Arnaud Tourin. Monte carlo simulations of ultrasound scattering and absorption in finite-size heterogeneous materials. *Physical Review Applied*, 16(3):034009, 2021.

[6] Arnaud Tourin, Arnaud Derode, Aymeric Peyre, and Mathias Fink. Transport parameters for an ultrasonic pulsed wave propagating in a multiple scattering medium. *The Journal of the Acoustical Society of America*, 108(2):503–512, 2000.

[7] Pierre-Etienne Wolf and Georg Maret. Weak localization and coherent backscattering of photons in disordered media. *Physical review letters*, 55(24):2696, 1985.

[8] Meint P Van Albada and Ad Lagendijk. Observation of weak localization of light in a random medium. *Physical review letters*, 55(24):2692, 1985.

[9] G Bayer and T Niederdränk. Weak localization of acoustic waves in strongly scattering media. *Physical review letters*, 70(25):3884, 1993.

[10] Arnaud Tourin, Arnaud Derode, Philippe Roux, Bart A Van Tiggelen, and Mathias Fink. Time-dependent coherent backscattering of acoustic waves. *Physical review letters*, 79(19):3637, 1997.

[11] Julien de Rosny, Arnaud Tourin, and Mathias Fink. Coherent backscattering of an elastic wave in a chaotic cavity. *Physical review letters*, 84(8):1693, 2000.

[12] LA Cobus, BA Van Tiggelen, A Derode, and JH Page. Dynamic coherent backscattering of ultrasound in three-dimensional strongly-scattering media. *The European Physical Journal Special Topics*, 226(7):1549–1561, 2017.

[13] Laura A Cobus, SE Skipetrov, Alexandre Aubry, BA Van Tiggelen, Arnaud Derode, and John H Page. Anderson mobility gap probed by dynamic coherent backscattering. *Physical Review Letters*, 116(19):193901, 2016.

[14] Henry P Schriemer, Michael L Cowan, John H Page, Ping Sheng, Zhengyou Liu, and David A Weitz. Energy velocity of diffusing waves in strongly scattering media. *Physical Review Letters*, 79(17):3166, 1997.

[15] Benoit Tallon, Thomas Brunet, and John H Page. Ultrasonic wave transport in concentrated disordered resonant emulsions. *arXiv preprint arXiv:2208.11684*, 2022.

[16] Mathias Fink. Time reversal of ultrasonic fields. i. basic principles. *IEEE transactions on ultrasonics, ferroelectrics, and frequency control*, 39(5):555–566, 1992.

[17] Arnaud Derode, Philippe Roux, and Mathias Fink. Robust acoustic time reversal with high-order multiple scattering. *Physical review letters*, 75(23):4206, 1995.

[18] Mathias Fink. Time reversed acoustics. *Physics today*, 50(3):34–40, 1997.

[19] Arnaud Tourin, Arnaud Derode, and Mathias Fink. Sensitivity to perturbations of a time-reversed acoustic wave in a multiple scattering medium. *Physical review letters*, 87(27):274301, 2001.

[20] N Pérez, Orientador Dr Carlos Negreira, Tribunal Dr Carlos Negreira, Julio Adamowski, Hugo Fort, Stefan Catheline, and Rafael Canetti. *Inversión temporal de ondas ultrasónicas en cavidades acústicas*. PhD thesis, PhD. thesis in physics. University of the Republic, Uruguay, 2006.

[21] Mathias Fink, Didier Cassereau, Arnaud Derode, Claire Prada, Philippe Roux, Mickael Tanter, Jean-Louis Thomas, and François Wu. Time-reversed acoustics. *Reports on progress in Physics*, 63(12):1933, 2000.

[22] Didier Cassereau, Franqois Wu, and Mathias Fink. Limits of self-focusing using closed time-reversal cavities and mirrors-theory and experiment. In *IEEE Symposium on Ultrasonics*, pages 1613–1618. IEEE, 1990.

[23] Mathias Fink. Time-reversed acoustics. *Scientific American*, 281(5):91–97, 1999.

[24] Arnaud Tourin. *Diffusion multiple et renversement du temps des ondes ultrasonores*. PhD thesis, Université Paris, 1999.

[25] Julien De Rosny, Arnaud Tourin, Arnaud Derode, Bart Van Tiggelen, and Mathias Fink. Relation between time reversal focusing and coherent backscattering in multiple scattering media: A diagrammatic approach. *Physical Review E*, 70(4):046601, 2004.

[26] BA Van Tiggelen. Green function retrieval and time reversal in a disordered world. *Physical review letters*, 91(24):243904, 2003.

[27] Pieter Hendrik van Cittert. Die wahrscheinliche schwingungsverteilung in einer von einer lichtquelle direkt oder mittels einer linse beleuchteten ebene. *Physica*, 1(1-6):201–210, 1934.

[28] Frederik Zernike. The concept of degree of coherence and its application to optical problems. *Physica*, 5(8):785–795, 1938.

[29] Joseph W Goodman. *Statistical optics*. John Wiley & Sons, 2015.

[30] Arnaud Derode, Arnaud Tourin, and Mathias Fink. Random multiple scattering of ultrasound. ii. is time reversal a self-averaging process? *Physical Review E*, 64(3):036606, 2001.

[31] Eric Akkermans, PE Wolf, and R Maynard. Coherent backscattering of light by disordered media: Analysis of the peak line shape. *Physical review letters*, 56(14):1471, 1986.

Chapter 3

Time-reversal in dry granular media for triggering rearrangements

Contents

3.1 Fundamentals of dry granular media 78

3.1.1 A dry assembly of grains as an effective elastic medium 78

3.1.2 A dry assembly of grains as a disordered medium 79

3.1.3 The importance of the contact force network 80

3.1.4 Jamming and unjamming 81

3.1.5 Elastic wave propagation and scattering 84

3.2 Proof-of-principle experiment: time-reversal in a chaotic cavity 86

3.2.1 Time-reversal in a 2D chaotic cavity 87

3.2.2 Time-reversal experiment in a 3D chaotic cavity 88

3.2.3 Bead dropping by time-reversal focusing 90

3.3 Time-reversal experiment through a dry granular medium . 92

3.3.1 Experimental setup 93

3.3.2 Sample preparation protocol 93

3.3.3 Single-channel time-reversal experiment 98

3.4 Time-reversal as a means for triggering rearrangement 104

3.4.1 Single-channel time reversal 104

3.5 Discussion and conclusions 106

References 109

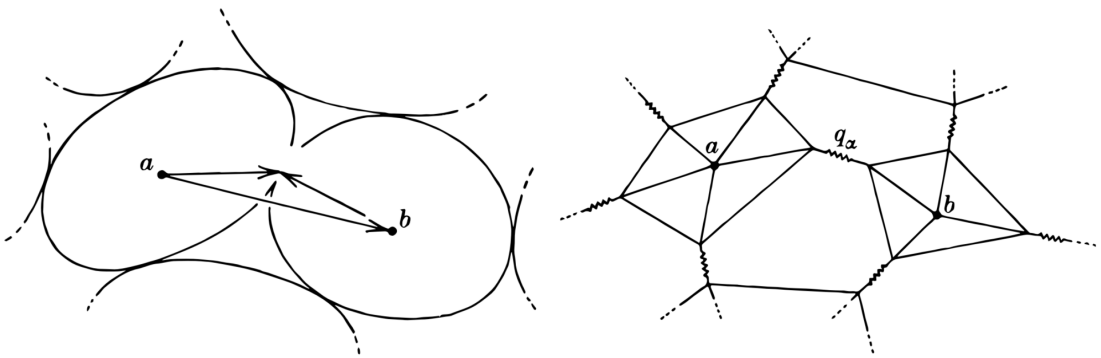
In the previous chapter, we investigated ultrasound wave transport in immersed granular media. We first used two classical approaches based on the study of respectively the average time-dependent transmitted intensity and the coherent backscattering effect. Then we introduced a new method based on time-reversal focusing and showed that the inferred value of the diffusion coefficient is consistent with that measured with the two previous approaches. It is quite amusing to note that the characteristic parameter of an irreversible process (diffusion of the average intensity) can be inferred from a time-reversal experiment.

In the present chapter, time-reversal focusing will be shown to be a means for remotely triggering controlled rearrangements in a confined granular media consisting of a glass bead packing under an external applied pressure.

3.1 Fundamentals of dry granular media

3.1.1 A dry assembly of grains as an effective elastic medium

Granular media are made up with macroscopic grains that interact through repulsive and frictional forces. Grain elasticity can sometimes be neglected, for example when studying rapid granular flows [1, 2], leading to considering grains as perfectly rigid bodies. However, studying propagation of elastic waves through the grain contacts requires the grains to be considered as elastic: an external stress applied to one particular grain induces its elastic deformation (figure 3.1) [3].



(a) (b)

Figure 3.1: (a) Deformed elastic grains under stress. (b) If the strain is not too large, contact between two grains can be modeled by a string-mass system. Figure extracted from [3].

Several models exist to account for the relationship between stress and strain between two bodies in contact [4, 5]. Among them, the Hertz model [6], which applies to the case of two frictionless spheres brought into contact under loading, is the simplest and most common one. Theoretically, the contact area between two spheres is a point where the

pressure should be infinite, which would cause immediate yielding of surfaces. However, a small contact area is being created through elastic deformation, thereby limiting the stress considerably. The overlap δ_0 between the two spheres in contact under a force F_0 (without friction) is then predicted to scale as $\delta_0 = F_0^{2/3}$ (figure 3.2).

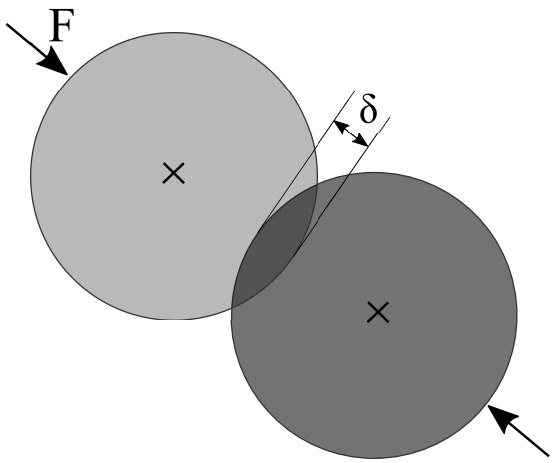


Figure 3.2: Schematic representation of deformed elastic grains under stress. The overlap between grains δ_0 is represented in terms of the applied external force, without friction.

A step further is the Hertz-Mindlin model [7] which adds the tangential (friction) force between the two spheres. One can also consider more complete models to include the grain surface roughness, liquid films trapped at the grain surface or losses due to visco-elastic dissipation inside grains.

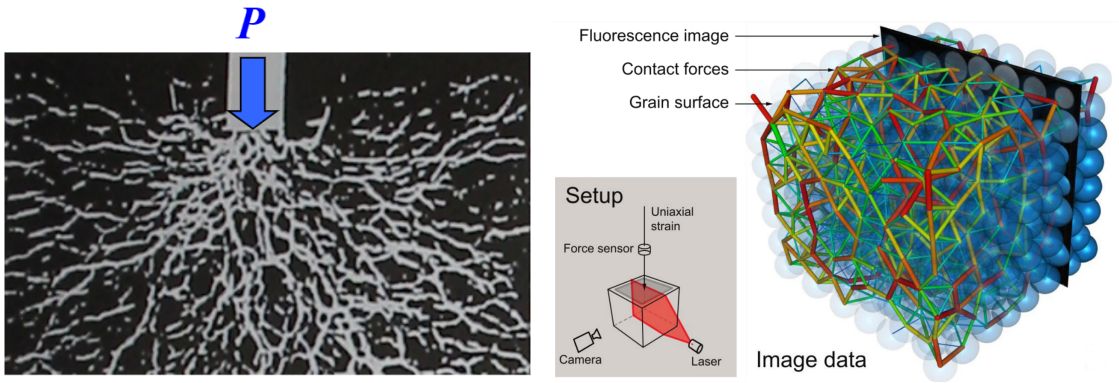
Starting from the contact forces at the grain level, effective medium approaches [3, 7] can be developed to describe a granular medium as a continuum elastic medium with effective macroscopic elastic moduli. The drawback of such an approach is that it does not account for properties that also influence wave propagation, disorder and the existence of a contact force network, that we discuss in the next two paragraphs.

3.1.2 A dry assembly of grains as a disordered medium

Various kinds of disorder coexist within a granular packing. Starting from a regular (crystalline) packing of identical nodes (corresponding to solid beads), disorder can be introduced in different ways. One can first modify the physical property at the nodes (e.g., the bead mass without changing its size or position). Another possibility would be to change the links between nodes (i.e., by changing the grain surface roughness or by wetting some contacts to tune the interaction between beads). A third possibility, perhaps the most natural one, would be to introduce a topological disorder by placing the nodes randomly in space (i.e., by mixing the set of beads to achieve a random packing). In general, a granular medium includes these three types of disorder.

3.1.3 The importance of the contact force network

A granular packing confined by an external stress exhibits an internal force distribution which is extremely heterogeneous. It was first visualized in 1957 by Dantu in a small packing of glass cylinders (pyrex) under stress [8]. Thanks to the photoelastic effect (i.e., modification of the optical index of the cylinders as a function of the applied stress), Dantu was able to obtain an image of the forces within the medium: grains under high stress appear bright while grains under small stress appear dark (see figure 3.3). Note however that the light intensity is not proportional to the stress but to its square, which consequently amplifies the contrast between small and large stress compared to the actual values. Such a contact force network was also recently observed in 3D as illustrated in figure 3.3 [9].



(a) (b)

Figure 3.3: (a) Image of the force chains in a small packing of glass cylinders (pyrex) under stress. Thanks to the photoelastic effect, grains under high stress appear bright while grains under small stress appear dark. Figure extracted from [8]. (b) Probe of the force network in a 3D granular medium. Figure extracted from [9].

The forces appear to be distributed according to a complex heterogeneous network of "forces chains". Remarkably, this contact force network appears to be disordered even in the case of a regular packing [10, 11], which can be explained by the grain roughness that induces frictional forces. In other words, the disorder of the contact force network does not only depend on the topological disorder of the granular packing, but also on the disorder at the level of contacts due to friction (disorder of the "links").

Makse, Johnson and Schwartz showed that the distribution of the inter-grain forces highly depends on the external stress [12] as shown in figure 3.4. For weak external stress, the force distribution is exponentially decreasing as soon as the forces are higher than the average force. For higher stress, the distribution decreases faster and becomes Gaussian, a signature that the forces in the network tend towards homogenisation. In other words, at low stress, the network is made up of a few chains supporting a significant part of the stress (a sort of "skeleton" of the bead packing), and of many chains withstanding a small fraction of the stress; at high stress, the network is much more homogeneous and

is made up of chains, all supporting almost the same stress. It should also be noted that this behaviour depends little on the nature of the packing (regular or not) and the grain properties (roughness, shape, etc.).

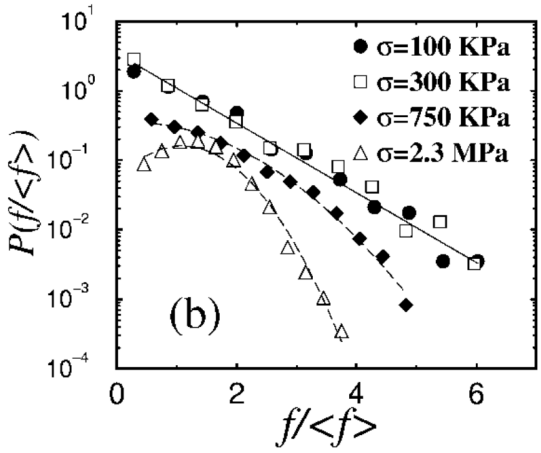


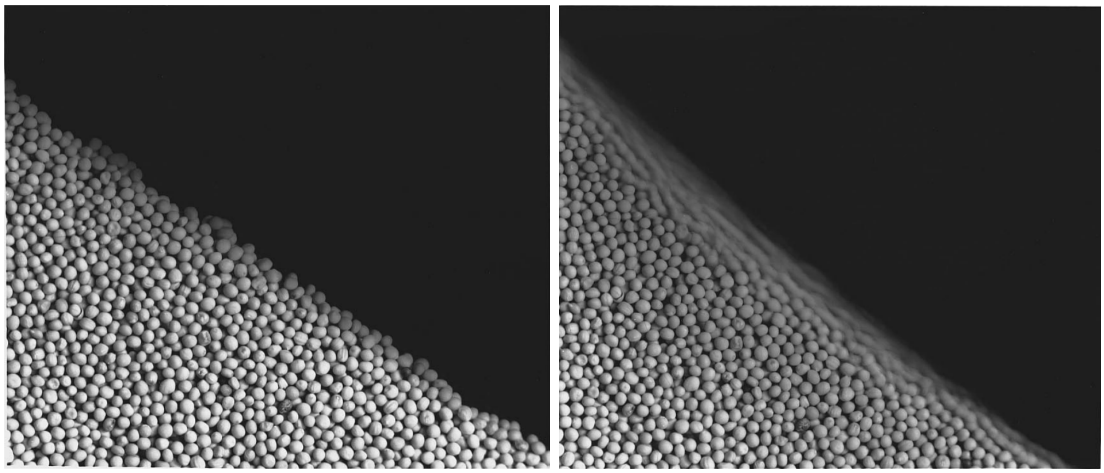
Figure 3.4: Inter-grain force distribution in terms of the external applied pressure. Figure extracted from [12].

In real experiments as the ones reported later in this chapter, friction always plays a role (more or less important according to the grain roughness) in determining the stability of a confined granular packing. Indeed, the friction between two grains is a threshold force: the contact is stable only if the tangential force remains below a certain value fixed by the normal force and the friction coefficient. Therefore, in a frictional bead packing, there is an indetermination in the contact force network which is history-dependent and in particular depends on the preparation protocol of the granular sample. The equilibrium is said to be hyperstatic and several contact force networks may correspond to a given topological packing [13].

In the absence of friction (as can be achieved in simulations), the forces between the grains are normal to the contacts and, for a given geometrical configuration of the grains, the force balance equations admit only one solution: the system is then said to be "isostatic". The network equilibrium is then fragile in the sense that the tiny external force may break the overall equilibrium. Friction, by revealing "alternative" solutions, gives the medium some resistance (shear rigidity) even at zero confinement stress [14].

3.1.4 Jamming and unjamming

Another peculiarity of granular media is that they can behave as both a solid or a liquid. For example, a granular bed at rest, as depicted in figure 3.5, behaves like a solid. If the granular bed is tilted above some critical angle, grains on the surface start to flow as a liquid, which is referred to as an unjamming transition: the grains initially jammed in a metastable state have received sufficient external energy to move to another state by flowing.



(a) (b)

Figure 3.5: (a) A granular medium tilted to an angle lower than the avalanche angle. At this position the system can be considered to be in a blocked (solid) state. (b) The same medium after the slope has been increased to create an avalanche. The system changed to an unblocked (liquid) state, where the flow occurs only along the grains located on the surface; the grains deeper within the pile do not move. Figure extracted from [1].

The jamming transition is a general paradigm for understanding how complex fluids such as foams, emulsions and granular materials develop rigidity, and share similarities with the glassy transition: when the density of randomly packed particles is increased to a certain critical value, the viscosity increases dramatically and the flow is arrested. Liu and Nagel proposed to unify the description of the different routes to the jamming transition [15] in a phase diagram involving temperature, stress, and the inverse of density (figure 3.6). It reveals a closed central zone, representing the blocked states (a solid glass in the plane of zero stress or a stable granular packing in the zero temperature plane) and an outside zone, limited by a "jamming surface", where the system is released: the glass becomes liquid when the temperature is too high or the granular bed flows when the stress is too great.

In a glassy medium, the transition from a jammed to an unjammed state is activated by thermal energy, whereas in a granular medium the transition is initiated by an external mechanical driving. Indeed, the thermal energy k_BT is negligible compared to the energy required to move a grain (as soon as its size is typically larger than 1μm), meaning that a granular medium is athermal [1]. Thus the grain assembly cannot spontaneously explore the various metastable states in the vicinity of its current state, contrary to the case of a liquid or a gas. It is the external solicitation that allows the granular medium to explore different states, playing the role of an effective temperature.

A granular medium is fragile in the sense that a small perturbation can induce the

[1]The kinetic energy of a $100-\mu$m diameter glass bead moving at a typical speed of 1 cm/s would correspond to a temperature of 10^9K !

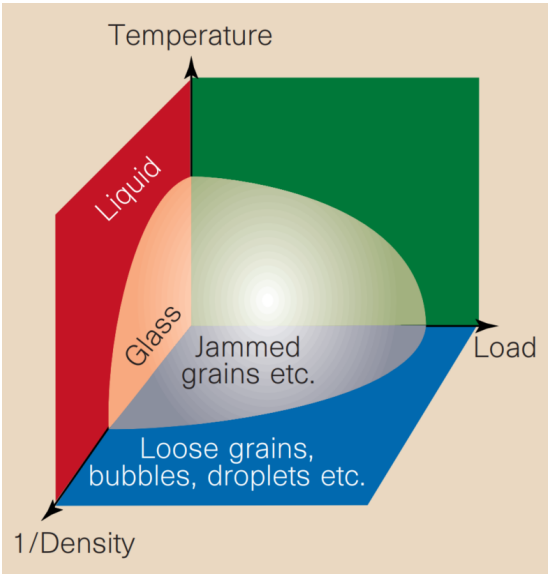


Figure 3.6: A possible phase diagram for jamming/unjamming transition. The variables involved in the diagram are the temperature, the applied stress and the inverse of the density. A surface within the figure delimits the region of blocking, near the origin. Figure extracted from [15].

unjamming transition as argued by [16, 17] taking the example of a linear chain of grains. If the contacts between the grains are point-like, the chain cannot withstand any force (no matter how small) non-collinear with its axis without undergoing plastic deformation (see figure 3.7). If the grains can deform, the collinearity constraint can be lifted and a non-longitudinal force can be applied without the chain breaking.

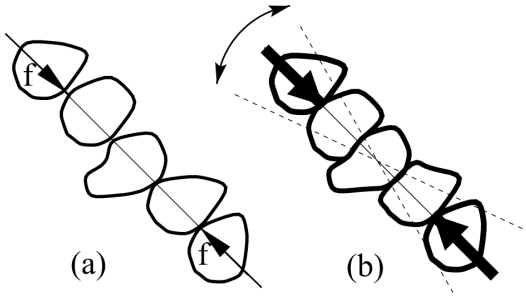


Figure 3.7: (a) In the hard-particle case (for any shape), a force chain can only support a longitudinal compression. (b) In the elastic-particle case, small transverse contributions of the applied force are allowed. Figure extracted from [16].

We can therefore imagine that rearrangements of a granular medium can be triggered with small stress fluctuations. In the context of geophysics, this led to the idea that some earthquakes could be triggered by incoming waves from regional foreshocks and far-distant large earthquakes. In both cases, the instability (a fault zone containing granular gouge) exists before the "triggering" event, so that shaking on a fault plane is a question of activating an instability. In other words, the view has emerged that a dynamic perturbation of sheared gouge material can induce a phase transition corresponding to a failure or a

fault slip. One important issue is to determine when a fault has reached its near-rupture state to be sensitive to a remote solicitation. In the same manner, certain landslides or rockfalls can originate from vibrations linked to local seismic activity. Small-scale laboratory experiments have been suggested as a possible strategy to shed new lights on these issues. In that context, time-reversal focusing appears as an appropriate method for remotely creating controlled perturbations (in time, position and amplitude) as we will show in the following. But before, let us discuss the ways elastic waves propagate in a granular material.

3.1.5 Elastic wave propagation and scattering

Due to the stress-induced elasticity, granular media can withstand the propagation of elastic waves.

The simplest example of wave propagation in a granular medium is the propagation of a compressional wave along a 1D chain of identical and perfectly elastic spheres under compression [18–21]. Following the Hertz contact theory, the overlap δ_0 between two elastic spheres (radius a) subjected to a static force F_0 is given by [19]:

$$\delta_0 = \frac{2}{a^{1/3}} \left[\frac{3\left(1-\mu^2\right)}{4E} F_0 \right]^{2/3} \tag{3.1}$$

where E is the Young's modulus of the sphere's material and μ the Poisson's ratio. This expression remains valid even when the force F_0 (and hence δ_0) are both time dependent, as long as the motion time scales remain much greater than the time needed by a longitudinal acoustic wave to travel across a bead diameter. This condition will be satisfied in our own experiments.

For an overlap δ_0 small compared to the sphere radius a, the granular chain can be modelled as a spring-mass system, leading to a set of coupled non-linear equations

$$\frac{d^2 u_n}{dt^2} = \frac{2E\sqrt{a/2}}{3m\left(1-\mu^2\right)} \left\{ \left[\delta_0 - (u_n - u_{n-1})\right]^{3/2} - \left[\delta_0 - (u_{n+1} - u_n)\right]^{3/2} \right\} \tag{3.2}$$

where m is the mass of a sphere and u_n is the displacement of the n-th sphere from its equilibrium position. Here the non-linearity only comes from the geometric non-linearity of the Hertz contact (i.e. the stiffness of the contact between the grains depends on the contact surface and thus on the overlap). Note that this model does not take into account any possible dissipation (at grains contacts or inside grains).

In the approximation of small amplitudes, equation (3.2) can be linearized to deduce the dispersion relation between the angular frequency, ω, and the wave vector $q = 2\pi/\lambda$ (where λ is the wavelength):

$$\omega(q) = 2\sqrt{\frac{k}{m}}\,|\sin(qa)| \tag{3.3}$$

where k is the stiffness of the contact defined by

$$k = (\partial\delta_0/\partial F_0)^{-1} = (3/4)\,(aF_0)^{1/3}\left[4E/3\left(1-\mu^2\right)\right]^{2/3}.$$

From equation (3.3), we can show that the wave phase velocity c increases with the confining pressure as $P^{1/6}$, as also predicted by the effective medium theory in a 3D granular medium [22, 23]. As to the wave group velocity $d\omega/dk$, it is found to vanish when the wavelength is four times the bead radius, which corresponds to a cutoff frequency $\frac{1}{\pi}\sqrt{\frac{k}{m}}$. Finally, it should be pointed out that elastic waves can no longer propagate when the confining pressure goes to zero (the contact stiffness vanishes), but nonlinear solitary waves can still propagate [19].

The case of 2D or 3D granular packings is much more complex. This complexity is not only due to the topological disorder, but also to the heterogeneity of the contact network [11], even for regular packings of grains as already mentioned. For these reasons, there is no analytical model that can accurately describe the propagation of elastic waves in real granular media. However, it can be modelled using an effective media approach, which provides average elastic properties on a macroscopic scale. This approach allows the wave speed of low-frequency waves to be predicted to a good approximation [11, 24].

But as shown in 1999 by Jia et al. [25], there are generally two types of elastic waves propagating in a confined granular medium (figure 3.8): a ballistic coherent wave (E) and a multiple scattered wave (S). The ballistic wave corresponds to the self-averaged wave that propagates ballistically in the effective medium and that is insensitive to the precise position of the grains: it sees a homogeneous effective medium. The multiple scattered wave results from the multiple scattering of the wave by the heterogeneous force chain network and is extremely sensitive to small perturbations of the granular packing.

The relative amplitudes of these two contributions to the signal strongly depend on the ratio of the bead size to the detector size. The transducer averages the transmitted wave field on its surface, leading to a cancellation of the incoherent multiple scattered wave. Thus, when the transducer is large relative to the grain size (figure 3.8a), many grains are in contact with the transducer and the coherent wave dominates over the multiple scattered wave. On the other hand, when the transducer size is comparable to that of the beads (figure 3.8c), the amplitude of the coherent wave is of the same order as that of the multiple scattered wave. In the intermediate case (figure 3.8b), the recorded transmitted wave is a mixture between the two types of wave.

In the frequency domain, we see that the coherent wave (E) has much lower frequencies than the multiple scattered wave (S), meaning that it corresponds to large wavelength and "sees" a homogeneous medium. In contrast, the multiple scattered wave corresponds

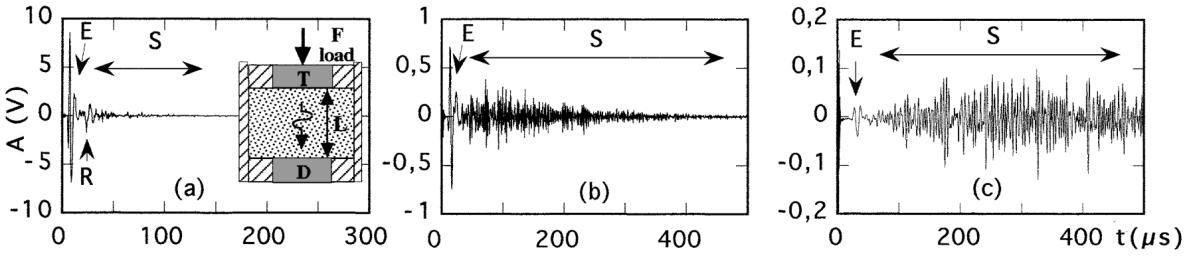


Figure 3.8: Elastic waves transmitted in a granular medium under an external load and influence of the ratio of the beads size to the detector size. A brief ultrasonic pulse is emitted by a piezoelectric transducer T and received, after propagation in the medium, by a transducer D with a diameter of 12 mm. The latter then takes an average of the elastic field at its surface adding the coherent and incoherent wave of the multiple scattered wave. (a) When the beads are much smaller (diameter $0.2-0.3$ mm) than the transducer, the coherent part dominates the transmitted wave. (b) For bead size between $0.4-0.8$ mm, the amplitudes of the two waves are comparable. (c) For larger bead size (diameter 1.5 mm), the multiple scattered wave dominates. Figure extracted from [25].

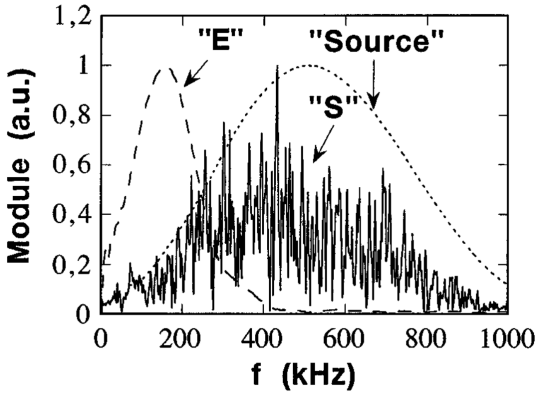


Figure 3.9: Spectrum of the elastic wave transmitted in a granular medium under an external load. The coherent wave (E) corresponds to lower frequencies than the multiple scattered wave (S). Figure extracted from [25].

to shorter wavelengths (comparable to the grain size) and thus undergoes a large number of scattering events through the contacts between grains.

The role of these two waves in a time reversal experiment in a granular medium will be carefully studied in the next part. But before that, based on a proof-of-principle experiment, we will show the ability of time-reversal to remotely trigger mechanical perturbations.

3.2 Proof-of-principle experiment: time-reversal in a chaotic cavity

Before attempting to use time-reversal focusing to create a localized perturbation in a granular medium, we designed a proof-of-concept experiment in which one takes advantage of multiple reverberation in a chaotic cavity to focus high amplitude ultrasound on a bead

one wants to remove from a trap.

3.2.1 Time-reversal in a 2D chaotic cavity

The basics of time-reversal have been briefly introduced in the second chapter. Time-reversal of elastic waves in a chaotic cavity has been first experimentally studied by C. Draeger and M. Fink [26, 27]. The experimental setup is sketched in figure 3.10. The cavity consists of a silicon wafer with a typical diameter of 100mm and a thickness of 525μm. The cut off segment gives the cavity a chaotic shape. The material was chosen for its weak dissipation. Elastic waves are injected at A from a point-like source and received by a point-like receiver of the same type at point B. Both the source and the receiver consist of an aluminum cone fixed to a 1MHz-central-frequency transverse transducer.

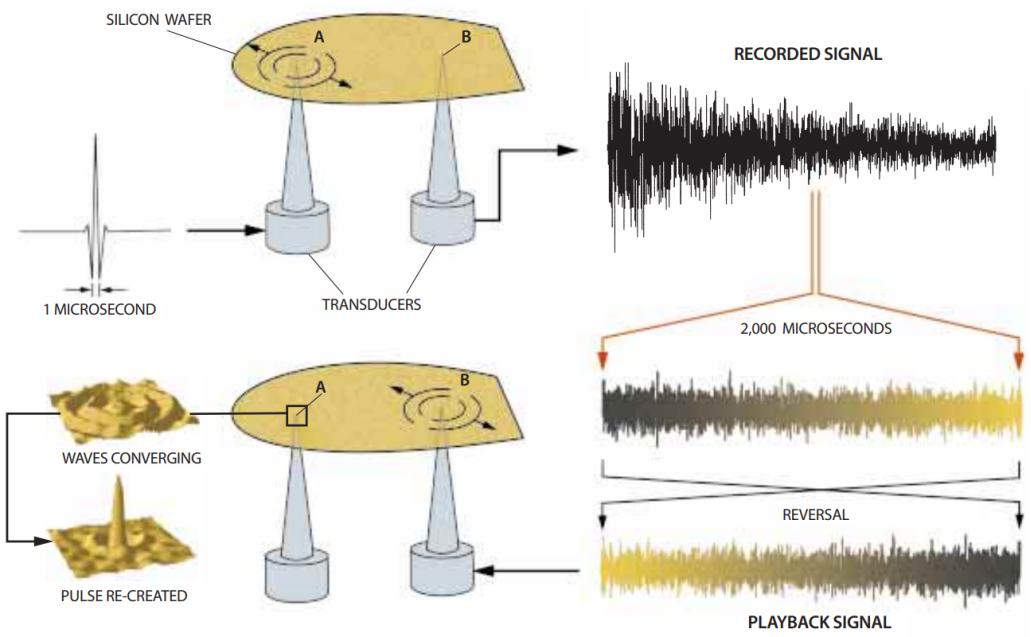


Figure 3.10: Mono-element time-reversal of elastic waves in a D-shaped silicon cavity. Two point-like emitter-receivers are located at points A and B (upper left). In step one, a brief pulse is emitted from A and a much longer signal is recorded at B after multiple bouncings off the perfectly reflective borders (upper right). A time window selected in the received signal is flipped in time and re-emitted from B (lower right), resulting in a wave focused at point A (lower left). Figure extracted from [27].

In the first step, the transducer at point A emits a brief ultrasound pulse (duration $\sim 1\mu$s) that excites SH and Lamb modes A_0 and S_0 in the silicon plate. The transducer located at B records a very long signal which corresponds to the multiple wave reverberation from the plate edge. In the second step, a time window is selected in the signal recorded at B, flipped in time and re-emitted from the same transducer; in A, one can then observe a sharp peak surrounded by temporal sidelobes, of which the level depends on the length of the time-reversal window (time compression). An optical interferometer can be used to analyse the spatial distribution of the wavefield around the refocusing time.

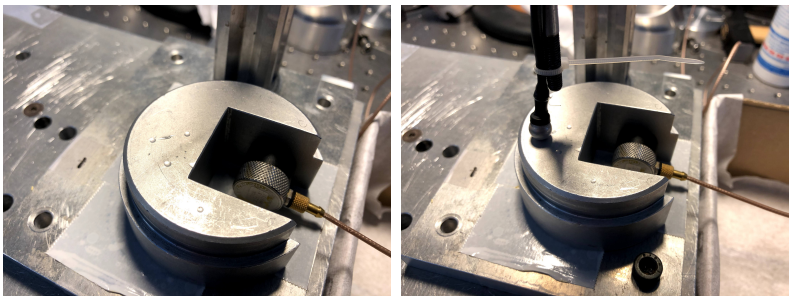
We observe that the time-reversed wave field converges toward the origin point A from all directions to produce a circular spot. This seminal work showed that a single-element time-reversal mirror can be enough to focus back a replica of the initial pulse at the source location. In an open homogeneous medium, spatial focusing would be limited by the time-reversal mirror aperture. Here the ergodicity of the cavity (coupled to a low absorption and perfectly reflective boundaries) ensures that all rays emerging from the source pass through the position of the receiver (within one wavelength). Thus if one records a long enough signal (longer than the Heisenberg time of the cavity), one has all the information to focus isotropically as if we had a full time-reversal cavity [28]. Furthermore, if the time-reversed signal is reemitted with the same amplitude as that of the initial pulse, a strong amplification can be obtained due to the time compression effect; the amplification factor is governed by the time-reversed window length. A stronger amplification can be obtained by digitising the time-reversed signal on one bit or by amplifying the time-reversed signal before reemission. The application of this "bazooka effect" to lithotripsy has been studied by G. Montaldo et al. [29].

3.2.2 Time-reversal experiment in a 3D chaotic cavity

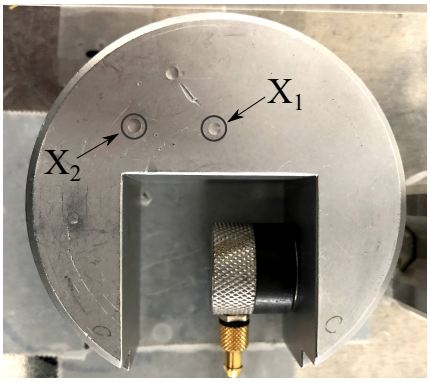
Inspired by the experiment described in the previous paragraph, we have designed a proof-of-concept experiment to investigate time-reversal focusing as a method to induce controlled rearrangements. For this purpose, an irregular steel block was used as a 3D chaotic cavity as shown in figure 3.11.a. A spherical transducer (diameter 8mm and resonance frequency of about 235kHz) is placed on the top surface of the cavity and used to excite the medium (figure 3.11.b). The single-element TRM consists of a flat transducer (Olympus Centrascan Panametrics C106-RM of central frequency 2.25MHz) attached to the side face of the cavity with some medical ultrasound coupling gel in order to ensure a good impedance matching (figure 3.11.c).

Two holes, labeled as X_1 and X_2, were made on the top of the cavity surface where the spherical transducer could be placed (figure 3.11c). The chosen working frequency is 300kHz, corresponding to a wavelength of approximately 19mm for longitudinal waves in stainless steel. It means that the distance between X_1 and X_2, i.e., about 12mm, is of the same order of the wavelength $\lambda \simeq 19$mm.

We first place the spherical transducer at point X_1 and excite it with a 3-cycle sine wave at a central frequency of 300kHz (duration $\sim 1\mu$s). The TRM then records the transmitted signal for almost 5ms (see figure 3.12). Then, a time-window starting from the first arrival ($t = 0$s) until the signal amplitude stops decreasing ($t = 3$ms) is selected, time-reversed and re-emitted. The time recompression measured with the spherical transducer at X_1 is shown in figure 3.13. The experiment is then repeated with the spherical source placed at X_2 keeping the TRM at the exact same position. The obtained time compression is



(a) (b)



(c)

Figure 3.11: (a) and (b) Chaotic block and the experimental arrangement of the transducers used during the experiments. (c) Positions in the surface of the block where the sourced is located for time-reversal measurements. The relative distance between X_1 and X_2 is approximately 12mm.

shown in figure 3.14.

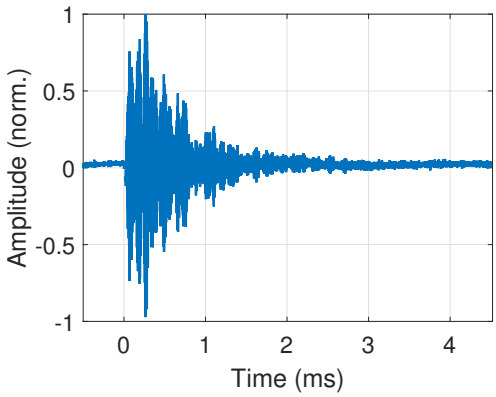
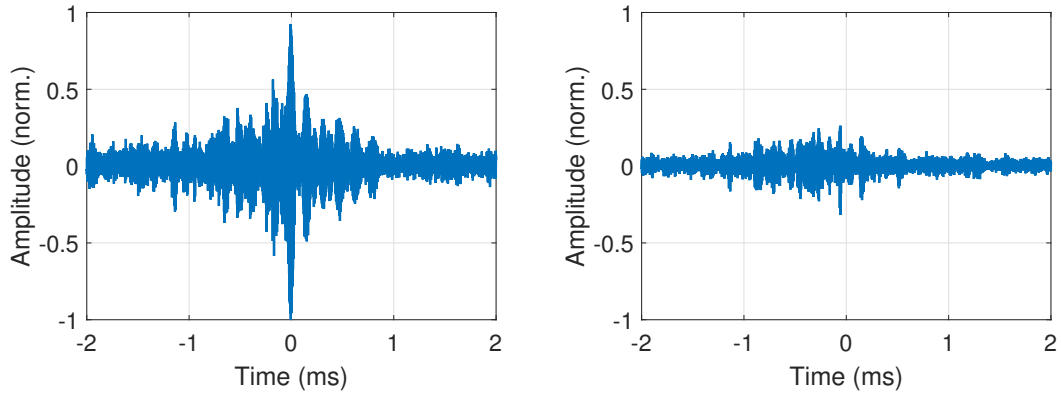


Figure 3.12: Example of a signal recorded by the TRM. The source signal was a 3-cycle sine wave transmitted from the spherical transducer located at X_1.

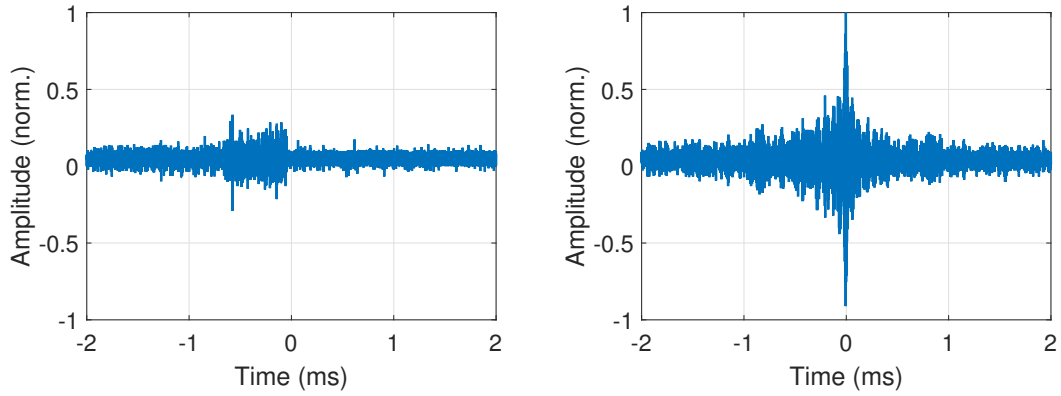
In both cases, the amplitude at the focal point is about four times higher than that measured one wavelength further, meaning that the wave is well focused in space.

To maximize the time-reversed amplitude at the focal point, we repeat the experiment following the same procedure, except that the signals are now digitized on a single bit as in the experiment by Derode et al. [30]. In other words, the only information that is



(a) X_1 (b) X_2

Figure 3.13: Time-reversed wave measured for an initial source position at X_1. (a) Time recompression observed at X_1. (b) Signal received at X_2.



(a) X_1 (b) X_2

Figure 3.14: Time-reversed wave measured when the initial source was placed at position X_2. (a) Signal observed at X_1. (b) Time recompression received at X_2.

recorded and time reversed is the sign of the reverberant signal, meaning that the signal sent back in the cavity is two valued. This procedure allows for compensating the time decay of the coda wave. Figure 3.15 shows the comparison between the time compressions obtained respectively with conventional and 1-bit time-reversal. The amplitude of the peak obtained in the 1-bit time-reversal experiment is approximately 4 times higher than in the conventional experiment. The drawback is a loss of symmetry in the sidelobes, which is not really an issue since the amplitude difference between the peak and its higher lobe is still a factor two.

3.2.3 Bead dropping by time-reversal focusing

As a proof-of-concept, we now test the ability of time-reversal focusing to trigger an "avalanche" of a single grain. As in avalanche experiments, an inclined plane of adjustable

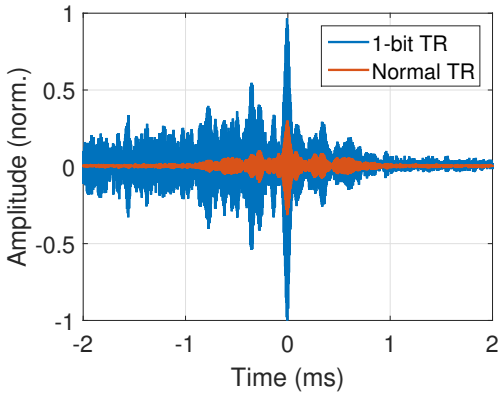


Figure 3.15: Comparison between recompression signals obtained by conventional and 1-bit time-reversal. The 1-bit recompression peak is approximately 4 times higher than the one obtained by conventional time-reversal.

angle is used [31] on which the chaotic cavity is placed. The goal is to determine the thresholds in both angle and amplitude to trigger the drop of a 1.5-mm diameter bead.



(a) (b)

Figure 3.16: (a) Positioning of the bead to study the thresholds for the angle and the amplitude necessary to drop the bead. (b) Positioning of two beads to test the high-amplitude time-reversal focusing.

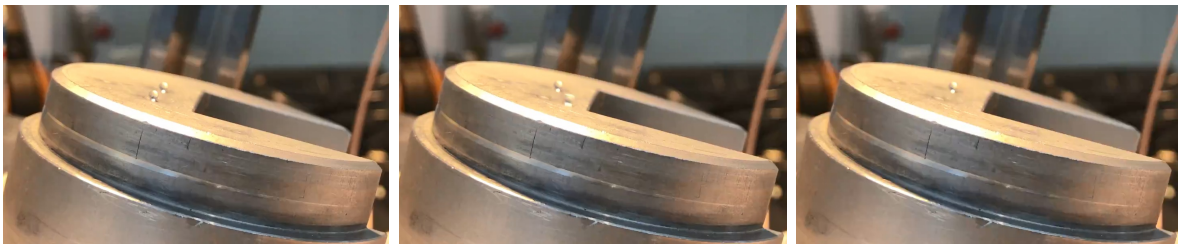
To determine the avalanche angle, the grain is placed at the position X_1 (respectively X_2), the plane being initially horizontal $\theta = 0°$. Then, the angle of the plane is slowly increased manually until the grain falls. The procedure is repeated several times. The critical angle measured for both positions X_1 and X_2 is similar and equal to about $\theta_c \simeq 15°$, within an effective range of 0.5°.

To determine the amplitude threshold, the plane is inclined at an initial angle of approximately 13.5° and the bead is placed at either X_1 or X_2. Then, the angle is slowly increased manually to approximately 14.5° and the 1-bit time-reversed signal is emitted at increasing amplitudes until the bead is dropped. Again, the procedure is repeated several times to confirm the threshold value.

For an angle of 14.5°, the threshold amplitudes obtained for the 1-bit time-reversed coda signal A_{X_1} and A_{X_2} (before a +50dB amplification) are

$$\begin{cases} A_{X_1} = 0.5\mathrm{V_{pp}} \\ A_{X_2} = 1.0\mathrm{V_{pp}} \end{cases} \tag{3.4}$$

After this calibration step, a last experiment is performed in which two beads are placed on the inclined plane, one at X_1 and the other at X_2 (figure 3.16.a). Since the threshold A_{X_1} is lower than A_{X_2}, dropping the bead at X_2 without dropping the one at X_1 would make explicit the possibility of creating a localized controlled perturbation.



(a) (b) (c)

Figure 3.17: Three frames showing the bead drop. Two beads are respectively placed at X_1 and X_2. In (b) and (c) it can be seen how the bead at X_2 falls, while the bead at X_1 remains in its equilibrium position. This implies that the dropping is triggered by time-reversal focusing and not due to the propagation of high amplitude acoustic waves through the system.

Figure 3.17 illustrates how the avalanche is triggered at X_2 while the bead X_1 remains trapped. Repeating several times the experiment under the same conditions gives a success rate of about 70%.

Of course, one can expect the situation to be more complicated in the case of a granular medium. The question is to know whether one can find a range of parameters for which a localized perturbation can be remotely induced without rearranging the whole medium.

3.3 Time-reversal experiment through a dry granular medium

It has been only recently shown that time-reversal focusing is possible through a dry granular medium [32], which was not so obvious. Such an experiment was indeed raising two challenging issues. First, as already mentioned, no wave equation can be written at the scale of the force chains. This issue is related to a fundamental question: at which scale is the continuum elasticity applicable in a contact network? Secondly, one may wonder whether time-reversal invariance can hold in a fragile granular medium where the propagating wave acts as a probe but also as a pump, leading to the acoustic fluidization

of the jammed media via the rearrangement of the contact network. And, as shown in [32], the fact is that a source of too high amplitude can indeed induce a rearrangement of the contact force network (without visible grain motion) in the forward propagation step such that the time-reversal focusing breaks down. Since our goal is to use TR focusing to induce controlled rearrangements localized in the source region, the first step consists in finding the parameters for which TR focusing is possible without any rearrangement.

3.3.1 Experimental setup

Photographs of the setup are shown in figure 3.18 while a schematic representation is shown in figure 3.19.

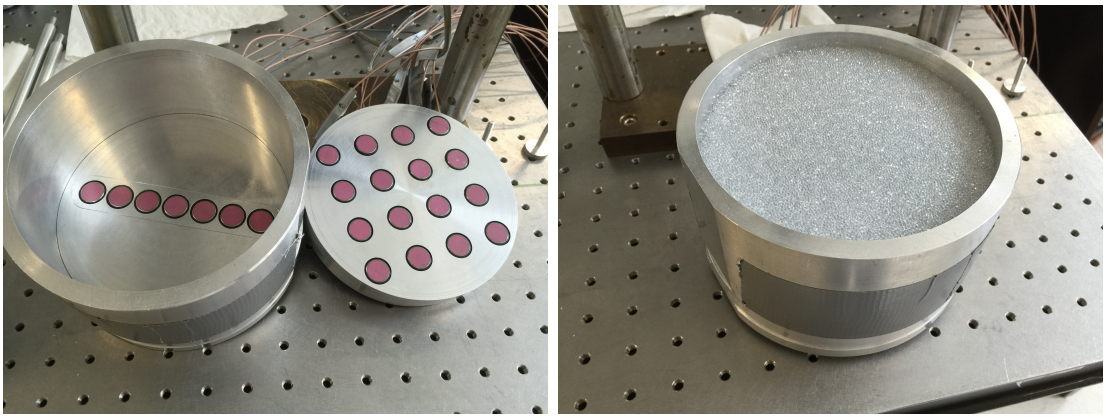
The experimental setup consists of a cylindrical steel container with diameter 15cm and height 6cm (see figure 3.18a). At the bottom of the container is located a linear array of seven circular identical piezoelectric transducers spaced 19mm apart. Each transducer (Olympus Centrascan Panametrics C106-RM) has a diameter of $D = 15$mm and a central frequency of 2.25MHz. On the lid of the container is a square-like array consisting of sixteen transducers of the same type spaced 30mm apart. It will be referred to as the Time-Reversal Mirror (TRM). Throughout this chapter, the container is filled with a set of 1.5-mm diameter monodisperse glass beads (3.18b). The effects of the bead size on the propagation of acoustic waves were previously discussed [25, 33]; our choice lends to several contacts between the grains and the sensors.

For the experiments presented in this chapter only compression transducers were used. The effects of the source polarisation (compressional or shear transducer) were discussed in previous works [32]. The experiments were performed using a one single-element TRM. In appendix A an analisys of time-reversal with multi-element TRM is discussed.

The source signal is generated from Matlab running on a standard PC, transmitted to an arbitrary function generator, amplified by 50dB and finally transmitted to the central piezoelectric transducer of the linear array (figure 3.20). The transmitted wavefield is recorded by one of the piezoelectric transducers in the TRM, amplified, analogically filtered (Panametrics Pulser-Receiver model 5058PR) and sent to a scope (LeCroy WaveJet 334A Oscilloscope) interfaced under Matlab.

3.3.2 Sample preparation protocol

As previously stated, our main objective is to use time-reversal focusing to remotely create localized rearrangements in dry granular media. Such media are known to be extremely fragile. Small mechanical perturbations can drive the contact force network from one metastable configuration to another one. Furthermore, once loaded under an external stress (figure 3.18), the sample starts evolving to a more stable state, a process which is referred to as “aging”. We thus have to define a preparation protocol for ensuring that



(a) (b)



(c)

Figure 3.18: Photographs of the steel container used in acoustic time-reversal experiments. (a) Photograph of the empty container and the two transducer arrays. On the one hand, a linear array of seven piezoelectric transducers is located at the bottom of the cell along a diameter. On the other hand, the 4×4 square-like array of sixteen transducers is located in the container top cover . (b) Photograph of the container filled with the granular medium. The beads shown here are $d = 1.5$mm in diameter. (c) Experimental setup. The steel container is put under an external stress, applied with a manual press and measured by a force sensor.

the rearrangements we will observe will be only those triggered by TR. In other words, the sample must remain stationary at the scale of a time-reversal experiment. To that goal, we have first to characterize the aging process.

Figure 3.21 compares acoustic signals transmitted in a dry granular medium under an external stress at two different times. After 30 seconds, signals are slightly shifted due to the aging of the sample. In figure 3.21.b signals do not look the same anymore with a delay of 10 minutes: the granular medium has evolved to another more stable configuration.

To characterize the aging of the sample, we use low amplitude acoustic wave trans-

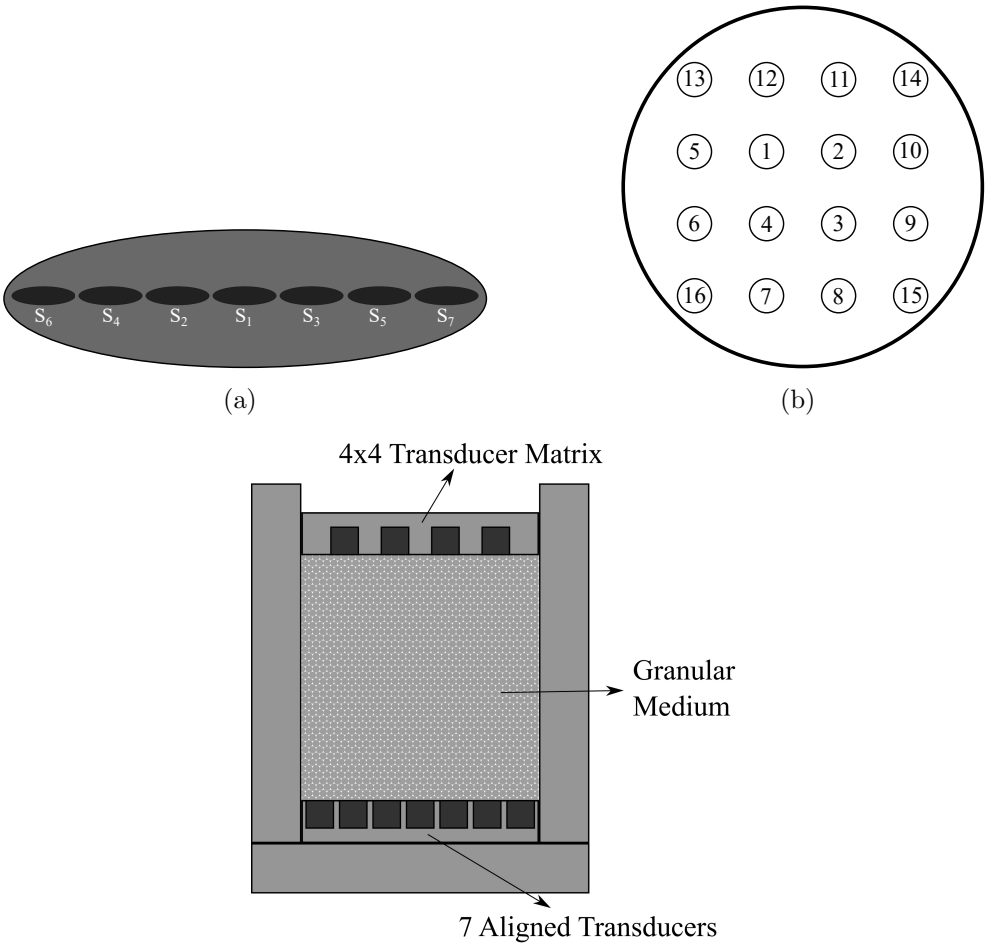


Figure 3.19: (a) Bottom of the cell where is located a linear array of seven piezoelectric transducers numbered from S_1 to S_7. S_1 denotes the source. (b) Top cover of the container where the sixteen transducers of the array are numbered. (c) Schematic representation of the whole setup.

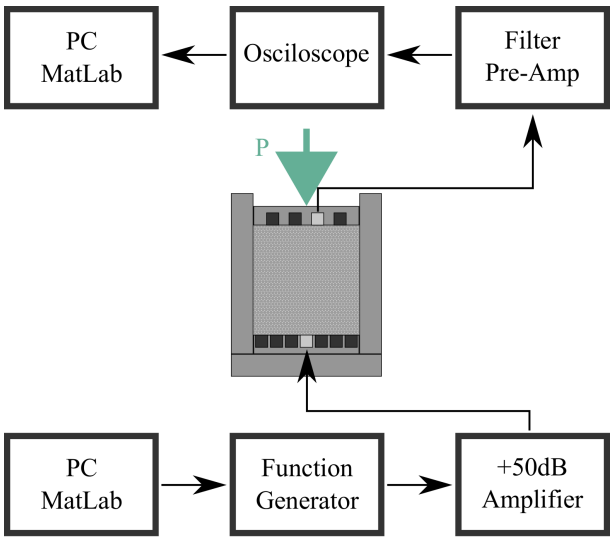
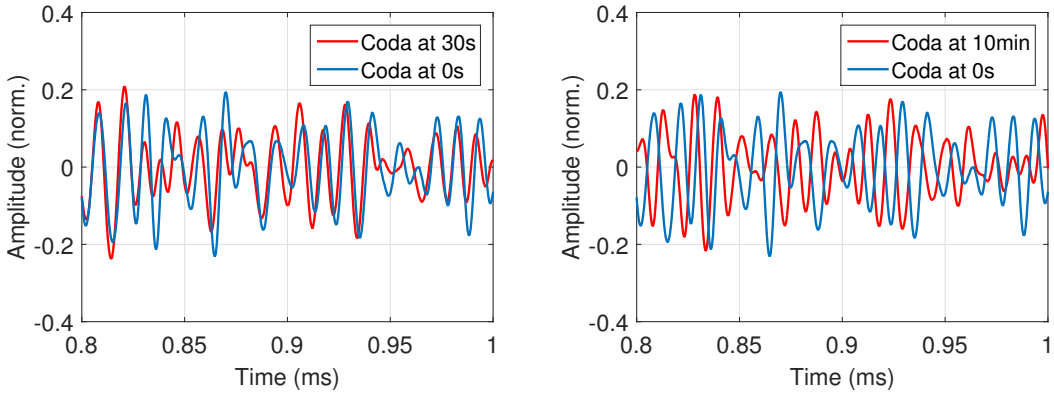


Figure 3.20: Experimental configuration for the emission/reception experiment.



(a) (b)

Figure 3.21: Zooms in the late part of the acoustic Coda wave for a granular medium composed of 1.5-mm glass beads under an external pressure of 85kPa. (a) Comparison between signals measured 30 seconds apart. In this case, the correlation coefficient is about 0.90. (b) Comparison between acoustic transmissions measured 10 minutes apart. The correlation coefficient went down to approximately 0.40.

mission. The external applied pressure is 85kPa. Using a piezoelectric transducer at the bottom of the container, S_1, a 2-cycle sine wave with central frequency 80kHz and amplitude $3V_{pp}$ is emitted. Another transducer, D_1, located on the container top cover records the signal transmitted through the granular medium. This procedure is repeated over time intervals $\Delta t = 30$s. To determine the aging time of the system, we calculate the correlation coefficient between acoustic signatures of the granular medium taken at two instants. On the one hand, the correlation coefficient between a signal received at time t_j and the baseline signal received at time $t = 0$, $C_{0,j}$, allows us to quantify the global change undergone by the system over time. On the other hand, the coefficient between two consecutive signals $C_{j,j+1}$ is calculated, which quantifies the instantaneous change of the system in a time interval Δt. Finally, the coefficient between signals with a delay equal to 5 minutes $C_{j,j+10}$ is also calculated, which will allow us to determine the waiting time (j) necessary for the system to be considered stationary during a typical measurement.

Let $\phi_i(t)$ be the acoustic wave transmitted at time t_i and and $\phi_j(t)$ that transmitted at time t_j. Their cross-correlation $\Psi_{i,j}$ is given by:

$$\Psi_{i,j}(\tau) = \int \phi_i(t)\,\phi_j(t+\tau)\,dt. \tag{3.5}$$

Then, we can define the correlation coefficients $C_{i,j}$ mentioned above as

$$\begin{cases} C_{0,j} = \frac{\max_\tau[\Psi_{0,j}(\tau)]}{\sqrt{\Psi_{0,0}(0)\Psi_{j,j}(0)}} \\ C_{j,j+1} = \frac{\max_\tau[\Psi_{j,j+1}(\tau)]}{\sqrt{\Psi_{j,j}(0)\Psi_{j+1,j+1}(0)}} \\ C_{j,j+10} = \frac{\max_\tau[\Psi_{j,j+10}(\tau)]}{\sqrt{\Psi_{j,j}(0)\Psi_{j+10,j+10}(0)}} \end{cases} . \tag{3.6}$$

To study the effect of how the external load is applied on the sample, we compare correlation coefficients obtained for three different cases: the load is applied directly on the granular medium; the load is applied, removed and applied again (referred to as "loading-unloading"); the loading-unloading is carried out three times. For this purpose, we studied the evolution of the system during 20 minutes, measuring the transmitted signal every 30 seconds.

Figure 3.22 shows the results obtained for the three considered cases. In the absence of "loading-unloading", the sample evolves rapidly in the first few minutes after its preparation (figure 3.22(a)). The correlation coefficient $C_{0,j}$ decreases to about 0.30 in just a few seconds, meaning that the system has transited to complete different configurations. Likewise, the dynamic correlation coefficient $C_{j,j+1}$ oscillates between 0.20 and 0.60 during the first 5 minutes, indicating the presence of abrupt changes in the system. It rises to values higher than 0.80 after 5 minutes, to finally reach values close to unity in the last 10 minutes. Finally, the coefficient $C_{j,j+10}$ oscillates around values between 0.20 and 0.40 in the first 10 minutes and, after 15 minutes, tends to stabilize around 0.80.

Figures 3.22(b) and 3.22(c) show that adding a "loading-unloading" procedure smoothes the evolution of the system. The correlation coefficient $C_{0,j}$ decreases slower to values in the order of 0.30, while the coefficient $C_{j,j+1}$ rises to values above 0.95 from the beginning of the measurement, showing that instantaneous changes in the system are negligible. Finally $C_{j,j+10}$ reaches values greater than 0.90 in the first 10 minutes of waiting while it reached a value of 0.20 without the "loading-unloading" procedure, indicating a much faster stabilization of the granular medium. After 15 minutes of waiting, the correlation coefficient $C_{j,j+10}$ even reaches values greater than 0.95.

We can thus conclude that the introduction of at least one "loading-unloading" is necessary to fasten and increase the stabilization of the system. Using as a criterion a correlation coefficient $C_{j,j+10}$ greater than 0.95, we conclude that waiting 15 minutes after the preparation of the system is enough to perform experiments on a stationary granular medium.

Finally, the sample preparation will consist in three steps. In the first step, one pour the beads and mixed them with a fork. Then the granular medium is subject to a "loading-

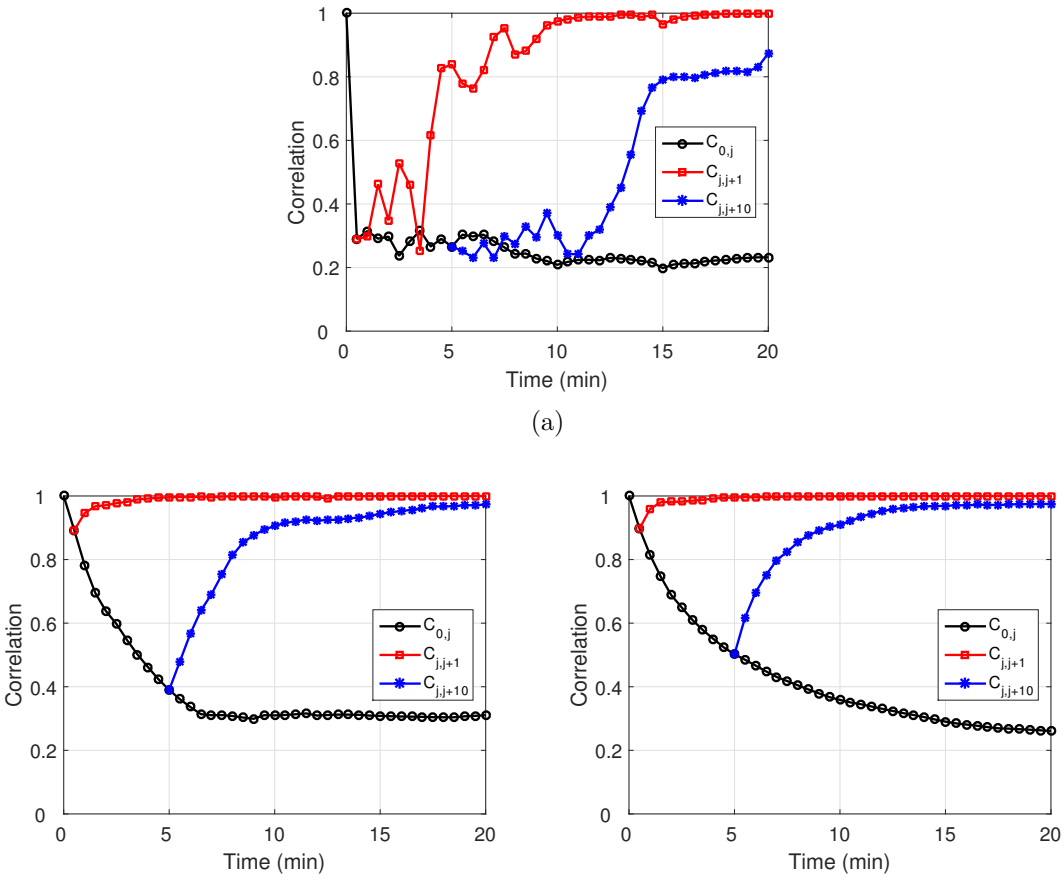


Figure 3.22: Follow-up of the aging effect for a granular medium composed of 1.5mm-diam beads under an external pressure of 85kPa. The curve in black quantifies the evolution of the sample compared to its initial state. $C_{0,j}$; the correlation coefficient $C_{j,j+1}$ is plotted in red and the correlation coefficient $C_{j,j+10}$ between signals transmitted 5 minutes apart is plotted in blue (a) Aging of a sample prepared without "loading-unloading". The correlation coefficient $C_{j,j+10}$ reaches a value of 0.80 after 15 minutes. (b) Aging with one loading-unloading cycle. In this case, the correlation coefficient $C_{j,j+10}$ reaches a value of 0.95 after 15 minutes. (c) Aging of a sample for three "loading-unloading" cycles. The correlation coefficient $C_{j,j+10}$ reaches a value of 0.97 after 15 minutes.

unloading" procedure and put under stress. Finally, we wait 15 minutes to ensure that the granular medium is stationary at the scale of a time-reversal experiment.

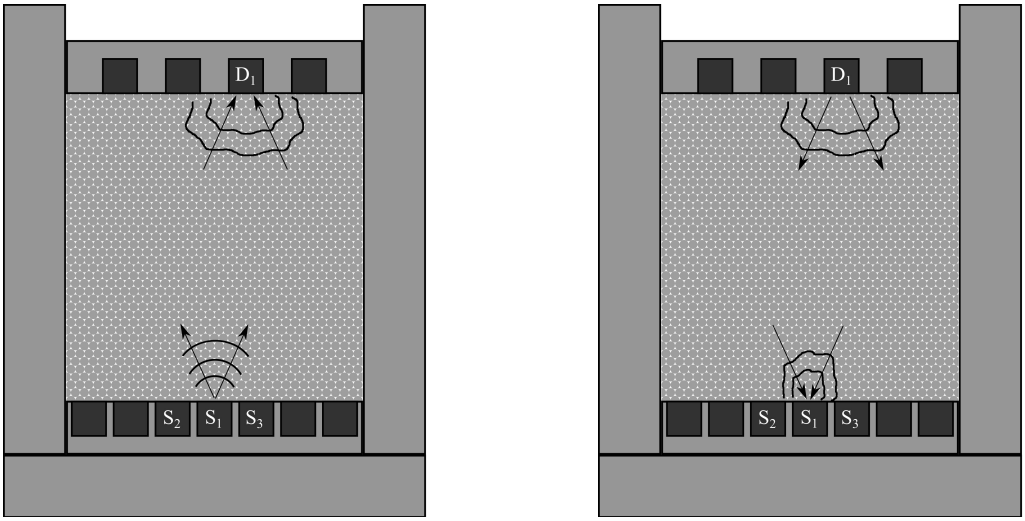
3.3.3 Single-channel time-reversal experiment

3.3.3.1 Contributions of the ballistic wave and the Coda wave

As previously reminded, an expected fundamental feature in the transmission of acoustic waves through a multiple scattering granular medium is the distinction between the ballistic coherent wave and the multiple scattered wave [25]. The former can be understood as the remnant of the incident wave. It sees the granular medium as an effective medium since it corresponds to wavelengths larger than the scatterer size. On the other hand, the

multiple scattered wave, also called coda wave [34], results from scattering off the contact network.

In our experiments, the granular medium is confined under an external pressure of 85kPa applied with a manual stress as presented in figure 3.18. Figures 3.23a and 3.23b illustrate the two steps of a typical single-channel time reversal experiment. A 2-cycle sine wave with a central frequency of 50kHz is emitted from S_1. The transmitted waveform as recorded by D_1 is shown in blue in figure 3.24a and its corresponding spectrum in 3.24b. The coherent wave (respectively the coda wave) can be extracted by a low pass filter (respectively a high pass filter) with a cutoff frequency of 30kHz.



(a) (b)

Figure 3.23: Scheme illustrating the two phases of a time-reversal experiment. (a) Phase one. A transducer excites the medium with a short signal, the response of the system is recorded by a transducer located on the other side of the medium. (b) The transmitted signal is time-reversed and re-emitted into the system, focusing back at the initial source.

In a first experiment, only the ballistic wave is time-reversed. In the second step, S_1, S_2 and S_3 are connected to the multi-channel electronics and the time-reversed wave is sent back from D_1. As shown in figure 3.25a, b and c, no spatial focusing is observed as would also be expected in a purely homogeneous medium. In that case diffraction theory indeed predicts that the focal spot size scales as $\lambda\frac{F}{D}$ with F the focal distance and D the TRM aperture. Thus TR focusing is impossible with a one-single channel TRM (i.e., a TRM without any aperture). On the contrary, we expect spatial focusing to occur when the coda wave is time-reversed and backpropagated as argued in [35] in the case of a multiple scattering medium made of cylindrical rods randomly placed in a homogeneous medium (water). Provided that the medium is sufficiently disordered and that the bandwidth is large enough, the coda wave contains all the necessary information to focus back to the source from all directions [36]. The same result was more recently demonstrated in a granular medium [32]. This is what we retrieve in our experiments as

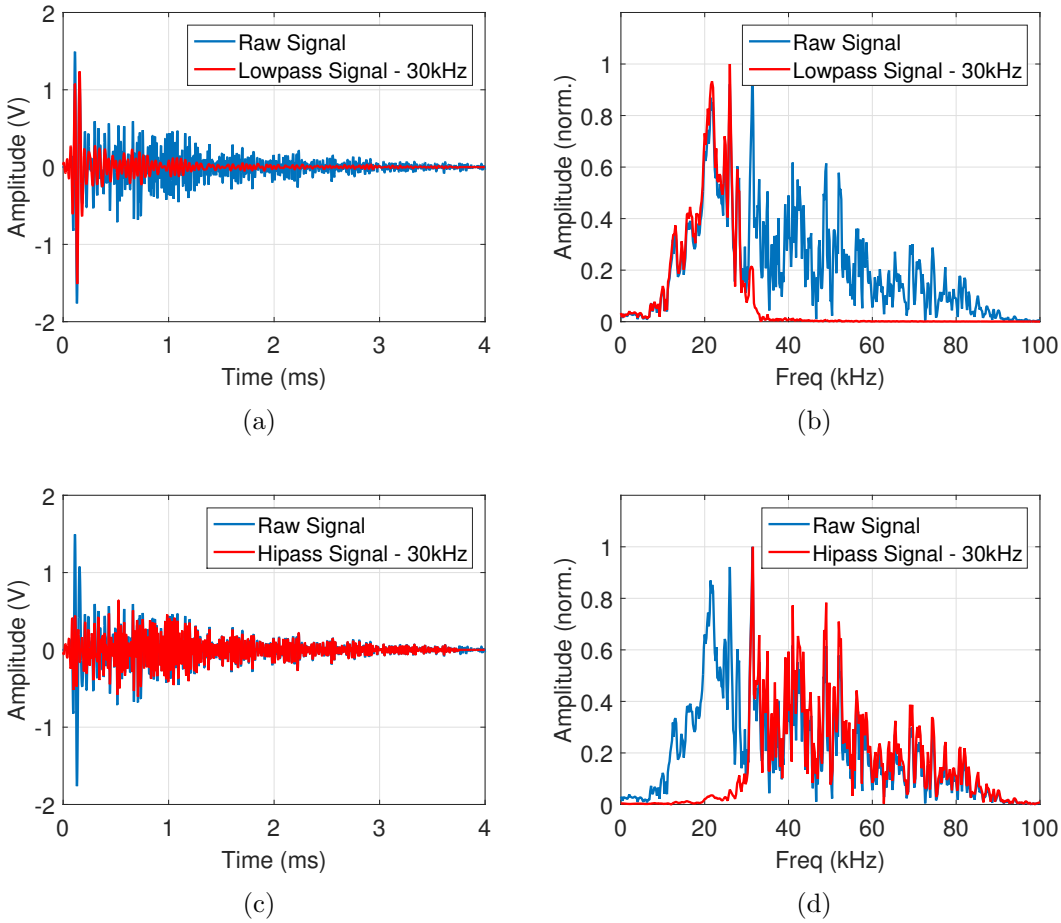


Figure 3.24: Separation of the coherent wave and the coda wave contributions. (a) Comparison between the transmitted acoustic waveform (in blue) and the waveform obtained after applying a low-pass filter with a cutoff frequency of 30kHz (in red). The filtered signal isolates the coherent wave. (b) Comparison of the spectra of the transmitted signal (in blue) and of the low-frequency filtered signal (in red). (c) Comparison between the transmitted acoustic waveform and the waveform obtained after applying a high-pass filter with a cutoff frequency of 30kHz. The filtered signal isolates the coda wave. (d) Comparison of the spectra of the transmitted signal (in blue) and of the high-frequency filtered signal.

shown in figures 3.25 d, e and f.

3.3.3.2 Verification of the stability of the granular medium

For the following experiments, we will use a higher central frequency, 80kHz instead of 50kHz, to reinforce the contribution of the Coda wave. Since our goal is to remotely trigger rearrangements by focusing a high-amplitude ultrasound wave at some desired location, we have first to check that the medium is rearranged neither during the forward nor during the backward propagation step of the TR process.

Before performing the TR experiment, we first follow the preparation protocol previously described and then record the reference signatures of the granular medium as illustrated in figure 3.26 on both the TRM and the source sides. On the source side, we

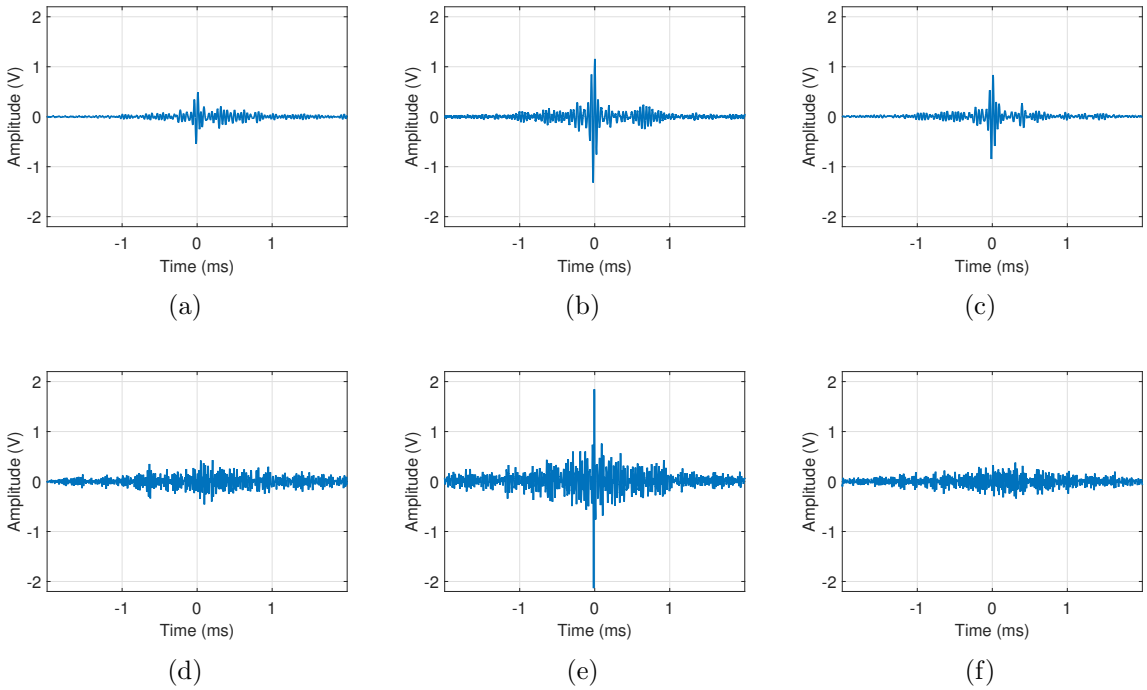


Figure 3.25: Recompression signals recorded at the source location S1 and at the closest neighbouring detectors S2 and S3 after time-reversal and back-propagation of respectively the low-frequency coherent wave (a, b, c) and the high-frequency multiply scattered waves (d, e, f). The coda wave is focused back at the initial source position while the coherent wave is not.

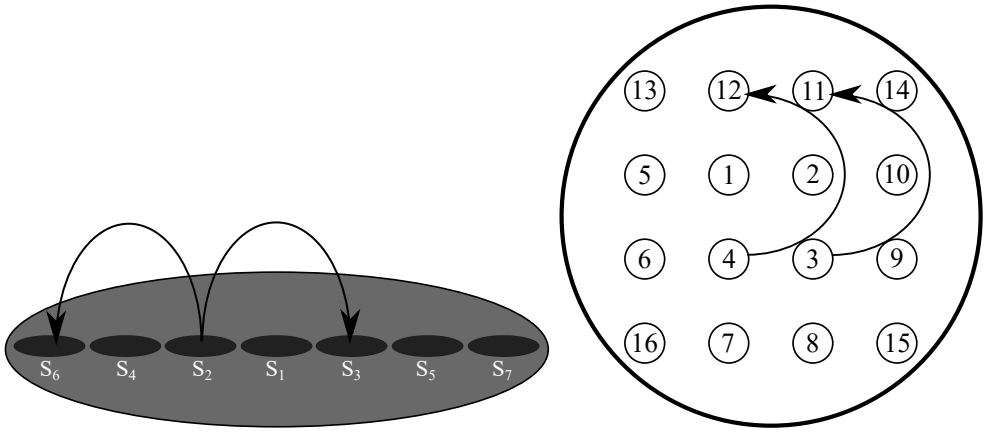


Figure 3.26: Recording of characteristic signatures of the granular medium (a) At the bottom of the cell, transducer S_2 sends an acoustic pulse and the transmitted signal is measured at S_3 and S_6. (b) In the TRM side, the acoustic signatures are measured from D_4 to D_{12} and from D_3 to D_{11}

measure the signals $h_{2,3}(t)$ and $h_{2,6}(t)$ at respectively S_3 and S_6 when S_2 sends out a 2-cycle sine wave with a central frequency of 80kHz. On the TRM side, we measure the signals $g_{3,11}(t)$ and $g_{4,12}(t)$ at respectively D_{11} and D_{12} when respectively D_3 and D_4 send out a 2-cycle sine wave with a central frequency of 80kHz.

Then the TR is performed. The source S_1 thus excites the medium with a short acoustic signal consisting of a 2-cycle sinus with a central frequency 80kHz and an amplitude of $3V_{pp}$. The transmitted wave is recorded at receiver D_1 and computationally filtered with a high-pass cutoff frequency of 45kHz to remove the ballistic contribution of the transmitted wave. It is then time-reversed and re-emitted back into the sample with the same amplitude as the source ($3V_{pp}$). Finally the time-reversal field is measured by the source transducer and its neighbours to analyse both temporal recompression and spatial focusing. A nice compression is obtained at the source as shown in figure 3.27 as well as a nice focusing as shown in figure 3.28.

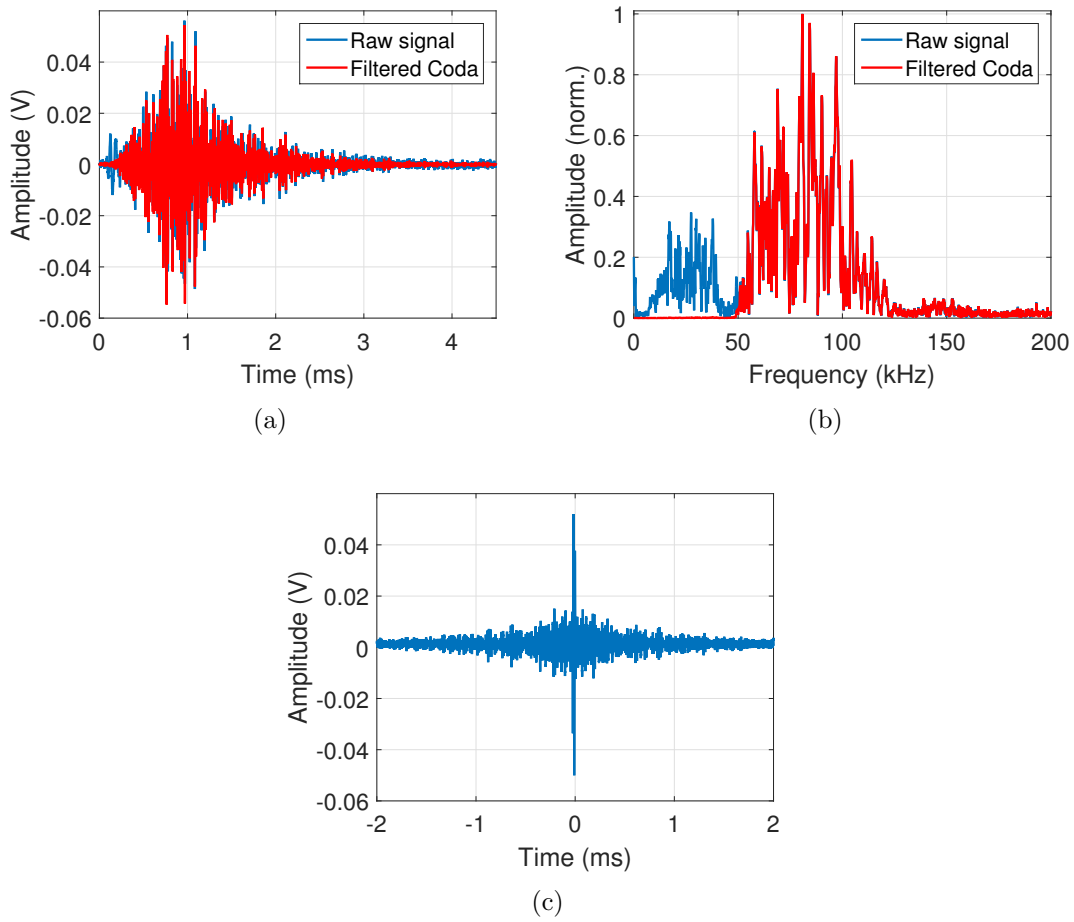
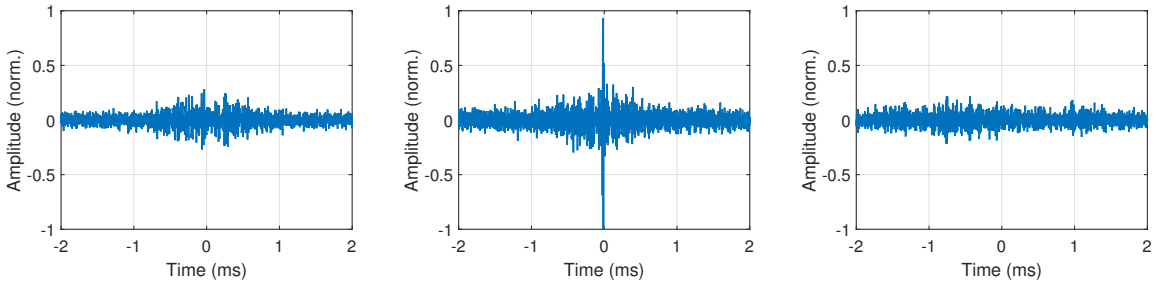


Figure 3.27: One-channel time-reversal. Both initial excitation and re-emission were emitted with an amplitude of $3V_{pp}$. The transmitted signal was high-pass filtered with a 45kHz cutoff frequency to remove its ballistic contribution. (a) Comparison between the transmitted acoustic waveform and the resulting waveform after filtering. (b) Comparison of the spectra of the transmitted signal and the filtered signal (c) Time recompression measured at S_1 in phase two of the time-reversal.

The new signatures of the granular medium $h'_{2,3}(t)$, $h'_{2,6}(t)$, $g'_{3,11}(t)$ and $g'_{4,12}(t)$ are then recorded and four correlation functions are calculated:



(a) (b) (c)

Figure 3.28: One-channel time-reversal experiment. Time-reversed signals measured at S_2 (a) S_1 (b) and S_3 (c).

$$\begin{cases} f_S(\tau) = \int h_{2,3}(t) h'_{2,3}(t+\tau) dt \\ f_S^N(\tau) = \int h_{2,6}(t) h'_{2,6}(t+\tau) dt \\ f_{TRM}(\tau) = \int g_{3,11}(t) g'_{3,11}(t+\tau) dt \\ f_{TRM}^N(\tau) = \int h_{4,12}(t) h'_{4,12}(t+\tau) dt \end{cases} \tag{3.7}$$

By repeating 10 times the whole process we inferred the following average correlation coefficients:

$$\begin{cases} C_{Source} = \langle \frac{\max_\tau f_S(\tau)}{\sqrt{\int h_{2,3}^2(t) dt}} \rangle \\ C_{Source}^N = \langle \frac{\max_\tau f_S^N(\tau)}{\sqrt{\int h_{2,6}^2(t) dt}} \rangle \end{cases} \tag{3.8}$$

$$\begin{cases} C_{TRM} = \langle \frac{\max_\tau f_{TRM}(\tau)}{\sqrt{\int g_{3,11}^2(t) dt}} \rangle \\ C_{TRM}^N = \langle \frac{\max_\tau f_{TRM}^N(\tau)}{\sqrt{\int g_{4,12}^2(t) dt}} \rangle \end{cases} \tag{3.9}$$

where the brackets denotes an average over 10 experiments.

These four correlations coefficients allow to quantify the modifications that occurred respectively around the source, in the neighbourhood of the source, around the single-channel TRM and in the neighbourhood of the single-channel TRM. We find:

$$\begin{cases} C_{Source} = 0.94 \pm 0.01 \\ C_{Source}^N = 0.96 \pm 0.01 \end{cases}$$

$$\begin{cases} C_{TRM} = 0.97 \pm 0.02 \\ C_{TRM}^N = 0.97 \pm 0.01 \end{cases}$$

These values confirm that the medium has not been rearranged during the TR experiment.

3.4 Time-reversal as a means for triggering rearrangement

In the previous sections, we have established a preparation protocol that ensures the stationarity of the granular medium and have checked that TR focusing can be achieved without any rearrangement of the medium. As done in section 3.2, the idea is now to play on the amplitude of the reemitted time-reversed wave to increase the amplitude focused at the source and induce localized rearrangements.

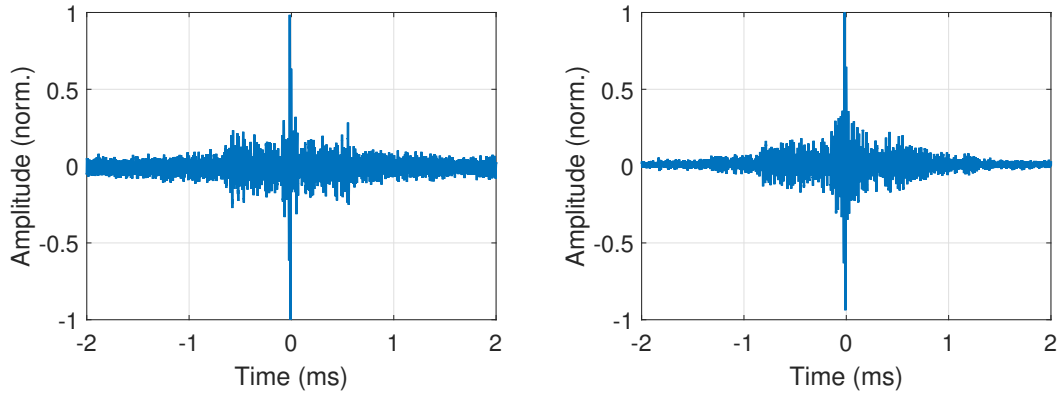
3.4.1 Single-channel time reversal

The experimental setup is the same as the one presented in figure 3.20. We use the preparation protocol presented in section 3.3.2. First, the beads are placed in the container. Then, a single loading-unloading cycle is performed to stabilize the granular medium and an external load of 85kPa is applied. Finally, we wait for 15*minutes* and record the acoustic signatures in the different regions of interest. The medium is then excited with the source S_1 emitting a 2-cycle sine wave at a central frequency of 80kHz and with amplitude $A_1 = 3\mathrm{V_{pp}}$. The transmitted waveform is recorded with the detector D_1, and flipped in time. In a second step, the time-reversed wave is re-emitted with an amplitude A_2 and the time recompression is recorded by S_1 as well as the new acoustic signatures to calculate the correlation coefficients. The second step is repeated for amplitudes ranging from $A_2 = 3\mathrm{V_{pp}}$ to $A_2 = 150\mathrm{V_{pp}}$. The corresponding time-reversed peaks are shown in figure 3.29.

For each amplitude, measurements were repeated for 10 different configurations of the granular sample.

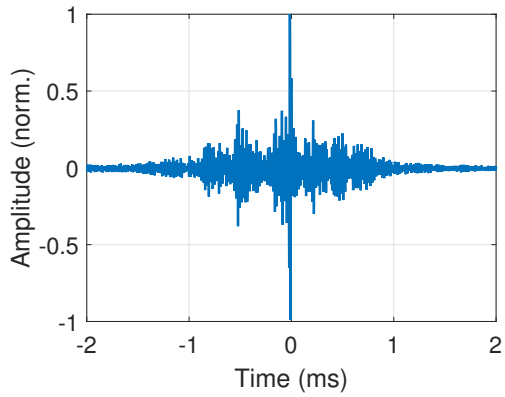
As shown in figure 3.30.a, the peak amplitude starts increasing linearly with the re-emitted amplitude, but decreases beyond $A_2 = 30\mathrm{V_{pp}}$. This is confirmed in figure 3.30.b where we see that the signal-to-sidelobes ratio decreases as soon as the re-emitted amplitude increases (even in the range of amplitudes where the TR peak still increases). These results highlight the difficulty to find a parameter window where rearrangements can be induced around the source. As already seen in section 3.3.3, no rearrangements occur at $A_2 = 3\mathrm{V_{pp}}$. But as soon as A_2 is increased, the medium undergoes rearrangements during backpropagation of the time-reversed wave such the focusing is degraded.

Figure 3.30c shows that for amplitudes up to $\sim 25\mathrm{V_{pp}}$, the granular remains approximately stationary on both the source and the TRM sides, with correlation coefficients higher than 0.90. For higher amplitudes, the correlation coefficient in the TRM side

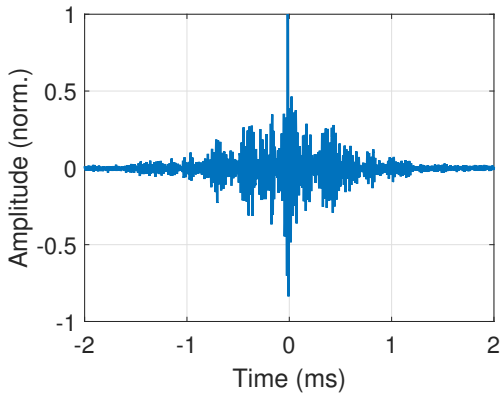


(a) $A_2 = 3\mathrm{V_{pp}}$

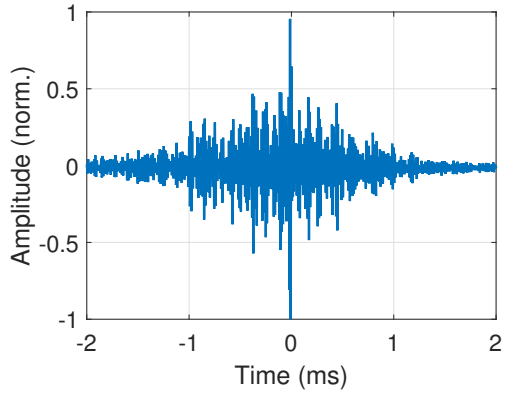
(b) $A_2 = 10\mathrm{V_{pp}}$



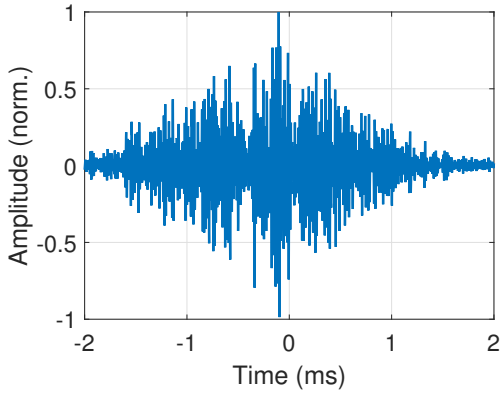
(c) $A_2 = 20\mathrm{V_{pp}}$



(d) $A_2 = 30\mathrm{V_{pp}}$



(e) $A_2 = 50\mathrm{V_{pp}}$



(f) $A_2 = 100\mathrm{V_{pp}}$

Figure 3.29: Time recompressions measured at S_1 for several amplitudes A_2 in phase two of the time reversal experiment. As A_2 increases, the quality of the time recompression decreases, resulting in a peak which is not distinguishable any more for values greater than $100\mathrm{V_{pp}}$.

rapidly decreases as A_2 increases. For amplitudes above $100\mathrm{V_{pp}}$, C_{TRM}, reaches a constant value of about 0.20 and the coefficient at the source, C_{Source} starts to decrease. Finally, for an amplitude of $150\mathrm{V_{pp}}$, both coefficients reach a value of 0.20, showing that the whole medium is rearranged. There is just a small window in amplitude ($A_2 = 30\mathrm{V_{pp}}$) where $C_{Source} < C_{TRM}$, i.e., where rearrangements occur mainly around the source.

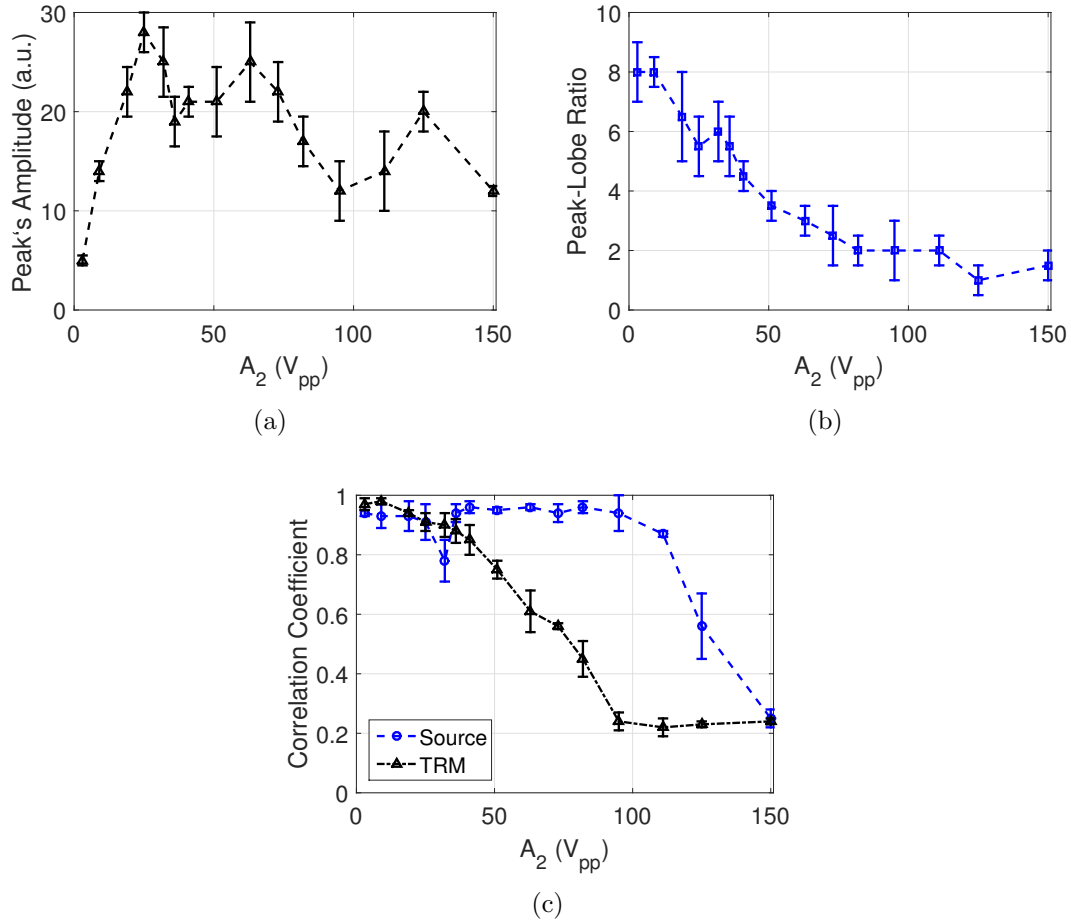


Figure 3.30: Recompression peak amplitude, peak-to-lobe ratio and correlation coefficients against the amplitude A_2 in the step two of time-reversal. (a) Evolution of the time recompression peak as a function of amplitude A_2. The peak amplitude grows as A_2 does, until it reaches a superior limit value and starts its decrease. (b) Dependence of the peak-to-lobe ratio of the time recompression with the amplitude A_2. (c) Correlation coefficient between acoustic signatures in the source and TRM region. For the value $A_2 = 30\mathrm{V_{pp}}$ we have a local minimum where the decorrelation is larger in the source than in the TRM.

3.5 Discussion and conclusions

Throughout this chapter, the time-reversal of acoustic waves through a confined granular medium was studied. The analysis and characterization of the system was carried out, from the linear regime using low amplitudes up to the generation of rearrangements by focusing high-amplitude waves by time-reversal.

In order to verify the feasibility of remotely generating rearrangements, we first mounted a bead dropping experiment using a chaotic cavity (section 3.2). Using a stationary and stable system, regardless of the amplitude of the acoustic waves propagating through it (as verified), allows to analyze how time-reversal focusing at high amplitudes focuses enough energy to drop a 1.5mm-diameter glass bead. In particular, the focusing of the acoustic waves was verified since the desired bead is the one that is dropped and

not the neighboring bead where the waves should not be focused. This also implies that the dropping is due to spatial focusing and not only to the propagation of high amplitude acoustic waves.

Special emphasis was then put on the preparation protocol of the system, obtaining a method that allows the reproducibility of experimental results. The analysis of the correlation coefficient between transmitted waves through the system (from S_1 to D_1) allowed establishing stability criteria for the granular system. By studying the correlation between transmissions 5 minutes apart, it was possible to accurately define both the preparation and the waiting time for each configuration of disorder. It is important to take into account the time involved in the measurement through the granular medium. Thanks to the study and characterization of the aging, it was concluded that the minimum waiting time to carry out an experiment is 15 minutes. This is in addition to the time of the experiment itself and the time required for the corresponding data processing. In an estimated way, a single clutter configuration involves at least 30 minutes. This means that obtaining a single experimental value (with its corresponding mean value and errorbar) involves at least 5 hours of work (solely dedicated to it). The commitment involved in ensuring the stability of the granular medium and the reproducibility of the experimental results is payed in the time invested in each of the measurements performed.

Once the working protocol was established, the linear regime of the granular medium was studied, performing the time-reversal of low amplitude acoustic waves. Verification of the linear regime are phenomena such as the dependence of the time recompression with the number of channels used in the TRM; or the measurement of quantities such as the correlation coefficients between acoustic signatures C_{Source} and C_{TRM}. In turn, the optimization of the spatial focusing was verified by using the coda signal, removing the ballistic contribution of the transmitted wave.

The transition from the linear regime to the instability of the system was studied by gradually increasing the amplitude of the TRM in phase two of the time-reversal experiment. To work with the granular medium it is necessary to have a gradual increase in amplitude due to its fragility. In order to have almost total control of the parameters involved in the experiment, we worked with a single-element TRM. Values were obtained for the correlation coefficients C_{Source} and C_{TRM}, the peak of the time recompression and the peak-to-lobe ratio as a function of the TRM amplitude A_2.

The behavior of the same parameters was studied for the case of a multi-channel TRM in appendix A.

From this chapter we conclude that the determination of a preparation protocol guarantees the reproducibility of the experiments. For the time-reversal experiment at low amplitudes, we were able to verify that the confined granular medium presents a behavior characteristic of a multiple scattering medium. In spite of the great compromise between stability and fragility, it was possible to find a window of parameters where the focusing

by time-reversal at high amplitudes triggers rearrangements remotely, around the focal spot.

References

[1] Heinrich M Jaeger, Sidney R Nagel, and Robert P Behringer. Granular solids, liquids, and gases. *Reviews of modern physics*, 68(4):1259, 1996.

[2] GDR MiDi gdrmidi@ polytech. univ-mrs. fr http://www. lmgc. univ-montp2. fr/MIDI/. On dense granular flows. *The European Physical Journal E*, 14:341–365, 2004.

[3] Joe D Goddard. Nonlinear elasticity and pressure-dependent wave speeds in granular media. *Proceedings of the royal society of London. Series A: mathematical and physical sciences*, 430(1878):105–131, 1990.

[4] LD Landau. Em lifshitz theory of elasticity, 104–107, 1959.

[5] K Johnson. Contact mechanics cambridge university press london. *UK*, 1985.

[6] Heinrich Hertz. Über die berührung fester elastischer körper. *Journal für die reine und angewandte Mathematik*, 92(156-171):22, 1882.

[7] Jacques Duffy and RD Mindlin. Stress-strain relations and vibrations of a granular medium. 1957.

[8] P Dantu. Contribution à l'étude mécanique et géométrique des milieux pulvérulents. *Proc. 4th ICSMFE, London, 1957*, 1957.

[9] Nicolas Brodu, Joshua A Dijksman, and Robert P Behringer. Spanning the scales of granular materials through microscopic force imaging. *Nature communications*, 6(1):1–6, 2015.

[10] T Travers, M Ammi, D Bideau, A Gervois, JC Messager, and JP Troadec. Uniaxial compression of 2d packings of cylinders. effects of weak disorder. *EPL (Europhysics Letters)*, 4(3):329, 1987.

[11] Bruno Gilles and Christophe Coste. Low-frequency behavior of beads constrained on a lattice. *Physical review letters*, 90(17):174302, 2003.

[12] Hernán A Makse, David L Johnson, and Lawrence M Schwartz. Packing of compressible granular materials. *Physical review letters*, 84(18):4160, 2000.

[13] Leonardo E Silbert, Deniz Ertaş, Gary S Grest, Thomas C Halsey, and Dov Levine. Geometry of frictionless and frictional sphere packings. *Physical Review E*, 65(3):031304, 2002.

[14] Martin van Hecke. Jamming of soft particles: geometry, mechanics, scaling and isostaticity. *Journal of Physics: Condensed Matter*, 22(3):033101, 2009.

[15] Andrea J Liu and Sidney R Nagel. Jamming is not just cool any more. *Nature*, 396(6706):21–22, 1998.

[16] ME Cates, JP Wittmer, J-P Bouchaud, and Ph Claudin. Jamming, force chains, and fragile matter. *Physical review letters*, 81(9):1841, 1998.

[17] ME Cates, JP Wittmer, J-P Bouchaud, and P Claudin. Jamming and static stress transmission in granular materials. *Chaos: An Interdisciplinary Journal of Nonlinear Science*, 9(3):511–522, 1999.

[18] Vitali F Nesterenko. Propagation of nonlinear compression pulses in granular media. *J. Appl. Mech. Tech. Phys.(Engl. Transl.);(United States)*, 24(5), 1984.

[19] Christophe Coste, Eric Falcon, and Stephan Fauve. Solitary waves in a chain of beads under hertz contact. *Physical review E*, 56(5):6104, 1997.

[20] M de Billy and X Jia. Experimental analysis of the propagation of elastic waves in a chain of spherical beads. *The Journal of the Acoustical Society of America*, 105(2):1147–1147, 1999.

[21] Guillaume Huillard, Xavier Noblin, and Jean Rajchenbach. Propagation of acoustic waves in a one-dimensional array of noncohesive cylinders. *Physical Review E*, 84(1):016602, 2011.

[22] PJ Digby. The effective elastic moduli of porous granular rocks. 1981.

[23] K Walton. The effective elastic moduli of a random packing of spheres. *Journal of the Mechanics and Physics of Solids*, 35(2):213–226, 1987.

[24] JD Goddard. Continuum modeling of granular assemblies. In *Physics of dry granular media*, pages 1–24. Springer, 1998.

[25] Xiaoping Jia, C Caroli, and B Velicky. Ultrasound propagation in externally stressed granular media. *Physical Review Letters*, 82(9):1863, 1999.

[26] Carsten Draeger and Mathias Fink. One-channel time reversal of elastic waves in a chaotic 2d-silicon cavity. *Physical Review Letters*, 79(3):407, 1997.

[27] Mathias Fink. Time-reversed acoustics. *Scientific American*, 281(5):91–97, 1999.

[28] Mathias Fink. Time reversal of ultrasonic fields. i. basic principles. *IEEE transactions on ultrasonics, ferroelectrics, and frequency control*, 39(5):555–566, 1992.

[29] Gabriel Montaldo, Phillippe Roux, Arnaud Derode, Carlos Negreira, and Mathias Fink. Generation of very high pressure pulses with 1-bit time reversal in a solid

waveguide. *The Journal of the Acoustical Society of America*, 110(6):2849–2857, 2001.

[30] Arnaud Derode, Arnaud Tourin, and Mathias Fink. One-bit time reversal through high-order multiple scattering media. *The Journal of the Acoustical Society of America*, 105(2):955–955, 1999.

[31] J Léopoldès, X Jia, A Tourin, and A Mangeney. Triggering granular avalanches with ultrasound. *Physical Review E*, 102(4):042901, 2020.

[32] Maxime Harazi, Yougu Yang, Mathias Fink, Arnaud Tourin, and Xiaoping Jia. Time reversal of ultrasound in granular media. *The European Physical Journal Special Topics*, 226(7):1487–1497, 2017.

[33] Maxime Harazi. *Diffusion multiple et retournement temporel des ondes ultrasonores dans les milieux granulaires secs et immergés*. PhD thesis, Université Sorbonne Paris Cité, 2017.

[34] Keiiti Aki and Bernard Chouet. Origin of coda waves: source, attenuation, and scattering effects. *Journal of geophysical research*, 80(23):3322–3342, 1975.

[35] Arnaud Tourin. *Diffusion multiple et renversement du temps des ondes ultrasonores*. PhD thesis, Université Paris, 1999.

[36] Arnaud Derode, Philippe Roux, and Mathias Fink. Robust acoustic time reversal with high-order multiple scattering. *Physical review letters*, 75(23):4206, 1995.

Chapter 4

Conclusions and perspectives

In this thesis we studied acoustic wave propagation through granular media, either dry or immersed in water.

In a first part, we built a 2D model of a granular medium by stacking copper rods in water. We studied this model as the limiting case of a slab-like multiple scattering medium, composed of discrete scatterers that are brought together until they touch. In the dilute case, we measured values of the scattering mean free path that are in very good agreement with the ones predicted by the Independent Scattering Approximation (ISA). Then, we investigated the transition to a dense packing by bringing together the copper rods, increasing the surface fraction by a factor of fifteen. Then, one of the main results of such transition, is the appearance of a low-frequency ballistic wave, with a frequency much lower than the central frequency of the initial pulse. We found that its behavior is well predicted by the ISA, measuring the scattering mean free path ℓ_S for this frequency. For the central frequency, we studied the second moment of the transmitted wave: the average incoherent intensity. In particular, for the largest slab thickness of the compact medium, the average transmitted intensity is fitted with the solution of the diffusion equation in 1D, with the corresponding boundary conditions. Using this model, we measure the absorption time and diffusion coefficient. Then, assuming that transport velocity is equal to propagation velocity in water, we determined the transport mean free path. We found that the medium thickness is about 6 times ℓ^*, which justifies the utilization of the diffusion approximation for the incoherent intensity.

In a second part, we focused on acoustic diffusive transport through a 3D dense granular packing. Our experimental system consisted of a random close-packed suspension of monodisperse glass beads immersed in water. We first characterized the system by measuring the transport parameters using well-known methods. Working in the transmission mode, we studied the time-of-flight distribution (i.e., the average time-dependent intensity). Depending on the ratio between the scattering mean free path and the sample size, we were able to fit the time-of-flight distribution to the solution of either the radiative transfer equation or the diffusion equation. For small beads, with diameter 1.5mm, we

used the solution of the diffusion equation in a half-space. With it, we fitted our experimental data and measured the absorption time and the diffusion coefficient. For bigger beads, with diameter 5mm, we see the coexistence between a purely ballistic and a purely diffusive regime in the transmitted intensity. Thus, we utilized the radiative transfer equation to fit our data. With this model, we were able to determine the absorption time, the scattering mean free path and to estimate both the diffusion coefficient and transport mean free path. Furthermore, with these parameters, we estimated the transport velocity of the energy. Surprisingly, the value obtained is about half of propagation velocity in water, suggesting a strong multiple scattering in our medium.

Then, we exploited the Coherent Backscattering Effect (CBE) by measuring the backscattered average intensity. The CBE allowed us to measure independently both the diffusion coefficient and the transport mean free, analyzing respectively the dynamic and stationary cone. With the independent measurement of the transport parameters, we calculate the transport velocity of the system. We found an energy velocity that is about half of the propagation velocity in water, as obtained previously by the TOF distribution. This result suggests, for the two bead sizes larger than to the shear wavelength within the beads used here, the presence of resonance scattering would be possible as observed in similar experiments in immersed bead packings, where comparable values for the transport velocity were measured experimentally[1]. Further careful investigation is still required to confirm such a scenario, for example, by studying immersed granular packing with the bead size smaller than the shear wavelength.

Based on the link that can be established between the CBE and time-reversal focusing, we presented an experimental situation where the last one can be related to the transport parameters of the system. First, a physical picture to understand how time-reversal might be sensitive to the transport parameters. Then, we presented a full model describing the situation, explicitly exposing the relation between time-reversal focusing and the diffusion coefficient. With such a model, the experimental results measured were fitted, resulting in the determination of the diffusion coefficient of the system. Furthermore, we found that, exploiting self-averaging property of time-reversal focusing, it is possible to measure the parameter in a single realization of the experiment.

In the last part, we studied time-reversal of acoustic waves through a 3D dense dry granular packing under external stress, with the aim to propose a method for creating a perturbation controlled in both time and space. The idea was to take advantage of multiple scattering to focus a high-amplitude wave at some particular location, inducing a localized rearrangement without rearranging the rest of the medium. To verify the feasibility of time-reversal rearrangement triggering, a proof-of-concept experiment was first carried out in a chaotic cavity. Taking advantage of the reverberation in the cavity, we

[1]Schriemer, H. P., Cowan, M. L., Page, J. H., Sheng, P., Liu, Z., & Weitz, D. A. (1997). Energy velocity of diffusing waves in strongly scattering media. Physical Review Letters, 79(17), 3166.

were able to focus high-amplitude ultrasound on a bead trapped on an inclined plane and to dislodge it. Then, we moved to the case of a dry granular medium under external stress. First, we established a careful preparation protocol to ensure the reproducibility of our experiments. We then carried out a first set of time-reversal experiments with low source amplitudes, so we could confirm the reversibility of wave propagation in such a fragile granular medium. Then, we studied time-reversal focusing by varying the amplitude at step two of the time-reversed wave. Using cross-correlation of acoustic signatures to monitor the region of interest, we indeed found a small window of parameters where rearrangements can be induced in the focal region, without significant rearrangement in other regions.

Perspectives

Several perspectives can be drawn for future works.

First, it would be interesting to further study the transition from dilute to compact media. In our work, we focused on the two extreme cases, with either the scatterers separated by a distance greater than their diameter or placed in contact with each other. A more systematic analysis in terms of the surface fraction would be useful to investigate the validity range of the dilute media approximation. In particular, it would be possible to describe the transition towards a compact media in terms of the appearance of a low-frequency ballistic wave, and characterize its contribution as the surface fraction increases.

Secondly, the presented link between time-reversal and the transport parameters could be exploited for another use of our interest. Following the theory presented in this manuscript, and using that the time-reversal focusing is a statistical estimator of the correlation length of the acoustic field measured in a plane far from the system, this model can be used to estimate the depth of a hidden object within a complex medium. If a source (possibly a passive source, i.e. an externally illuminated reflector) would be located in the multiple scattering medium at a depth greater than the mean free path, its location could be found by calculating the correlation length of the signals acquired in a plane away from the system. Therefore, this theory evidences the possibility of localizing an object immersed in a complex medium in a non-invasive way.

Thirdly, we have shown that TR focusing can be used to create controlled rearrangements at a particular location, but in very tiny window of parameters. Our attempt to using a N-channel Time Reversal Mirror ($N > 1$) instead of one (each one emitting an amplitude decreased by a factor N) has failed so far. However, we think that this strategy should be further investigated, which could pave the way for a controlled remote triggering of avalanches.

Finally, the conjunction of measuring the transport parameters and the generation of rearrangements in a complex medium triggers our interest. In particular, there is an experimental approach that allows not only to reach higher amplitudes, but also to perform a frequency sweep in a single measurement: the utilization of non-linear waves. A non-linear pulse can generate, throughout its propagation, harmonics that are multiples of the central operating frequency. If there is an emitter and a detector that allow the emission/reception of a large bandwidth, the time-reversal can be carried out for the emitted wave as well as for its harmonics. It has been shown that non-linear waves propagate independently of their harmonics in media such as water or the like[2]. In particular, performing a time-reversal reversal experiment including the harmonics generated during the propagation of a non-linear wave, would allow to determine the transport parameters

[2]Garay, G., Benech, N., Abraham, Y., & Negreira, C. (2020). Nonlinear wave propagation through multiple scattering media and virtual time reversal focusing. The Journal of the Acoustical Society of America, 148(3), 1315-1324.

for several frequencies in a single realization. Furthermore, the inclusion of the harmonics in a time-reversal experiment can improve the energy at the focal spot, allowing us to generate local perturbations of the density and compressibility of the medium. In this direction, the generation of controlled remotely triggered rearrangements by time-reversal focusing could be further improved by using non-linear waves.

APPENDICES

Appendix A

Time-reversal experiments in dry granular media using multi-channel time-reversal mirror

In the multi-channel configuration case, an electronic platform from Lecoeur Electronics was used, which is capable of handling simultaneously and independently up to sixteen channels in emission and another sixteen channels in reception. This equipment allows to emit signals up to $100V_{pp}$ on each channel and to record signals with a sampling frequency up to 80MHz. The signal generated under Matlab then must consist of a 7 entry matrix of which one contains the signal to be transmitted, the other ones being filled with zeros. The waveforms transmitted through the granular medium are captured by the sixteen receivers, digitized, stored in the memories of the Lecoeur platform and transferred to Matlab for further analysis (figure A.1).

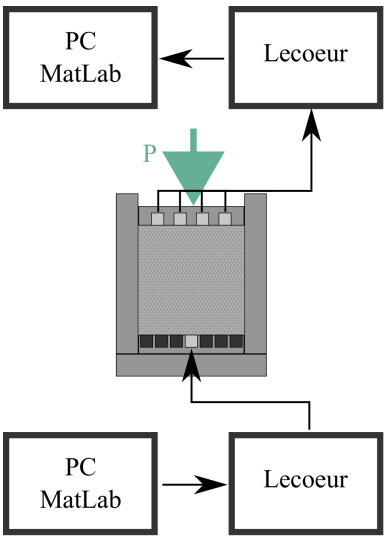
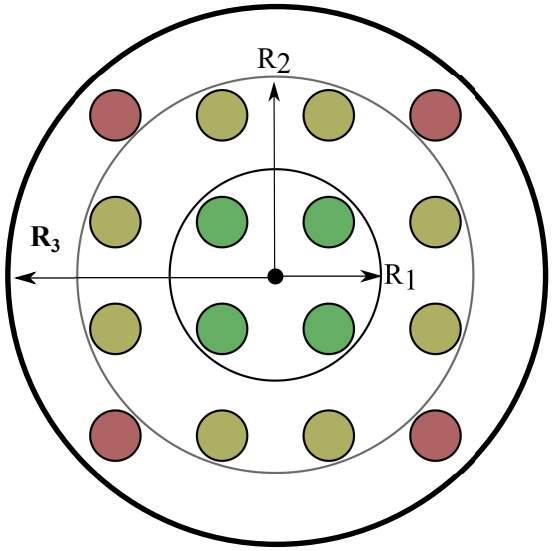


Figure A.1: Experimental configuration for the emission/reception experiment for multi-channel experiments.

A.0.1 Multi-channel time-reversal mirror

As shown in the previous paragraph, TR focusing is possible with a TRM limited to one single element. Here we will use the whole TRM we have built, which consists of sixteen transducers. The focal spot width does not depend on the TRM aperture but the signal-to-sidelobes level does[1]. In a first intuition, another possible advantage of using several channels instead of one, is to distribute spatially the energy injected in the granular medium. In other words, the same amplitude at the focal point should be obtained in a one-single channel experiment where the time-reversed wave is sent with an amplitude A and in an N-channel TR experiment where each of the N time-reversed signal is sent with an amplitude A/N. Thus using the 16-channel TRM should help to reach our goal, that is rearranging the medium around the source without rearranging it on the TRM side. As we will see in the last part of this chapter, the situation is not so simple. But let us first characterize the performances of TR against the number of channels.



(a)

Figure A.2: Distribution of transducers on the top of the container. Three different groups are distinguished for the reception/reemission of acoustic waves during the time-reversal experiment. In green, the central group of transducers $D_1 - D_4$ located within a radial distance R_1; in yellow, the group $D_5 - D_{12}$ located at a distance $R_1 < X \leq R_2$; in red, the group closest to the edge $D_{13} - D_{16}$ located at a distance $R_2 < X \leq R_3$.

We follow the same procedure as before: measure reference signals, perform the TR experiment, measure the new signatures of the medium and finally determine the correlation coefficients that quantify potential modifications of the medium. As in the previous experiments, the initial excitation was generated by the central transducer at the bottom of the container S_1. Based on the symmetry of the TRM, we can divide its channels into

[1]Derode, A., Tourin, A., & Fink, M. (2001). Random multiple scattering of ultrasound. II. Is time reversal a self-averaging process?. Physical Review E, 64(3), 036606.

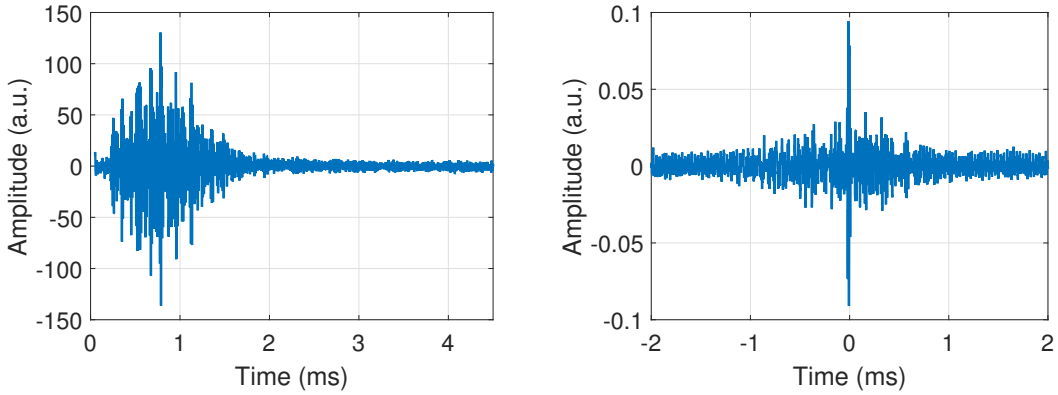


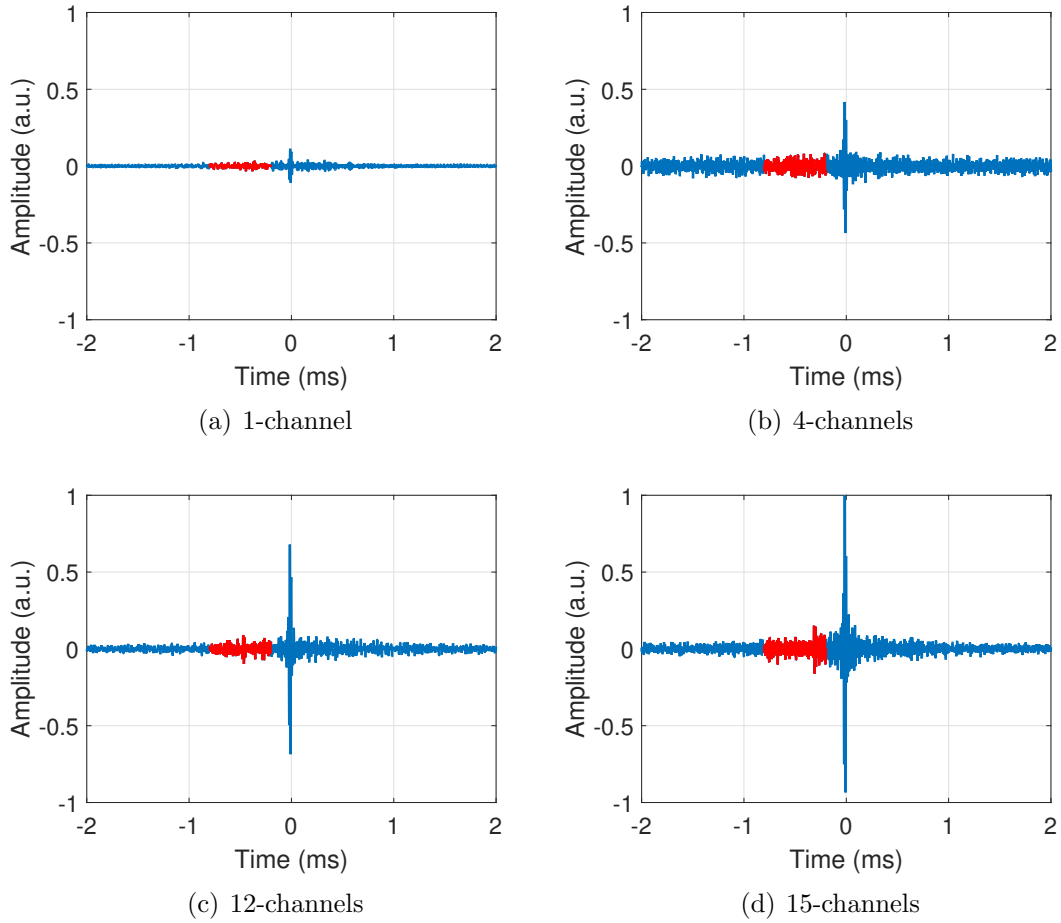
Figure A.3: Time-reversal measurements in the linear regime for a configuration using a single channel in the TRM. The experiment is performed using the Lecoeur Electronics equipment, in order to have a comparative measurement with the case in which the equipment consisting of the function generator and the oscilloscope is used. Both initial excitation and re-emission were performed at an amplitude of $10V_{pp}$. The transmitted signal is high-pass filtered with a cutoff frequency of 45kHz. (a) Transmitted coda after filtering. (b) Time recompression measured at S_1.

three different groups as shown in figure A.2: the central ones, from D_1 to D_4, those located at a medium distance, from D_5 to D_{12}, and those closer to the cell edge, from D_{13} to D_{16}. The element D_{16} is not used since it is the channel with the highest coupling with the initial emission, so it is not reliable when measuring the wave transmission or performing the time-reversal.

As a first test, the time-reversal was performed with a single channel driven thanks to the multi-channel electronics. The source was excited with the minimum amplitude provided by this latter, that is $10V_{pp}$. In figure A.3 is shown a filtered coda signal together with the resulting time recompression. In this situation, we find a correlation coefficient $C_{Source} = 0.95$ in the source region and $C_{TRM} = 0.96$ in the TRM region, which is consistent with our previous measurements and verifies the linearity assumption.

Then, TR experiments were carried out by increasing the number of channels: 4, 12 and 15. Each time-reversed signal is normalized by the absolute maximum amplitude measured on the array such that the maximum reemitted amplitude corresponds to $10V_{pp}$ and the amplitude variations from one channel to the other are preserved. Figure A.4 shows the evolution of the time recompression in terms of the number of elements used in the TRM. The evolution is not linear contrary to what could have been expected, which can be related to the fact that the amplitude of the scattered field captured by the TRM decreases with the radial distance to the symmetry axis. This can be interpreted as a manifestation of the anisotropy of the contact force network resulting in a non homogeneous spatial distribution of the scattered field.

As a measure of the quality of time recompression we use the peak-to-lobe ratio. This



(a) 1-channel (b) 4-channels

(c) 12-channels (d) 15-channels

Figure A.4: Time recompressions obtained by changing the number of elements used for time-reversal focusing. The time recompression amplitudes are normalized by the maximum amplitude obtained with the 15-channel TRM. In red is highlighted part of the signal considered for the calculation of the peak-to-lobe ratio.

quantity is the ratio of the peak amplitude to the standard deviation of the surrounding lobes (see figure A.4). At the focal time, the time-reversed signals backpropagated from each transducer are in synchrony, resulting in a coherent summation. Outside the focal time, the sidelobes add up incoherently. One can thus expect the peak-to-lobe ratio to vary as $\sqrt{N}$. This is the tendency observed in figure A.5 up to $N = 12$. Increasing further the number of channels is not useful meaning that the channels on the TRM edge do not contribute to improving the recompression. This could be a signature of temporal and/or spatial long range correlations[2].

Finally, the correlation coefficient around the source and the TRM, as well as their nearest neighbours, are computed. As in the one single-channel case, the results shown in table A.1 show the stability of the granular medium during the time-reversal experiment.

[2]Derode, A., Tourin, A., & Fink, M. (2001). Random multiple scattering of ultrasound. II. Is time reversal a self-averaging process?. Physical Review E, 64(3), 036606.

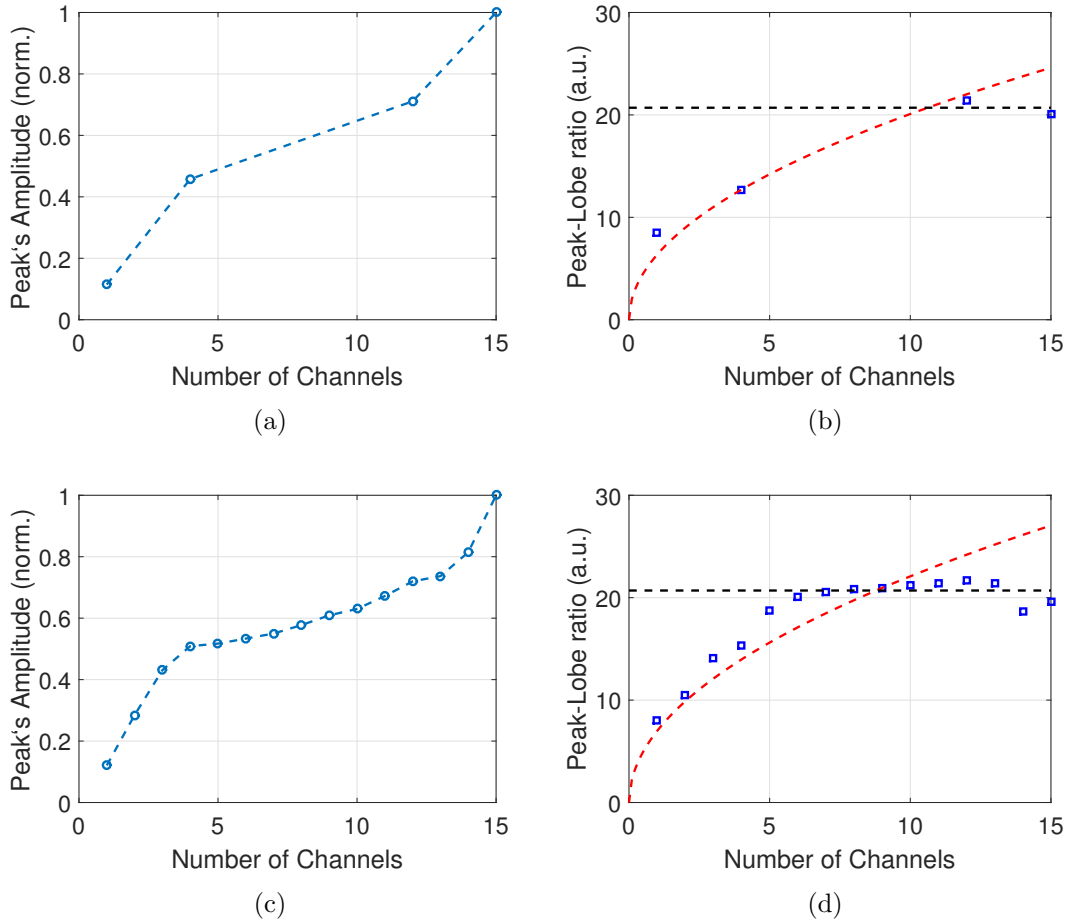


Figure A.5: Evolution of the peak and peak-to-lobe ratio of time recompression as a function of the number of transducers in the TRM. (a) Peak of the time recompression as a function of the number of channels used in the TRM. The evolution of the peak shows a sub-linear behavior. (b) Peak-to-lobe ratio as a function of the number of channels in the TRM, showing a dependence as $\sqrt{N}$ up to 12 channels (red curve). (c) Peak of the time recompression calculated as the cross-correlation in terms of the number of acquired coda waves. The cross-correlation peak in terms of the number channels behaves similarly to the experimental results obtained. (d) Peak-to-lobe ratio of the cross-correlation as a function of the number of coda waves. The $\sqrt{N}$ dependence is presented (red curve) as the saturation value (black curve) of the peak-sidelobe ratio. As in (c), the cross-correlation behaves similarly to the experimental results obtained.

C.C.	4-channels	12-channels	15-channels
C_{Source}	0.96	0.93	0.94
C^N_{Source}	0.97	0.95	0.95
C_{TRM}	0.98	0.94	0.95
C^N_{TRM}	0.97	0.96	0.93

Table A.1: Correlation coefficients between acoustic signatures before and after the linear time-reversal experiment.

A.0.2 Multi-channel high-amplitude time reversal

In section 3.4 we found a small window of parameters for which TR focusing allows the granular medium to be rearranged only around the source. The results were however maybe not as spectacular and convincing as could have been expected. The situation is as follows: as shown in section 3.3.3, if the re-emitted amplitude is not high enough, no rearrangement is observable. Our idea was to exploit the time compression and space focusing properties of TR for re-emitting the time-reversed Coda wave with an amplitude low enough to avoid rearrangements of the granular medium on the TRM side while focusing an amplitude high enough at the source. But it turns out that as soon as the amplitude of the TR wave is increased, the medium starts to be rearranged on the TRM side and during back propagation such that TR invariance breaks. Even in the range of amplitudes where the TR peak increases, the signal-to-noise ratio simultaneously decreases, which illustrates a loss of reversibility.

As a last attempt, we use a multi-channel TRM with the aim to obtain the same amplitude at the source by reemitting an amplitude N times lower on each channel, with N the number of channels.

We limit the TRM to $N = 12$ channels D_1 to D_{12} since, as shown in A.0.1, the other channels do not allow the signal-to-sidelobes to be further improved. We covered amplitude ranging from $A_2 = 10\mathrm{V_{pp}}$ to $A_2 = 100\mathrm{V_{pp}}$. As in the single-channel case, the correlation coefficients in the source and TRM regions were studied, as well as the evolution of both the peak and the peak-to-lobe ratio of the time recompression. The results are shown in figure A.6.

Figure A.6a shows the correlation coefficients C_{Source} and C_{TRM} as a function of the TR re-emitted amplitude. Unlike the single-channel case (see figure 3.30a), we observe that C_{TRM} decreases before C_{Source}. In a first intuition, we would have expected to limit the rearrangement on the TRM side by using a larger number of channels, each emitting a smaller amplitude. But what actually happens is that, when excited over a larger surface with 12 transducers instead of one, the granular medium becomes more fragile as compared to the single-channel case.

Figures A.6b and A.6c show the evolution of respectively the peak and peak-to-lobe ratio of the time recompression signal. From these results it can be said that, up to a value $A_2 = 40\mathrm{V_{pp}}$ the system behaves as linear, presenting a linear growth of the peak and an approximately constant peak-to-lobe ratio. But the maximum reached amplitude is not enough to create rearrangements as shown in A.6a. For larger amplitudes, the peak no longer behaves linearly, but remains constant. The peak-to-lobe ratio begins to decrease as soon the amplitude A_2 increases, a signature that rearrangements occur that contribute to a worsening of the time-reversal recompression.

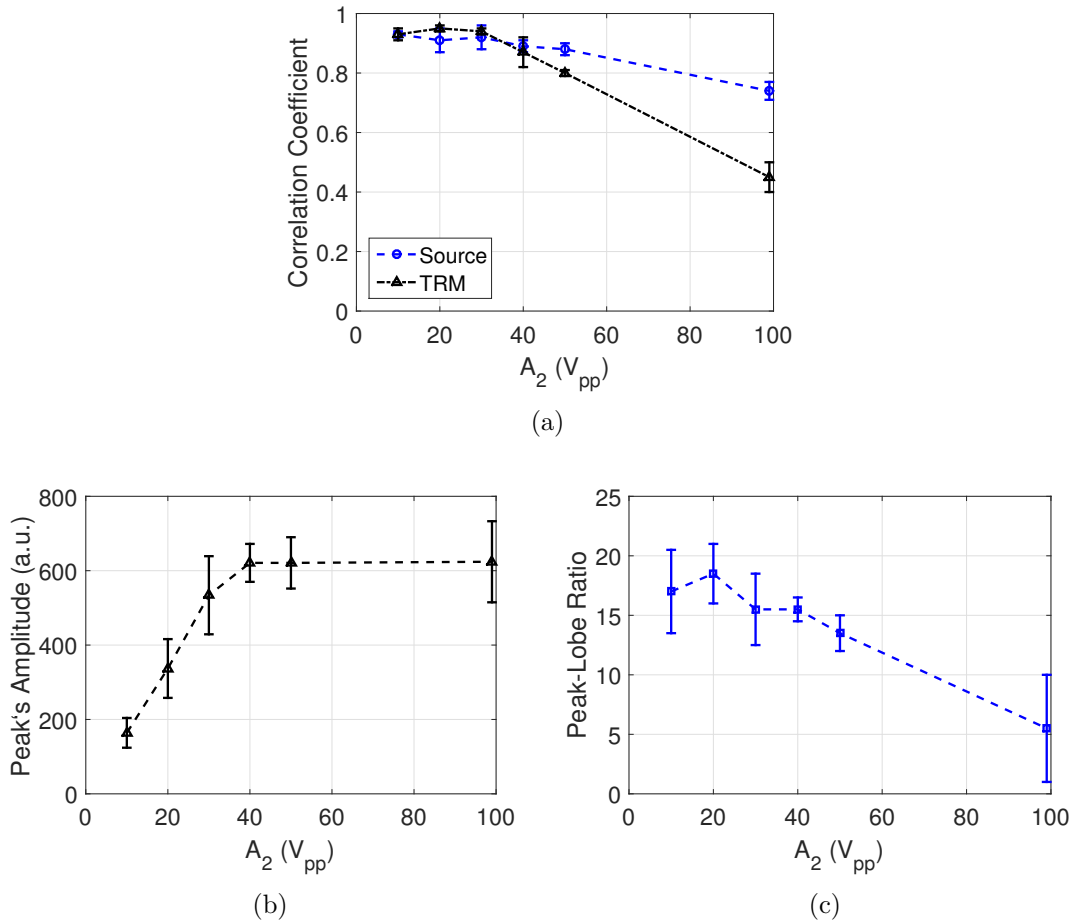


Figure A.6: Multi-channel TR experiment with an increasing amplitude A_2 in step 2. (a) Correlation coefficient between acoustic signatures measured in the source and TRM regions. (b) Evolution of the time recompression's peak as a function of amplitude A_2. For amplitudes up to 40V_{pp} the recompression peak grows linearly. For larger amplitudes, the peak remains approximately constant. (c) Dependence of the peak-to-lobe ratio of the time recompression with the amplitude A_2. For values up to 40V_{pp} this quantity remains approximately constant. After this value, it starts to decrease.